Bismuth telluride nanoparticles for thermoelectrical application, synthesis and incorporation into polymer hybrid composites

Aigerim Baimyrza

Normandie Université

THÈSE

Pour obtenir le diplôme de doctorat

Spécialité CHIMIE

Préparée au sein de l'Université de Caen Normandie

Bismuth telluride nanoparticles for thermoelectrical application, synthesis and incorporation into polymer hybrid composites

Présentée et soutenue par
AIGERIM BAIMYRZA

Thèse soutenue le 27/10/2022 devant le jury composé de		
M. YVES GROHENS	Professeur des universités, UNIVERSITE BRETAGNE SUD UBS	Rapporteur du jury
MME LORETTE SICARD	Maître de conférences HDR, Université Paris Cité	Rapporteur du jury
M. CYPRIEN LEMOUCHI	Maître de conférences, Université de Caen Normandie	Membre du jury
MME VALÉRIE GAUCHER	Professeur des universités, Université de Lille	Président du jury
M. LOIC LE PLUART	Professeur des universités, Université de Caen Normandie	Directeur de thèse

Thèse dirigée par LOIC LE PLUART (Laboratoire de chimie moléculaire et thio-organique (Caen))

UNIVERSITÉ CAEN NORMANDIE

ED 508 NC Normande de Chimie

lcmt

Acknowledgement

These three years of thesis research were also three years of experiencing a life in France, thus I would like to show my appreciation to all the people listed here, and of course those I forgot to mention, not only for their help in my thesis study but also for their assistance in adjusting to the French lifestyle, which I started to understand and enjoy.

Firstly, I would like to express my gratitude to the director of my thesis, Pr. Loïc Le Pluart for the great opportunity to be the part of his team and work under his guidance throughout the project. Thank you for your believe and tremendous support of my ideas and projects. Your professionalism, the way of handling challenges and kindness inspired me a lot and gave courage to continue with my path.

Secondly, I would like to thank the members of the Jury Pr. Yves Grohens, Dr. Lorette Sicard and Pr. Valérie Gaucher for accepting my thesis work for evaluation and devoting your precious time for that.

Special mention and gratitude to Jean-Francois Lohier, Director of the Doctoral school EDNC Dr. Isabelle Dez and my referent teacher Dr. Stéphane Perrio for standing by me when I decided to change the research team and topic. This decision completely altered my scientific path, my experience, and life in a positive direction and gave me the opportunity for a whole new start. Without your support, I would not be able to do the proper changes timely.

Certainly, I am thankful to co-supervisor of my thesis Dr. Cyprien Lemouchi his guidance in the synthesis and post-doctoral researcher Dr. Biduir Rajal for providing training in this area.

Also, I would like to note how grateful I am for the people in LCMT. Director of LCMT Pr Thierry Lequeux for welcoming me in his laboratory. Mdme Marie-Cecile Helaine and Mdme Jeanine Amice for the administrative support and their special kindness. Cyril Lebargy, Remi Legay, Guillaume Morcel for their help in the respective areas. Adrien Lanel for the countless supply of round bottom flasks and custom designed tricky shaped glassware. PhD students of LCMT, Fatima Almetwali, Dr. Thibault Thierry, Dr. Abdoul-Gadiry Diallo, Malak Qassab, Iliya Lenko, Charles Jambous, Jean-Nicolas Noel, Yougourten Boumekla, Aimar Gonzalo, Dr. Leo Bettoni and others for sharing the fate of a PhD student and being there with me.

Specials thanks to Dr. Mohammad Wehbi and Dr. Romuald Herbinet with whom I shared the office, for the warm and friendly working environment and your tremendous help and support on both, scientific and personal matters. I am also thankful to your families, which made me feel as a part of one in France as well.

I would like to show my gratitude to CRISMAT collective for their assistance. Firstly, Dr. Richard Retoux for teaching me how to operate SEM and for his endless patience, kindness and time spent searching for tubes for my samples. I cannot express how touched I am by your thoughtfulness, since even in rough times you made sure that your absence is covered. Thank you, Pr. Franc Gascoin for providing access to the CRISMAT facilities and your scientific input in the project. Special thanks to Pr. Daniel Chateigner for helping me to refine and verify XRD spectra. In addition, I want to thank Xavier Larose, Jérôme Lecourt, Stephanie Gascoin, Christophe Couder, Christelle Bilot for all the trainings, help in dealing with my special and tricky samples and kindness. Thanks to the PhD students of CRISMAT, Dr. Hugo Bouteiller, Krishnendu Maji, Yiteng Xing, Antoine Levee. Alix Souchon for his brightening smile through the days in CNRT.

I am very thankful to the people in the Insitute of Polymers and Composite in Hamburg Technical University Pr. Bodo Fiedler, Valea Kim Wisniewski and Dr. Hristiana Velichkova for the opportunity to work there, for their help in adopting their method to my system, for warm welcome and unforgettable experience.

Many thanks to my friend and dearest person in France Clement Gonnot for his support and, even if not physically, but for always being around and reachable. Also, I would like to mention how greatly I appreciate you, my beloved friends Nathalie, Aidana and Fariza. My dear friends from LCS Vera Bikbaeva, Lois Aguilera and Aymeric Magisson.

Last, but not least, I would like to thank my family. My parents for everything, my sisters for always being there for me, and my niece and nephew for giving special meaning to my life.

Résumé en Français

Introduction

Le bouleversement climatique principalement causé par l'effet de serre dû à la consommation de combustibles fossiles ainsi que le potentiel épuisement de ces derniers mettent l'humanité au défi de passer à des ressources énergétiques alternatives. À cet égard, les dispositifs thermoélectriques qui utilisent la chaleur résiduelle comme source d'énergie peuvent constituer une alternative durable pour la production d'énergie dans certaines applications. Ces dispositifs utilisent des matériaux thermoélectriques, susceptibles de générer de l'électricité à partir d'un gradient de température ou de fonctionner comme un refroidisseur Peltier en générant un gradient de température lorsqu'une tension leur est appliquée. De plus, la structure des modules thermoélectriques, sans pièces mobiles, leur confère une longue durée de vie sans entretien majeur. Malgré ces avantages des, les rendements de production d'énergie des matériaux thermoélectriques sont assez faibles et les plus performants sont composés de métaux et de terres rares. C'est pourquoi, à l'heure actuelle, ils sont principalement appliqués dans les domaines où le rapport coût-efficacité n'est pas une préoccupation (99%), comme les missions militaires et spatiales. Pour stimuler son application de masse, de nombreuses recherches sont menées pour concevoir des matériaux thermoélectriques avec une meilleure efficacité ou pouvant être produits par des procédés adaptable à grande échelle, moins énergivores et économiquement viables.

Les thermoélectriques à basse température ont un potentiel particulier en raison de l'absence d'autres systèmes de collecte d'énergie à faible gradient de température et de l'abondance de la chaleur résiduelle à basse température, comme la chaleur corporelle ou celle des moteurs de voiture. Depuis sa découverte, le tellurure de bismuth Bi_2Te_3 et ses dérivés restent les matériaux thermoélectriques les plus performants dans cette gamme de température. Au cours des deux dernières décennies, ses propriétés thermoélectriques ont été considérablement améliorées grâce à diverses méthodes. L'une de ces méthodes est la nanostructuration, en particulier depuis que Hicks a postulé la morphologie nanostructurée du Bi_2Te_3 devrait diminuer la conductivité thermique du matériau, tandis que la faible dimension des nanoparticules devrait induire un effet de confinement quantique qui améliore les propriétés de transport électrique du matériau. En combinaison, ces deux effets conduisent à l'amélioration des performances thermoélectriques du matériau. Cependant, l'incorporation de ces nanostructures dans un matériau continu est un autre processus difficile et très consommateur d'énergie. Le frittage de nanoparticules dans une masse continue peut entraîner une structure

poreuse qui diminue le potentiel thermoélectrique des nanostructures. De plus, les techniques de frittage les plus efficaces, comme le pressage à chaud et le frittage par plasma, nécessitent une énergie élevée et sont donc coûteuses.

Une façon de surmonter ces inconvénients est d'introduire des propriétés thermoélectriques dans des matériaux dont la mise en œuvre nécessite moins d'énergie. Grâce à ce projet de recherche, nous voulons explorer les possibilités de fabriquer des matériaux composites basés sur une matrice thermodurcissable dans laquelle un réseau conducteur thermoélectrique composé de charges thermoélectriques percolées peut être incorporé. Afin d'abaisser le seuil de percolation et d'augmenter la conductivité du réseau, il est préférable d'utiliser des particules fortement anisotropes. C'est pourquoi le premier objectif de cette thèse de recherche a été de développer des méthodes faciles et facilement développables à grande échelle pour préparer des nanoparticules de Bi_2Te_3 avec une morphologie nanotubulaire. Ensuite, ce projet vise à explorer les méthodes de préparation de composites hybrides polymères avec un réseau percolant de charges Bi_2Te_3.

Cette thèse est présentée en trois chapitres. Le premier chapitre est une revue de la littérature dont le but est de présenter le contexte du sujet de la thèse en général. Le chapitre 2 décrit les méthodes développées pour la synthèse des nanoparticules de Bi_2Te_3 et discute de l'effet des conditions de synthèse sur la morphologie des particules et les performances thermoélectriques des matériaux. Le chapitre 3 décrit les tentatives de préparation de composites polymères hybrides par différentes méthodes utilisant le Bi_2Te_3 synthétisé comme charge, suivies de la caractérisation thermoélectrique des composites hybrides.

Résultats expérimentaux et discussion

Conformément aux objectifs de la thèse, le chapitre 2 décrit les différentes méthodologies développées pour la synthèse à reflux assistée par le 1-DDT des nanoparticules de Bi2Te3 qui ont permis d'augmenter la teneur en nanotubes dans le produit de 30% à 100% . Toutes les méthodologies suivent deux mécanismes distincts : l'enroulement et la diffusion à l'échelle nanométrique de Kirkendall. Si les deux mécanismes sont bien décrits dans la littérature, les méthodes actuelles offrent d'autres conditions de réaction douces et faciles à mettre à l'échelle. L'effet Kirkendall à l'échelle nanométrique nécessite un support sacrificiel, c'est pourquoi le développement de la méthode de préparation in-situ du support est également rapporté. Les nanoparticules synthétisées ont été caractérisées par MEB, MET et DRX.

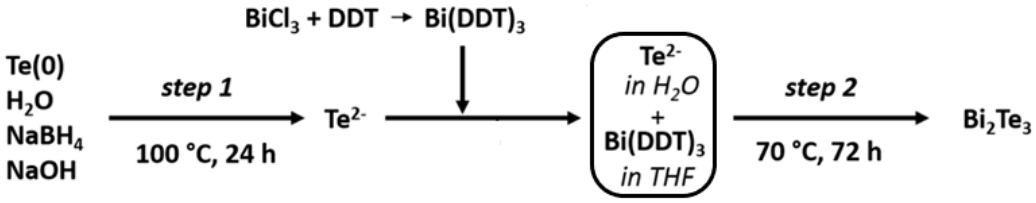

Schéma -1. Processus schématique en deux étapes pour la préparation du Bi_2Te_3 via un mécanisme d'enroulement

La première méthodologie, la synthèse à reflux assistée par le 1-DDT de nanoparticules de Bi_2Te_3 via un mécanisme d'enroulement, est développée sur la base des résultats préliminaires du groupe de recherche. La préparation des nanoparticules de Bi_2Te_3 selon le schéma-1 a été réalisée dans une cuve de réacteur agitée à double enveloppe de 2 L avec un contrôle précis de la température qui permet d'obtenir 7,00 g de Bi_2Te_3 pur pour chaque réaction. La réaction produit des nanoparticules de Bi_2Te_3 à phase pure qui, d'un point de vue morphologique, sont constituées de 30 % de nanotubes et de 70 % de particules isotropes, comme le montrent les images MEB de la figure-1.

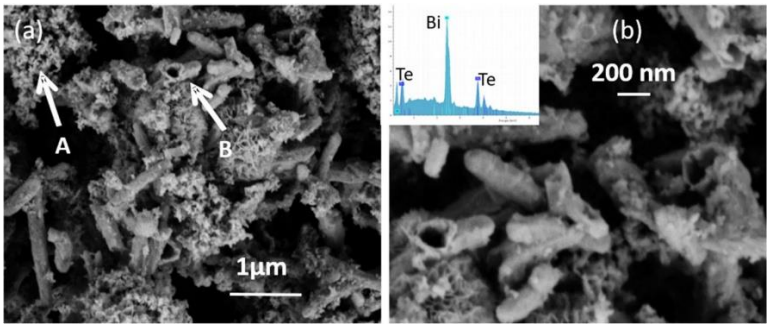

Figure - 1. Images MEB typiques d'un échantillon de Bi2Te3, en médaillon spectres EDX de la poudre.

Lors de nos premières tentatives pour augmenter la teneur en nanotubes des nanoparticules de tellurure de bismuth synthétisées selon la méthode décrite dans le schéma-1, nous avons remarqué que le Bi-DDT pouvait également réagir avec les nanoparticules de Te0, par un processus de diffusion connu sous le nom d'effet Kirkendall à l'échelle nanométrique. Au cours de ces synthèses, la morphologie du composé final est régie par la morphologie de Te0. Pour obtenir des particules tubulaires de Bi_2Te_3, il est important d'avoir comme support sacrificiel des particules de Te0 en forme de bâtonnets allongés. Les méthodes permettant d'obtenir de meilleurs supports de Te sont donc discutées. Les réactions dont les protocoles suivent n'ont pas été effectuées dans un réacteur de 2 L comme précédemment rapporté, mais dans des flacons à fond rond conventionnels plus petits afin de faciliter le travail de traitement post réactionnel.

Les bâtonnets de Te sont obtenus par précipitation des ions Te^{2-}, qui ont été obtenus comme dans la première étape de la synthèse de Bi_2Te_3 précédemment décrite. La réduction en milieu basique s'accompagne visuellement d'une effervescence et d'un changement d'aspect du mélange réactionnel qui passe d'une suspension à une solution pourpre foncé, puis à une solution claire pourpre pâle. L'effervescence suggère qu'une hydrolyse partielle du $NaBH_4$ a également lieu et conduit à la formation d'hydrogène. Après réduction complète du Te, il est re-précipité en permettant à l'oxygène de l'air d'accéder au mélange réactionnel. Après la précipitation complète de Te, qui s'observe visuellement par la formation d'une suspension gris-noir dans une solution transparente claire, celle-ci est filtrée et lavée à plusieurs reprises par de l'eau, de l'EtOH et de l'acétone, puis séchée. Cette procédure standard a été réalisée plusieurs fois, en modifiant à chaque fois un seul paramètre, afin d'évaluer l'effet des conditions modifiées sur la qualité des bâtonnets de Te. Les paramètres modifiés sont l'intensité de l'agitation, le temps d'accès à l'oxygène, le mode d'application de l'oxygène et l'ajout de surfactant. Des nanoparticules de Te avec 50% de nanobarres ont été obtenues sous agitation, tandis que 80% de nanobarres de Te ont été obtenus lorsque l'oxygène est introduit par injection directe dans la solution. Des bâtonnets à 100% de Te avec un rapport d'aspect élevé ont été obtenus lorsque le surfactant supplémentaire SDBS a été appliqué avant l'oxygène.

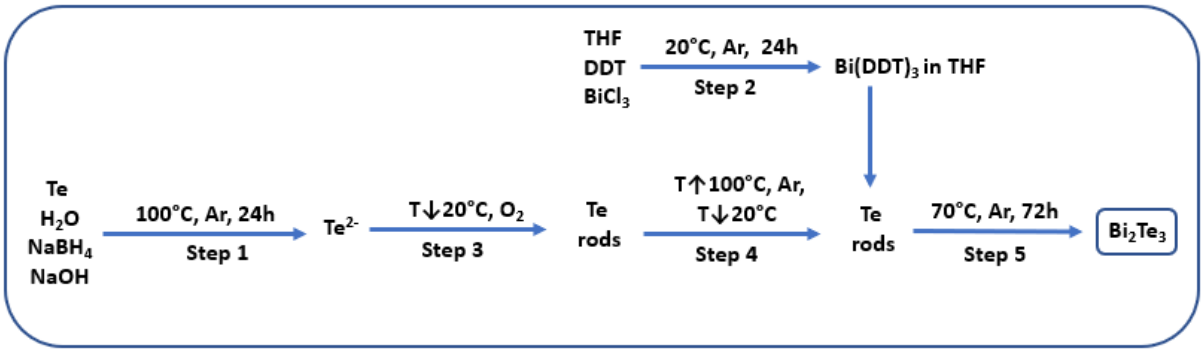

Schéma-2. Procédure générale de synthèse de Bi_2Te_3 via un mécanisme de diffusion sur des gabarits synthétisés in-situ

En appliquant différentes conditions de précipitation de Te, des nanoparticules de Bi_2Te_3 ont ensuite été synthétisées via une procédure de modélisation in situ décrite dans le schéma-2. Ce processus permet également d'obtenir du Bi_2Te_3 rhomboédrique à phase pure avec le groupe spatial R-3m (figure-2) par diffusion Kirkendall à l'échelle nanométrique. Comme il s'agit d'une formation de nanotubes assistée par unsupport sacrificiel, la teneur en nanotubes dans les particules dépend de la quantité de nanorods de Te dans le modèle. Ainsi, en fonction des conditions de recristallisation du Te, des échantillons de Bi_2Te_3 avec 50%, 80% et 100% (Figure-3) de nanotubes ont été obtenus. De plus, ce procédé a également été validé pour une synthèse en deux étape distinctes avec isolation préalable du support sacrificiel de Tellure.

Le Bi_2Te_3 obtenu a ensuite été fritté par Spark Plasma Frittage et les propriétés thermoélectriques des échantillons préparés ont été mesurées et représentées sur la figure-4.

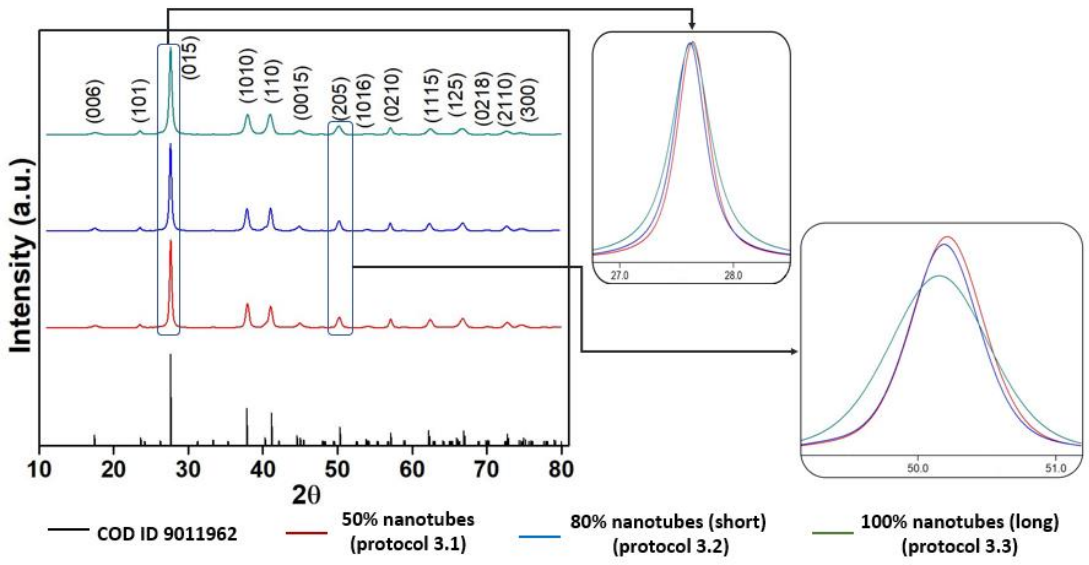

Figure-2. Spectres XRD des nanoparticules de Bi_2Te_3 synthétisées en comparaison avec le standard de COD (COD ID 9011962)

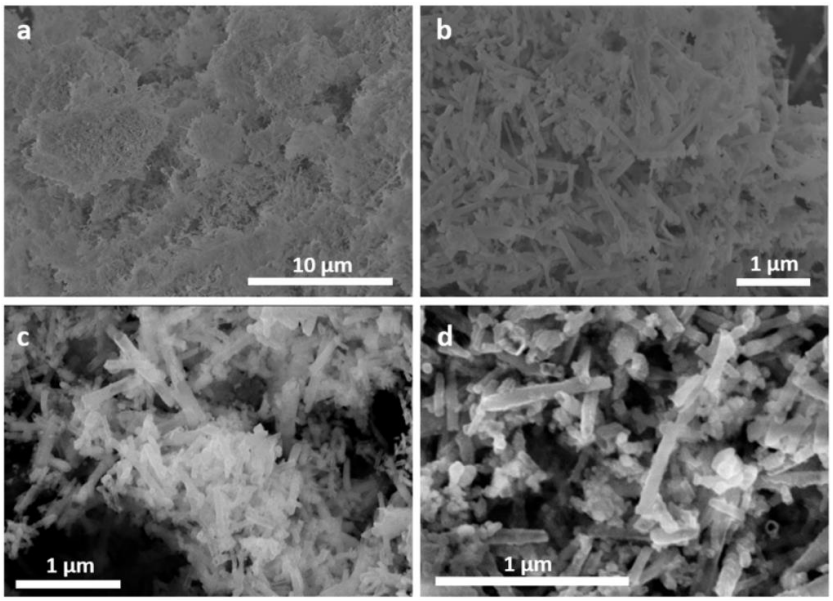

Figure-3. Images SEM des nanoparticules de Bi2Te3 synthétisées avec SDBS (100% nanotubes)

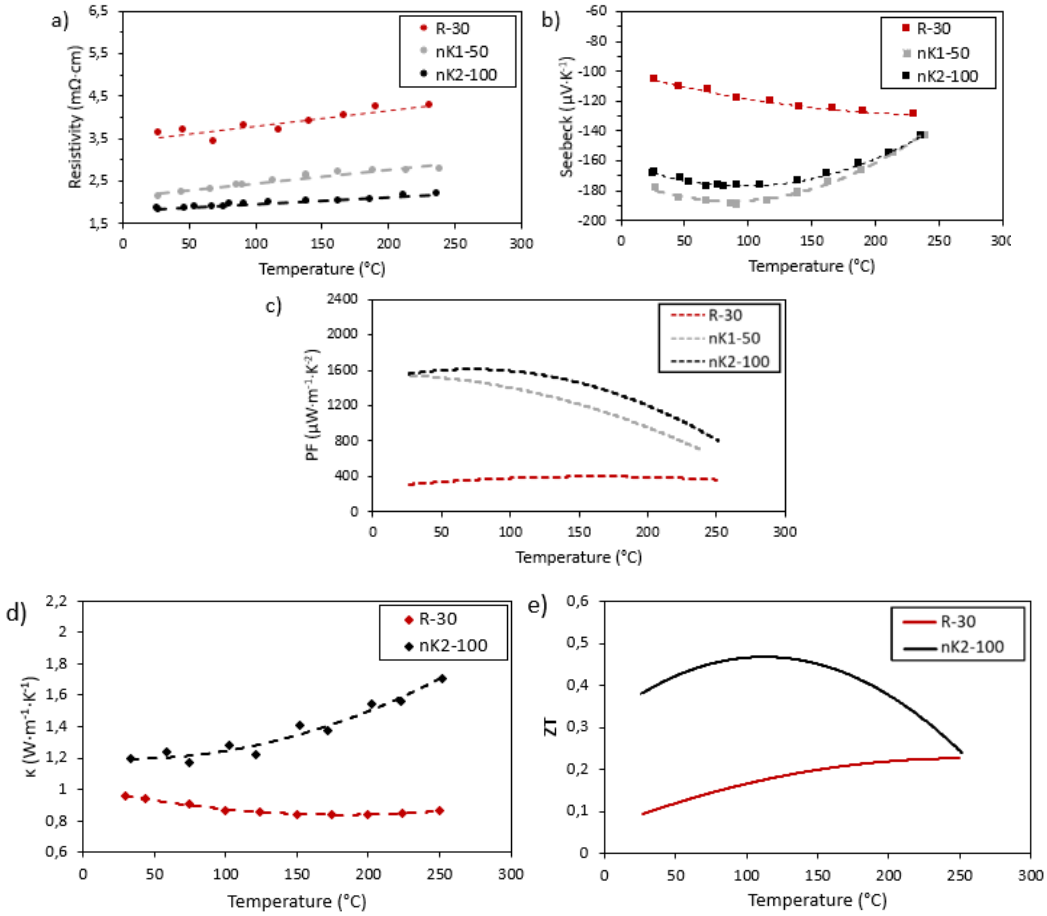

Figure-4. Variation des propriétés TE en fonction de la température des échantillons de Bi_2Te_3: a) résistivité électrique; b) coefficient Seebeck; c) facteur de puissance; d) conductivité thermique ; e) ZT

Les nanoparticules de Bi_2Te_3 synthétisées ont ensuite été utilisées comme charge pour préparer un composite polymère hybride avec une matrice de résine époxy en utilisant trois méthodes : mélange manuel, mélange rapide et infusion. Parmi ces méthodes, la méthode d'infusion a montré son potentiel pour préparer un composite thermoélectriquement actif avec un réseau de charge ségrégué. Le processus en trois étapes de la méthode d'infusion permet d'aligner les nanotubes dans une direction plane. Le composite préparé avec ces méthodes présente les propriétés thermoélectriques suivantes (Figure-5): σ = 51 mΩ·cm ; α_{max} = -108 µV/K ; PF_{max} = 22 µW/m·K2 ; κ= 0,4 W/m·K et ZT_{max} apparent est de 0,025. Les tentatives d'augmenter la conductivité électrique et de faciliter le processus d'infusion par l'inclusion de NTC dans la matrice avec Bi_2Te_3 ont conduit à la détérioration de la morphologie du composite (structure poreuse) et des propriétés thermoélectriques du matériau.

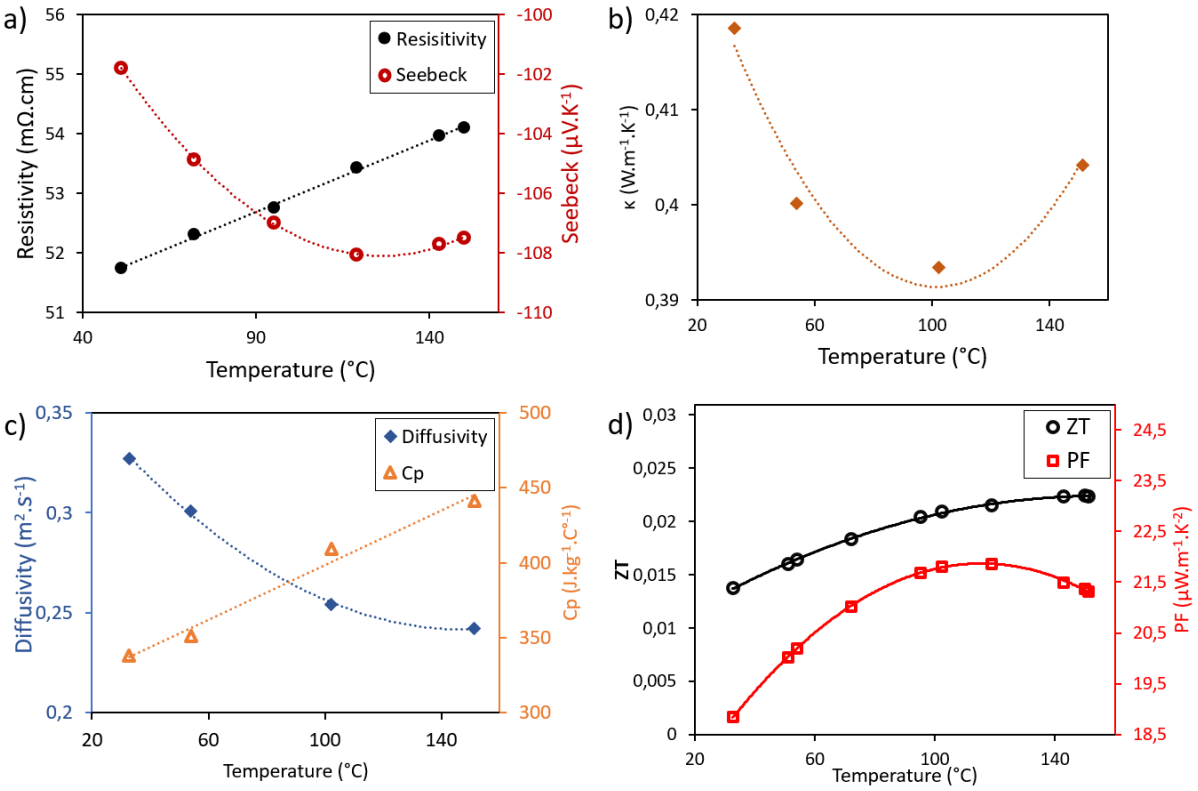

Figure-5. Dépendance des propriétés TE du composite Bi_2Te_3/résine époxy (préparé par infusion) en fonction de la température mesurée en mode chauffage : a) résistivité et coefficients Seebeck ; b) conductivité thermique (calculée) ; c) diffusivité thermique et chaleur spécifique ; d) ZT et PF (calculés).

Conclusion

L'objectif principal de la présente thèse était de développer des méthodes pour synthétiser des nanoparticules de Bi_2Te_3 avec une morphologie tubulaire pour une application thermoélectrique. En conséquence, la méthode de synthèse à reflux assistée par le 1-DDT, qui permet d'obtenir des nanoparticules de Bi_2Te_3 avec différentes teneurs en nanotubes en modifiant légèrement les conditions de réaction, a été établie. Lorsque l'on laisse les précurseurs réagir à l'état ionique, les nanotubes se forment par un mécanisme d'enroulement, qui implique la formation de feuilles et leur enroulement ultérieur en tubes. Dans de telles conditions, la réaction donne du Bi_2Te_3 rhomboédrique monophasé avec une teneur en nanotubes de 30 %. Lorsque la réaction est effectuée selon un mécanisme de diffusion de Kirkendall à l'échelle nanométrique, des nanoparticules deBi_2Te_3 avec une teneur en nanotubes allant de 50 % à 100 sont obtenus. Ainsi, l'oxydation du Te à partir de son état réduit en solution conduit à sa recristallisation dans une morphologie différente et régit la morphologie des particules finales de Bi_2Te_3, car le Te précipité joue le rôle d'un support sacrificiel. Par conséquent, l'effet des conditions de recristallisation sur la morphologie du Te précipité a été étudié de manière approfondie. L'étude montre que la morphologie du Te est fortement affectée par le tensioactif et le mode d'introduction de l'oxydant. Les barres de Te de meilleure qualité sont obtenues à des taux élevés d'apport d'oxydant et en présence de surfactant.

L'originalité de la méthode de synthèse à reflux assistée par le 1-DDT développée est la douceur des conditions de réaction. Toutes les nanoparticules de Bi_2Te_3 sont obtenues à 70°C sous reflux et l'eau est utilisée comme solvant principal. La réaction est facilement adaptable à plus grande échelle. Malgré la différence dans les mécanismes, cette méthode produit toujours une phase Bi_2Te_3 pure avec un arrangement rhomboédrique des atomes dans le réseau cristallin selon les spectres XRD. La caractérisation thermoélectrique des échantillons sélectionnés démontre des coefficients Seebeck de type n compétitifs autour de 180 μV/K après frittage. Bien qu'une certaine amélioration de la réduction de la conductivité thermique ait été obtenue, d'autres améliorations sont nécessaires pour concurrencer les matériaux de pointe. L'aspect principal qui limite la performance thermoélectrique des échantillons testés est la faible conductivité électrique. Pourtant, compte tenu de l'absence de dopage extrinsèque et des conditions de réaction relativement douces, le ZT de 0,49 est une valeur compétitive. L'optimisation des conditions de frittage et l'utilisation de nanotubes de meilleure qualité devraient permettre d'augmenter cette valeur.

Enfin, les méthodes d'élaboration des nanoparticules obtenues dans un composite hybride polymère ont été explorées. Parmi les méthodes étudiées, seule la méthode d'infusion permet d'obtenir un nanocomposite avec un réseau de charges percolant, qui confère des propriétés thermoélectriques au matériau. La spécificité du processus de préparation en trois étapes permet d'aligner la majorité des nanotubes de Bi_2Te_3 dans une direction plane. L'inclusion de la matrice polymère isolante conduit comme prévu à des matériaux ayant une conductivité thermique inférieure à celle du Bi_2Te_3 pur. Cependant, cette diminution n'est pas suffisante pour compenser la baisse de la conductivité électrique et du coefficient Seebeck, ainsi, le composite a un ZTmax (apparent) beaucoup plus bas de 0,025. Pourtant, il s'agit du premier exemple de composite hybride massif de Bi_2Te_3 avec une matrice polymère isolante et ses performances thermoélectriques sont comparables à celles de son analogue en couche mince, même si les tubes de la meilleure qualité n'ont pas été utilisés.

Les résultats obtenus sont intéressants à plusieurs égards. Premièrement, la méthode de synthèse assistée par le 1-DDT développée montre la possibilité d'obtenir des nanoparticules de Bi_2Te_3 dans des conditions de réaction relativement douces, contrairement aux méthodes similaires rapportées. Elle montre également comment le contenu morphologique peut être réglé en modifiant les paramètres de la réaction. L'obtention de nanoparticules de Bi_2Te_3 avec différentes teneurs en nanotubes a permis de mettre en évidence que pour améliorer les propriétés thermoélectriques d'un matériau par nanostructuration, ce n'est pas seulement la taille des particules qui compte, mais aussi leur morphologie. Ainsi, après frittage l'échantillon de Bi_2Te_3 avec une teneur plus élevée en nanotubes présente clairement de meilleures performances thermoélectriques par rapport aux échantillons contenant plus de nanoparticules. Troisièmement, l'adoption de la préparation du composite par la méthode d'infusion, qui est habituellement utilisée pour les charges de NTC, démontre la possibilité d'appliquer le processus à des charges plus rigides avec un rapport d'aspect plus faible.

Les travaux futurs du projet devraient commencer par une caractérisation plus approfondie des nanotubes Bi_2Te_3 de meilleure qualité qui ont été obtenus à la toute fin de ce projet de recherche. Les travaux pourraient également porter sur l'étude de la dépendance de la taille des domaines cristallins et du rapport d'aspect des tubes aux conditions de réaction. Plus précisément, il s'agit d'étudier si la taille du domaine cristallin du modèle de Te est en corrélation avec la taille du cristal de Bi_2Te_3 résultant et, si c'est le cas, d'explorer des méthodes pour ajuster la taille du cristal de Te dans le but de gouverner la taille du cristal de Bi_2Te_3 résultant. Le contrôle précis de la concentration en tensioactifs et du rapport

tensioactifs/précurseurs pourrait permettre d'adapter la morphologie des tubes. L'optimisation des conditions de frittage de ces particules à haut rapport d'aspect permettrait d'établir des relations entre le rapport d'aspect des nanotubes et les propriétés thermoélectriques des échantillons frittés. À terme, l'utilisation de ces nanotubes de Bi_2Te_3 de qualité supérieure pour élaborer des mats dans lesquels les résines thermodurcissables seront plus facilement infusées pourrait contribuer à accroître les propriétés thermoélectriques globales de cette nouvelle catégorie de composites polymères conducteurs.

Table of Content

General introduction

Alerting state of the climate change mainly caused by greenhouse effect from fossil fuel consumption and the depletion potential of the last are challenging humanity to switch to alternative energy resources. In this regard, thermoelectric devices which utilize waste heat as an energy source can be a sustainable alternative for energy generation in certain applications. Principles of thermoelectric devices based on thermoelectrical material, which can generate electricity from temperature gradient (heat source) and also can function as Peltier cooler by generating temperature gradient when voltage is applied. Additionally, solid structure of thermoelectric modules without moving parts is expected to provide long lifespan without major maintenance. Despite these advantages of thermoelectrical modules energy generation efficiencies of the known thermoelectric materials are quite low and the best performing ones are composed of rare earth metals. Therefore, currently they are mainly applied in the fields where the cost efficiency is not a concern (99%), as military and space missions. To boost its mass application, many researches are conducted to design thermoelectrical materials with better energy generation efficiency, using both rare and abandoned elements, along with designing economically feasible facile mass production method.

Low temperature thermoelectrics have special potential due to the absence of alternative energy harvesting systems at low temperature gradients and abundance of the low temperature waste heat as body heat or car engines heat. Since its discovery Bi_2Te_3 and its derivatives remain the best thermoelectrical material with intrinsically high thermoelectrics properties owing to its special structure. Over the last 2 decades its thermoelectric properties were vastly improved using various methods. One of such methods is nano-structuring, especially since Hicks postulated that Bi_2Te_3 quantum well can have ZT as high as 14. Nanostructured morphology of Bi_2Te_3 is expected to decrease the thermal conductivity of the material, while thin dimension of nanoparticles is expected to induce quantum confinement effect which improves the electrical transport properties of the material. In combination, both effects lead to improvement the thermoelectrical performance of the material. However, incorporation of these nanostructures into continuous material is another challenging and high energy consuming process. Sintering of nanoparticles into continuous bulk can result in porous structure which decreases the thermoelectric potential of the nanostructures. Additionally, most effective sintering techniques as hot pressing and spark plasma sintering require high energy, therefore expensive.

One way to overcome these drawbacks is to introduce thermoelectric properties in materials whose processing requires less energy. Through this research project we want to explore possibilities to process composite materials based on an easily processable thermoset matrix in which a thermoelectric conductive network made of percolated thermoelectric fillers can be incorporated. In order to lower the percolation threshold and to increase the conductivity of the network, use of highly anisotropic particles is preferable. This explain why the first goal of this research thesis has been to develop scalable and facile methods to prepares Bi_2Te_3 nanoparticles with nanotubular morphology. Then, this project aims to explore methods to prepare polymer hybrid composites with percolating Bi_2Te_3 filler network.

This thesis is reported in three chapters. First chapter is a literature review with the aim to provide a background to the thesis topic in general and into specific topics within it. Chapter 2 describes the developed methods of Bi_2Te_3 nanoparticles synthesis and discusses the effect of the synthesis conditions on the morphology of the particles and thermoelectrical performance of the materials. Chapter 3 describes attempts to prepare hybrid polymer composites via different methods using synthesised Bi_2Te_3 as a filler, followed by thermoelectrical characterization of the hybrid composites.

Chapter I – Literature review

I Introduction

The idea of converting waste heat into electricity by thermoelectric materials is appealing. This led to intensive research in searching the best thermoelectric material. Yet, low conversion efficiency of available thermoelectric materials made the research in the field to broaden by searching different categories of materials. Current state of the thermoelectric material search is thus broad and difficult to systemise, yet with clear aims.

This literature review aims at giving context to the thesis research topic. It begins by introduction of thermoelectricity concept and its development history, followed by presentation of state-of-the-art bulk inorganic thermoelectric materials. The main methods developed to improve the thermoelectric properties and widen their fields of applications are discussed with a particular focus on recently developed solution-based bottom-up methods of Bi_2Te_3 nanoparticles. Since their easy processability is interesting for room temperature applications, organic and hybrid composite thermoelectric materials have also been recently investigated and will be presented in a last paragraph with a focus on the more relevant types of composites such as organic-inorganic hybrids. The last sub-chapter is presented by dissecting individual examples in the relevant topic to allow the reader to understand the broadness of the field.

I.1 Concept and history of thermoelectricity

I.1.1 Discovery of thermoelectric effect

Thermoelectricity is a conversion of temperature difference into electric voltage or vice-versa through a thermocouple, which is made of two thermoelectrical materials (TM). The thermoelectric effect was first discovered by T. J. Seebeck in 1821 when he noticed that a voltage difference is formed in a circuit made by attaching the ends of two dissimilar metal wires when these wires were kept at different temperatures[1,2]. A decade later J. Peltier noticed that the application of a voltage to a thermocouple produces slight heating or cooling depending on the direction of the current. Those two phenomena were later known as Seebeck and Peltier effect correspondingly. However, the interdependency between Seebeck and Peltier effects was only recognized in 1855 by W. Thomson, who established relationship between Seebeck and Peltier coefficients.

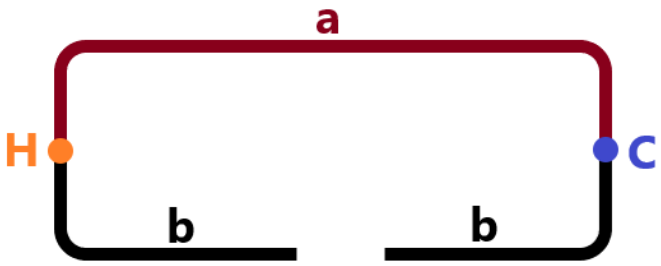

Figure – 1.1. Basic thermoelectric circuit: a and b – different conductors; H and C hot and cold junctions

Figure-1.1 depicts a simple TE circuit which consists of two dissimilar conductors a and b. They are connected at junction points H and C. If a temperature gradient is formed between the two junctions by heating the junction H and keeping the junction C colder, a voltage difference is formed between two b segments which can generate a current if the circuit is closed. When the circuit is open the electromotive force known as Seebeck coefficient is defined as[1]:

$$\alpha_{ab} = \frac{dV}{dT} \qquad (1)$$

Such circuit drives the current in a clockwise direction and Seebeck coefficient have a positive sign. While, if current is applied clockwise to the circuit through the ends of b segments to create a temperature gradient (used as Peltier cooler element), the sign of Peltier coefficient (Π) is negative. Created temperature gradient has hot and cold sides at H and C junctions

correspondingly. While Seebeck can be easily measured experimentally, the Peltier coefficient is calculated from the Seebeck coefficient of the thermocouple or material thanks to the discovery of Thompson[3]:

$$\Pi_{ab} = \alpha_{ab} T \quad (2)$$

Later, as a result of empirical evaluation of different materials, semiconductors found to be more efficient in thermoelectrical application. Highest power output was obtained when two dissimilar materials where replaced one by semiconductor with positive electrical conduction and the second with negative conduction. In semiconductors with positive electrical conduction holes play the role of charge carrier responsible for electrical conduction and materials demonstrates positive Seebeck coefficient. Contrarily, electrons act as charge carriers in the semiconductors with negative electrical conduction and material shows negative Seebeck coefficient. This understanding set the model for the thermoelectric power generator and cooler and materials applied started to be considered in such pairs.

The next discovery which had a weighted contribution to the development of the field was made in 1909 by E. Altenkirch[4]. He mathematically derived a relationship between physical properties of thermoelectric materials and the efficiency of a thermoelectric generator which included electrical and thermal conductivities along with other parameters and coefficients. In 1949 A. F. Ioffe integrated the parameters from Altenkirch derivation into the Z parameter, later known as the figure of merit, in order to evaluate the efficiency of a TM pair[4]:

$$Z = \alpha^2 \frac{(\alpha_p - \alpha_n)^2}{[(\lambda_p \rho_p)^{\frac{1}{2}} + (\lambda_n \rho_n)^{\frac{1}{2}}]} \quad (3)$$

where α – electromotive force (currently known as a Seebeck coefficient and often expressed as S), ρ – electric resistivity, λ – thermal conductivity, subscripts p and n stand for the materials with positive and negative electrical conduction. Higher the Z, better the performance of TM pair.

In selection of TM materials for TM pair, it is more reasonable to optimize and characterize each constituent material (n or p) separately. It can be done by figure of merit of single material z, which defines the performance of single material:

$$z = \alpha^2 \frac{\sigma}{\lambda} \quad (4)$$

where σ – electrical conductivity. The Figure of merit of the pair (and the device) then is average of two "z"s for two constituents.

The Figure of merit[4] is widely used to evaluate the TMs as their main characteristic for generation of both electricity and cold. However, all the parameters allowing to evaluate the Figure of merit vary with temperature, Therefore, it should be considered as a function of temperature rather than a single number. Comparing functions is bit difficult than the single characteristic values, therefore the temperature value is introduced to the characteristic of the TMs and earlier known z with the unit of [K^{-1}] becomes the "Dimensionless figure of Merit" zT. Thus, reported zT for the materials is the maximum value measured at the optimal temperature.

$$zT = \frac{\alpha^2 \sigma}{\lambda} T \qquad (5)$$

The nominator of the equation (5) is known as a power factor (PF) and often used to evaluate the TMs along with zT, especially when measuring thermal conductivity of the material is difficult as in the case of thin films:

$$PF = \alpha^2 \sigma \qquad (6)$$

From the equation (6) it is clear that to obtain high zT material should have PF ($\uparrow\alpha^2\sigma$) and small thermal conductivity (λ) at a given temperature. Combination of these requirements is tricky to realize, because all three parameters are interrelated as we will explain later on.

To simplify further the comparison between thermoelectric materials, three categories have been defined depending on the temperature range of maximum zT (also stated as application temperature): Low temperature (below 453K), intermediate temperature and high temperature thermoelectric materials (>900K). It is only reasonable to compare zTs of materials belonging to the same category.

Derivation of these equations which allow to evaluate the performance of single materials and recognition of semiconductors and doped semiconductors as suitable materials for TE application in early 1950s[5] fuelled the development of the field for the next two decades until 1970 when started a second stagnation period[1]. Nevertheless, the field of TE materials vastly advanced since the 1990s driven by environmental concerns (both related for current refrigeration systems impact and the need for alternative energy sources) and new discoveries as a size related effect (quantum confinement effect by Hicks[6]), microstructure[7] effect and band gap engineering[8] which opened wide opportunities to optimize the material properties. These

methods and related developments will be discussed in the following chapters as current and ongoing methods of optimizing the performance of existing TMs and creating new ones.

Two kinds of device use the phenomenon of thermoelectricity: thermoelectric generators (TEG) which generate electricity from heat source and thermoelectric coolers (TEC) which produce temperature gradient in the thermoelectric module upon application of current, thus used as cooler[9,10]. A schematic representation of a basic TEG unit consisting of single TM pair is depicted on Figure-1.2a. It consists of two conductor units one with positive (P) and the other with negative (N) charge carriers connected electrically in series via a metallic conductor and thermally in parallel. Interconnecting metal conductor has a low Seebeck coefficient which is considered as 0. Application of heat at heat source and keeping the heat sink at lower temperature creates a temperature difference between the two ends of the thermoelectric materials leading the charge carriers (electron and holes) to diffuse from hot to cold side and creating an electric current in the circuit. Simple TEC unit, depicted on Figure-1.2b has similar construction, however the temperature gradient created by applied current has opposite direction. Actual TEG consists of multiple of thermocouple units connected in series electrically and in parallel thermally (Figure-2c). Each thermocouple pair produces electrical potential upon application of heat difference and total electromotive force of the device is generated by summing up these potentials. Consequently, the higher the number of the thermocouple pairs in the circuit the higher the performance of the device.

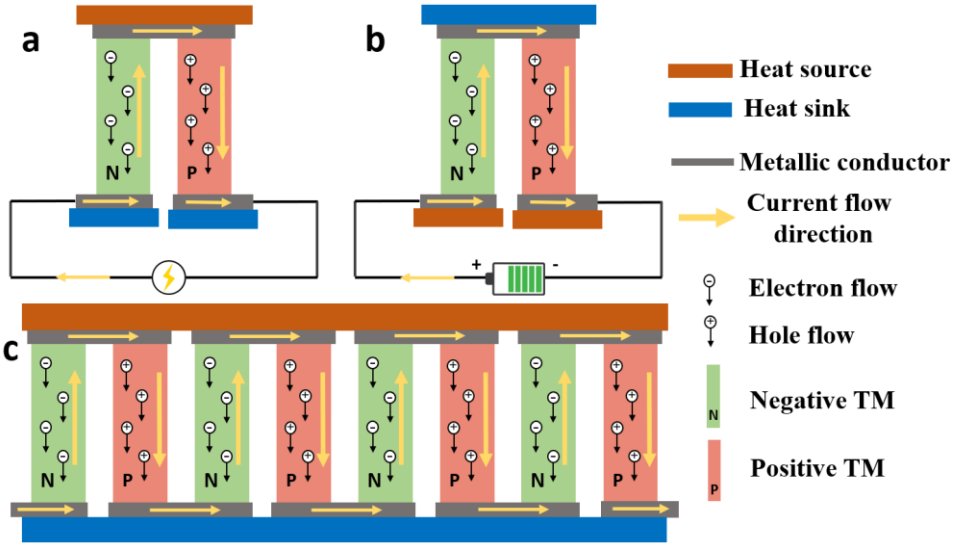

Figure – 1.2. Schematic representation of: a) TEG unit with single thermocouple; b) TEC with single thermocouple; c) Practical TEG unit with interconnected multiple thermocouples

Whereas the dimensionless figure of merit allows to compare the intrinsic performance of thermoelectric materials, the efficiency of materials or devices (TEG or TEC) also needs to be calculated and compared with other available electricity generators and coolers in order to evaluate the viability for commercial application. The efficiency of TMs is calculated using the following equation[10,11]:

$$\eta = \frac{(1+zT_m)^{0.5}-1}{(1+zT_m)^{0.5}+\frac{T_C}{T_H}} * \frac{T_H-T_C}{T_H} \qquad (7)$$

where T_H – temperature of heat source; T_C – temperature of heat sink; $T_m = \frac{T_H+T_C}{2}$

The efficiency of current thermoelectric materials ranges mainly from 5% to 15%.[4,12] The same equation is used to estimate the TEG efficiency only by replacing the figure of merit of single material by figure of merit of the device (Z). Despite the intriguing concept of thermoelectricity, efficiency of current TEGs remains lower than most other power generation systems (vapor compression, photovoltaics (27%))[13]. Therefore, their main application niche remains to be military and space engineering (>90%)[14] where the cost of produced energy is not a concern. One of the famous applications of TEG is in space missions. For example, the Perseverance rover send to explore Mars is powered by TEG based on PbTe. Yet, it does not utilize waste heat, but the heat is supplied by decay of a radioactive element. Other industrial applications of thermoelectric modules take only few percent of the market and mainly thermoelectric coolers.

The highest zT of current TMs reached values around 2.5 (PbTe[15] and SnSe[16]). Physical laws do not prohibit the increase of either zT or material and device efficiencies. Therefore, the search for better performing TM continues intensively. Low temperature (near room temperature) materials are of particular interest since at small temperature differences (5°C) they can surpass the efficiency of other power generator systems when ZT is around 1[13]. Nevertheless, the progress made in understanding the influence of the materials structure on their performance and the possibilities opened by technology for tailoring and monitoring this structure pushed the field further. These novel methods to "tailor controlling" the TM performance, which is current state of the art for the last decades, are discussed in the following chapter.

I.1.2 State-of-the-art Bulk TMs

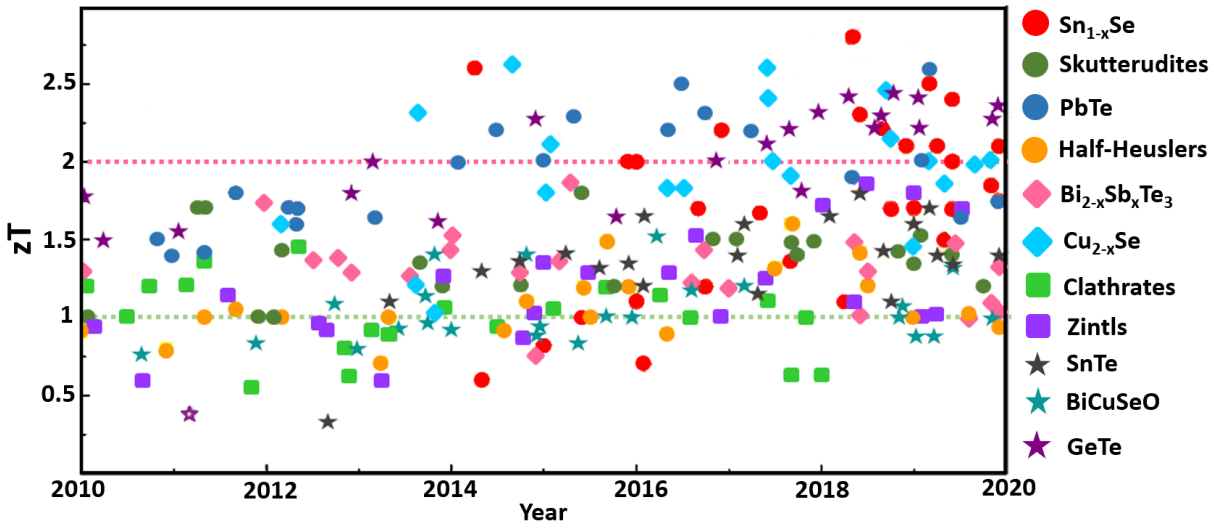

Figure – 1.3. Evolution of zT for state-of-the-art bulk TMs over the years[17]

Bismuth chalcogenides (Te, Se, Sb) remain to be the best performing TMs for room temperature application for decades[18]. Their remarkable performance is rationalized by their layered structure which provides intrinsic low thermal conductivity. Possibility to tune the conduction type (n or p) by slight changes of the composition makes bismuth chalcogenides excellent TM for commercial application. They are based on Bi_2Te_3 structure in which either Bismuth or Tellurium are partly replaced by respectively Antimony or Selenium (called dopants) to tune the thermoelectric properties. Thus, $Bi_xSb_{2-x}Te_3$ is an excellent p-type semiconductor with a zT around 1.8 around 300K[19–21], while a n-type representative of the class can be $Bi_2Te_{3-x}Se_x$ with zT values close to 1[22]. Excellent solubility of dopants in the structure[23] allows to enhance further the intrinsically high zT values of the bismuth chalcogenides by different structuring techniques, thus the research in optimization of their TE characteristics is ongoing as will be discussed later in this chapter.

Chalcogenides of lead, notably PbTe is the best-known TM widely applied in space exploration missions (often called superstar of TE field)[24]. PbTe structures with zT as high as 2.5[25] at around 900K have been reported. Such a high zT arises from the combination of high power factor and low thermal conductivity in the structure. High power factor is explained by highly symmetric rock-salt crystal structure. Their high melting temperature and the stability of the structure makes them suitable for mid-temperature applications. Similar to the Bi chalcogenides, PbTe structure allows to obtain high performing n and p type conduction by facile tuning of the doping. *Chalcogenides of tin* is another class of excellent TMs, and in

comparison with PbTe and Bi_2Te_3, they are considered as less-toxic and more cost efficient. Two remarkable representatives of the class are SnS and SnSe. p-type SnS demonstrates zT as high as 1.6[26] (around 900K), while p and n-type SeSn are reported to have zTs as high as 2.3[27] (~ 900K) and 2.8[16] (~ 773K) respectively.

Another class of TMs is Half-Heusler alloys which typically have three metallic composition: early transition, late transition and heavy main group metals. The maximum zTs achieved for Half-Hausler alloys are below the values of above discussed chalcogenides: 1.5 at 1200K for p-type FeNbSb alloy[28]. Nevertheless, they are widely investigated due to their stability at high temperature and consequent potential as high temperature TM[29]. Such potential is rationalized by the fact that they meet most of the requirements for commercial application such as easy matching of n and p counterparts, relative abundance and low cost, high mechanical properties and thermal stability. Half-Heusler alloys have $F\bar{4}3m$ (216) cubic space group[30] which provides high power factor, however low zT values arise from high thermal conductivity. The last can be decreased by different structure tailoring techniques.

Clathrates (inorganic) structurally differ from other TMs classes. They consist of two substructures – a rattling guest in a clathrate framework which are specially separated[31]. Covalent bonding in the clathrate framework provides high electrical conductivity to the material, while the rattling guest atom inside the oversized framework, which acts as a cage, scatter the phonons, thus low thermal conductivities are obtained. High zT values as 1.45 at 500 K was reported for $Ba_8Ga_{16}Sn_{30}$ clathrate[32]. This value is lower than the zT of Bi chalcogenides for near room temperature application, but structural tailoring (phonon engineering) promises great enhancement of this value by further decreasing the lattice thermal conductivities of clathrates.

Skutterudites have a complex crystal structure with the unit cell consisting of 8 cubes[33] (made of transition metals and denoted as T in the structure below). 6 out of these cubes are filled with pnictogen (Pn, elements of 15 group) while two remains empty (□), giving the structural formula of $\square_2T_8Pn_{24}$. Unfilled skutterudites usually possess low TE characteristics, while filling the empty cubes with guest atoms in a cage manner causes the rattling effect and scatter the phonons. This phenomenon raised interest in in them as potential TMs and zT of 1.8 at ~800K was obtained for $\square_2Co_4Sb_{12}$ structures partially or fully filled with Sr, Ba or Yb atoms.[34]

Other state of the art classes of bulk TM materials are Zintle phases, silicides, copper chalcogenides, TAGs and etc[17]. The developments of zT values over the past decade for bulk TM material classes (or one representative from the class) are represented on Figure-1.3 (adapted from reference[17]) and show great enhancement for most of them for the last several years.

I.2 Enhancement of thermoelectric performance of materials/device

As mentioned earlier thermoelectric performance of the material and thermocouple is evaluated by its dimensionless figure of merit:

$$zT = \frac{\alpha^2 \sigma}{\lambda} T \qquad (6)$$

According to the equation (6) t to obtain a high zT, a material should have a high Seebeck coefficient (α), high electrical conductivity (σ) and a small thermal conductivity (λ) at a given temperature. However, the combination of these requirements is tricky to realize, because all three parameters are interrelated. The increase of one leads to unfavourable increase or decrease of the others: exp., conventional increase of electrical conductivity leads to decrease of the Seebeck coefficient and increase of the thermal conductivity.

The values of α, σ and λ are interrelated through the carrier concentration *n*, which in turn depends on the level of doping. To adjust the level of doping to its optimal value, the influence of n on each parameter should be understood. With certain assumptions (the semiconductor is degenerate, band dispersion is parabolic, dopant does not affect the band structure significantly, some of were proven to be not true, but the equation remained to be applicable[1]), the Seebeck coefficient can be expressed as[35]:

$$\alpha = \frac{8\pi^2 k_B^2}{3eh^2} m^* T \left(\frac{\pi}{3n}\right)^{2/3} \qquad (8)$$

k_B – Boltzmann constant; *h* – Plank constant; e – electron charge, m* - density of states effective mass. Inverse proportionality between α and *n* in equation (9) allows to conclude that the Seebeck coefficient will drop when increasing the carrier concentration. Meanwhile, the electric conductivity is directly proportional to the carrier concentration, thus a high concentration of carrier leads to an increase of the σ (μ – carrier mobility):

$$\sigma = ne\mu \qquad (9)$$

To understand the influence of the carrier concentration on thermal conductivities, the last should be divided into its constituents: electronic thermal conductivity – κ_{ele} and lattice thermal conductivities – κ_{lat} ensured by phonons:

$$\kappa = \kappa_{ele} + \kappa_{lat} \qquad (10)$$

The influence of *n* on lattice thermal conductivity of the material is negligible, therefore it is considered as single parameter and not affected by it. This independence opens a possibility

to decrease the overall thermal conductivity by favouring phonon scattering without distorting the other properties. Nevertheless, electronic thermal conductivity directly depends on electric conductivity and subsequently on carrier concentration via Wiedemann-Franz equation (L – Lorenz factor):

$$\kappa_{ele} = L\sigma T = Lne\mu T \qquad (11)$$

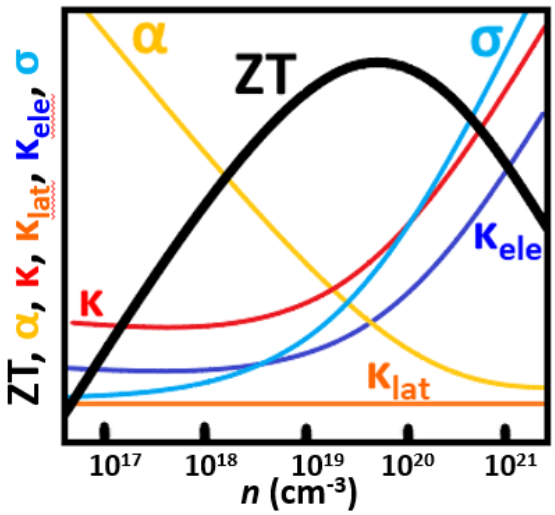

Figure – 1.3. Dependence of ZT and related parameters (α,σ, κ) on carrier concentration (the trends were adopted from reference[23] which in turn was plotted using the data from reference[36] for Bi_2Te_3)

Figure-1.3 illustrates the above discussed dependencies of ZT and its parameters on the carrier concentration. Despite this complicated dependence of parameters on *n*, it is yet possible to identify the most suitable carrier concentration for the best performance of a thermoelectric material (maximum ZT). Such trends should be identified for each system individually, but for most of the semiconductors the optimized carrier concentration lies between 10^{19} and 10^{20} cm^{-3}. [37] Considering the influence of each parameter defining the ZT and their inter-dependency, different strategies have been established to improve the thermoelectric properties of semiconductors and they are briefly presented hereafter.

I.2.1 Doping Strategies

Doping is the most established method to enhance the thermoelectric performance of semiconductors. Generally, it is a process of inclusion of elements into the structure of semiconductor to optimize its carrier concentration. Nevertheless, this theoretical optimal n (Figure-1.4a black line) which results in the best ZT at a given temperature (Figure a.4b and c, black lines) is not constant and increases with temperature according to the power law of $T^{1.5}$.

For conventional doping methods the *n* does not vary with temperature (Figure-1.4a, green line). As a consequence, at low temperatures the n is higher than its optimal value and lower at high temperatures and only at one temperature the optimal *n* and correspondingly maximum ZT is reached (point A in Figure-1.4a).

In order to obtain values, close to the optimal n at different temperatures, the strategy of graded doping has been developed. These thermoelectric materials are made of several segments (two or more) with different levels of doping[23,38]. The performance of graded TM is compared with performances of its low and high doped segments on Figure 1.4b. Grated doping, allows indeed to approach the ZT curve at optimal n (black line) in contrast with its segments and conventional doping (Figure-1.4c, green curve). Such graded doping have been realized[39], however, due to the diffusion, after number of cycles materials performance drops vastly.

An alternative approach to maintain optimal *n* when the temperature varies is to apply T-dependant doping[23,38]. It relies on using certain dopants which have T-dependant solubility in the host material. This method indeed allows to reach values (Figure-1.4a red curve) close to the optimal n on a wider range of temperatures and as a consequence approach the optimized ZT values (Figure-1.4c red curve). In contrast with graded doping, T-dependent doping does not present diffusion related issues.

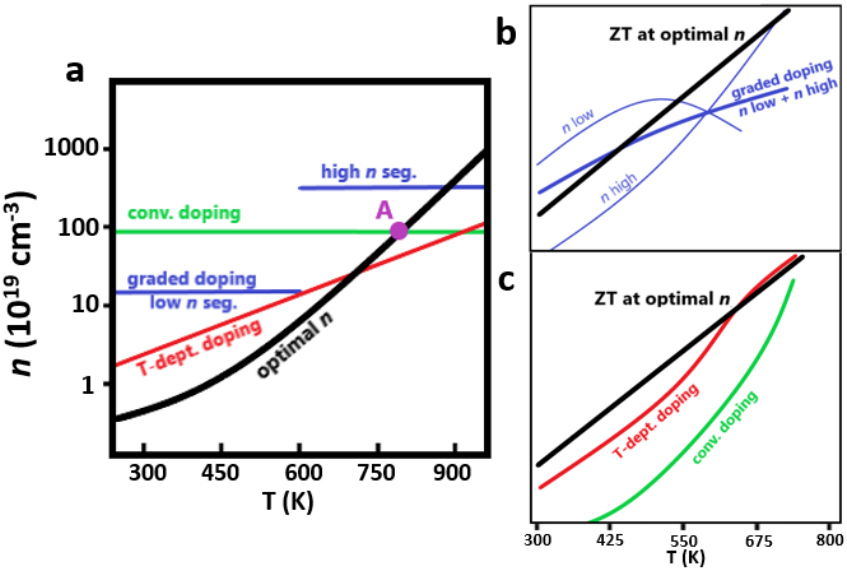

Figure-1.4. Schematic representation of variation of a – carrier concentration (*n*) b – ZT with temperature via different doping methods[23]

I.2.2 Electronic tailoring

When the maximum achievable zT is already reached by the most optimal *n*, the next strategy to increase further the zT is to tailor the electronic structure[23]. Electronic structure tailoring is also reached by doping, but with assumptions that doping does not influence the electronic and phonon structure significantly (scattering), but only affects the chemical potential[8]. In such case the zT depends only on atomic and electronic structure of the materials and it is determined by the dimensionless thermoelectric quality factor[40]:

$$B = \left(\frac{k_B}{e}\right)^2 \frac{2e(k_B T)^{3/2}}{(2\pi)^{3/2}\hbar^3} \frac{N_V \mu_0 m_b^{*3/2}}{\kappa_L} T \qquad (12)$$

where N_V – band degeneracy; μ_0 – mobility of nondegenerate limit; m_b* – carrier effective mass.

The dependence of zT on B factor is expressed with a more complex equation which apart from B factor contains more complex parameters which is out of the scope of this literature review, but in short, higher zT is obtained at higher B factor values. Increase of B factor so far have been realised by two main methods, which are increasing number of degenerate valleys (N_V) or carrier effective mass m_b*. Both methods rely on careful selection of dopant and doping level, which leads to favourable distortion of the crystal structure and bands.

N_V highly depends on the symmetry of crystal structure: higher the symmetry higher the N_V. Thus, in order to *increase the N_V* the symmetry of the crystal structure should be increased. This was demonstrated by Zhang et al.[41] by distorting non-cubic tetragonal structure of two chalcopyrites by mixing them and creating total pseudo-cubic structure. This allowed to obtain an overall higher zT.

A second way to increase the N_V is *to converge different bands*. Such approach was successfully realized on SnTe, which is considered as environmentally friendly substitution of PbTe. Pure SnTe is poor TM because its Σ valence band is unavailable for charge transport due to high energy gap of $\Delta E_{L\text{-}\Sigma}$=0.35eV[42] between L and Σ valence bands. In general case the N_V of the Σ valence band is higher than the N_V of the L band, and converging the bands by decreasing $\Delta E_{L\text{-}\Sigma}$ allows to achieve an effective N_V which is usually higher than the N_V of the Σ valence band. Doping of SnTe with Mn, allowed indeed to achieve such an effect which resulted in tremendous improvement of the Seebeck coefficient and PF of $Sn_{1-x}Mn_xTe$.[43] This finding is notable, because earlier inefficient material showed TE properties comparable with

the state-of-the-art materials (PbTe). Therefore, this method is considered as promising to tune the poor TMs into good ones.

The increase of carrier effective mass m_b*can be achieved by *band flattening effects*[23]. The last in turn achieved by doping the structure with atoms which have strongly localized orbitals. Such substitution decreases the overlap of orbitals and leads to an increase of m_b* (mainly increases the Seebeck coefficient). However, the increase of m_b* leads to a decrease of the carrier mobility (μ), thus to the decrease of the electrical conductivity (equation 12). This adverse effect can be overcome only at high levels of doping; therefore, band flattening is considered to be effective only at high levels of doping. Solid example of band flattening effect is substitution if Sr in $SrTiO_3$ by La.[44]

Another way to increase the m_b* is by the introduction of *resonance level*.[45] This is done by the introduction of a small amount of impurities-dopant. With proper selection of the dopant, their electron couples with valence or conduction band electrons of the main semiconductor. This gives rise to an additional density of states at resonant energy and increases the m_b*. This improvement only takes place at low temperature, as at high temperature the resonance level effect diminishes.

Electronic tailoring methods require in depth understanding the effect of structure on each component of the TE properties of TM. The main challenge is to distinguish the improvement of zT arising from targeted effect from the additional effects likes phonon scattering raised from crystal structure distortion and etc. Nevertheless, some methods of electronic tailoring are promising, especially when the possible maximum zT is reached by increasing the carrier concentration adjustment.

I.2.3 Reduction of Lattice Thermal Conductivity

The concept of "Phonon glass, electron crystal" (PGEC) material asserts the design of the structure which allows low thermal conductivity as in the glass (by restraining the thermal lattice thermal conduction via phonon scattering) and electrical conductivity as in the semiconductors[46]. This concept was introduced nearly 3 decades ago by Glen Slack and remains to be leading concept to design the best performing TMs. As a part of this concept, great deal of research is directed to reduce the thermal conductivity (κ) of TM. The only way to do it without deteriorating the other properties of TM is to reduce only the lattice thermal

conductivity – κ_{lat} component of κ. The lattice thermal conductivity arises from propagation of phonons through the lattice of the crystal. Phonons are heat carriers in a form of vibrational waves of different wavelength and are created as a result of displacement of atoms from their positions at equilibrium due to the inter-atom interactions. The defects in the crystal structure can scatter the phonons instead of propagate them which leads to a decrease of the lattice thermal conductivity. Phonons have different wavelength and in order to be able to scatter the phonon these structural defects must have similar dimensions.

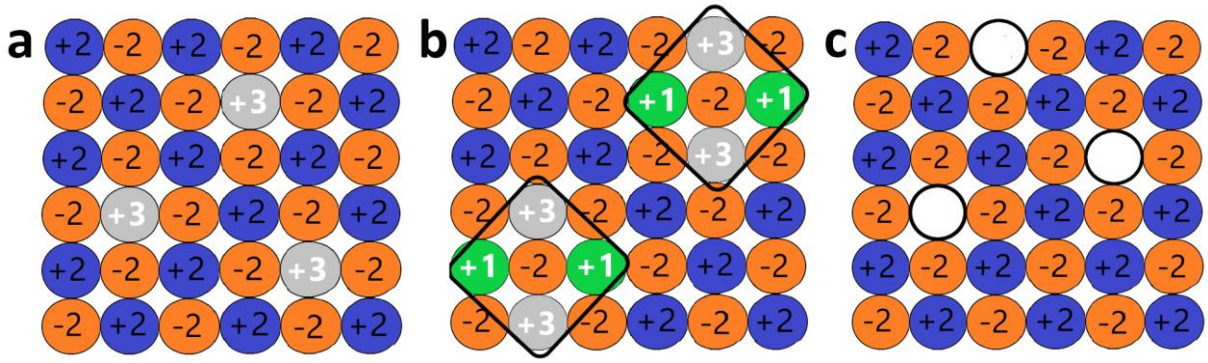

Figure-1.5. Point defects created by: a – aliovalent single doping; b – cross-substitution; c – lattice vacancy

Point defects, otherwise known as atomic scale defects have the ability to scatter phonons of several Angströms wavelength. The main types of point defects introduced by doping are represented in figure-1.5[23]. First method (Figure-1.5a) consists in replacing certain atoms in the structure by a single dopant which leads to κ_{lat} reduction by creation of lattice disorder. The efficiency of κ_{lat} reduction increases with increase of lattice disorder which is obtained when the valency of dopant is different than that of the host atoms. However, the solubility of the dopant atom is limited when the valences do not match, therefore the doping level is limited at low. The solubility problem is solved by the cross-substitution approach (Figure-1.5b) where the host atoms are replaced by pairs of dopant atoms with different valences which overall allows to keep the valence electron amount in the structure constant. This approach is proven to be more effective than the previous. Another way to create point defects is to introduce vacancies in the structure (Figure-1.5c), either on dopants or host atoms positions. Such vacancies are observed in partially filled skutterudites[47] and clathrates[48] (due to void cages).

In order to scatter the phonon with higher wavelengths nanoscale and mesoscale defects should be introduced into the structure. Defects up to 100 nm (usually several tens) are

considered as nanoscale defects. They must be homogeneously distributed in the structure in order to obtain efficient phonon scattering. The most reliable method to reach such distribution is by second phase precipitation ("in-situ") which produces bulk crystals with nanosized second phase impurities. It can be achieved when the impurity and the host are completely miscible in the molten state, but do not form solid solutions. When this criterion is met, the molten mixture of the two components is cooled down rapidly which results in a fine distribution of nanoscale defects in the bulk crystal which effectively scatters the phonons of corresponding sizes, and thus increases the zT of the material. Bi_2Te_3 with nanosized Cu or Zn inclusions[49] can be considered as a good example of such improvements of zT among many others.

Phonons with the highest wavelength range can be effectively scattered by mesoscale defects. In deference with all the above methods, introduction of mesoscale defects is not realised by doping with a second phase or atoms, but by breaking down bulk crystals into mesoscale grains and assembling them into a polycrystalline bulk material. Typical range considered as mesoscale is from 100 nm up to 3-5 μm. The high wavelength phonons are scattered by grain boundaries. The common methods to assemble the grains into continuous bulk are hot pressing and spark plasma sintering. One of the first examples which proved of the effectiveness of the concept is SiGe[50]. Alloys of SiGe consisting of grains less than 5 μm showed 20% reduction of thermal conductivity in comparison with single crystal sample.

Mesoscale structuring can be obtained by two main routes: top-down or bottom-up[23,37]. Top-down preparation is realised by breaking down big coarse crystals (sometimes single) into fine powders of required particle sizes. Common top-down methods are mechanical grinding, ball milling, spattering[51] among which ball-milling is being widely used for TMs due to is cost effectiveness. In bottom-up approach particles are grown into required sizes from molecular precursors. Common bottom-up methods are chemical vapour deposition, hydrothermal, solvothermal, aqueous synthesis, or electrochemical deposition. In some cases, bottom-up synthesis produces polycrystalline mesoscale particles, with nanosized crystal domains. Utilization of such particles promises to scatter phonons in both meso and nanoscales.

Nevertheless, defects introduced to scatter phonons can also scatter electrons, resulting in the decrease of the electronic conductivity thus TE properties of TM. Thus, to have a net positive impact the phonon scattering efficiency should be much greater than the adverse effect of electron scattering.

I.2.4 Quantum confinement

The tremendous influence of mesoscale structuring on the reduction of lattice thermal conductivity raised interest in low-dimensional materials synthesis such as nanoparticles. This interest was later fuelled by the introduction of quantum confinement effect in quantum-wells by Hicks and Dresselhaus at the beginning of 1990s[6], which suggests the improvement of PF of materials in thin nanoscale structures.

Quantum confinement effect in thin quantum wells raised interest in application of superlattices thin films as TMs[52]. Superlattices are layered structures consisting of alternating layers of two materials with different conductivities. The layer with higher conductivity acts the role of conduction layer while the second layer acts as a barrier. The thickness of layers required to be sufficiently thin to ensure transfer of charge carriers in 2D quantum-well. It enhances the electronic properties of the material and low thickness of films provides low thermal conductivity to the material. Nevertheless, integration of thin films into devices comes with costs as difficulties to attach. Another direction developed with introduction of quantum confinement effect is to synthesize nano and mesoscale 2D materials as nanorods and nanowires and also 3D nanotubes which can transfer charge carrier through its thin confined wall. These low dimensional materials can be integrated either into a superlattice or into a bulk.

Improvement of thermoelectrical properties of semiconductors by the last two mentioned techniques – reduction of lattice thermal conductivity and induction of quantum confinement effect requires preparation of nanoscale materials. The next sub-chapter, in this regard, discusses synthesis methods of Bi_2Te_3 nanoparticles.

I.3 Bismuth Telluride nanoparticles synthesis

Since the great influence of phonon scattering at grain boundaries on the reduction of thermal conductivity and possibility to increase the power factor by quantum confinement effect were discovered, the interest in low dimensional materials increased tremendously. To give a context to the experimental section of the thesis, in the current section of literature review common techniques to prepare low dimensional TMs will be discussed in the example of Bi_2Te_3 nanoparticles.

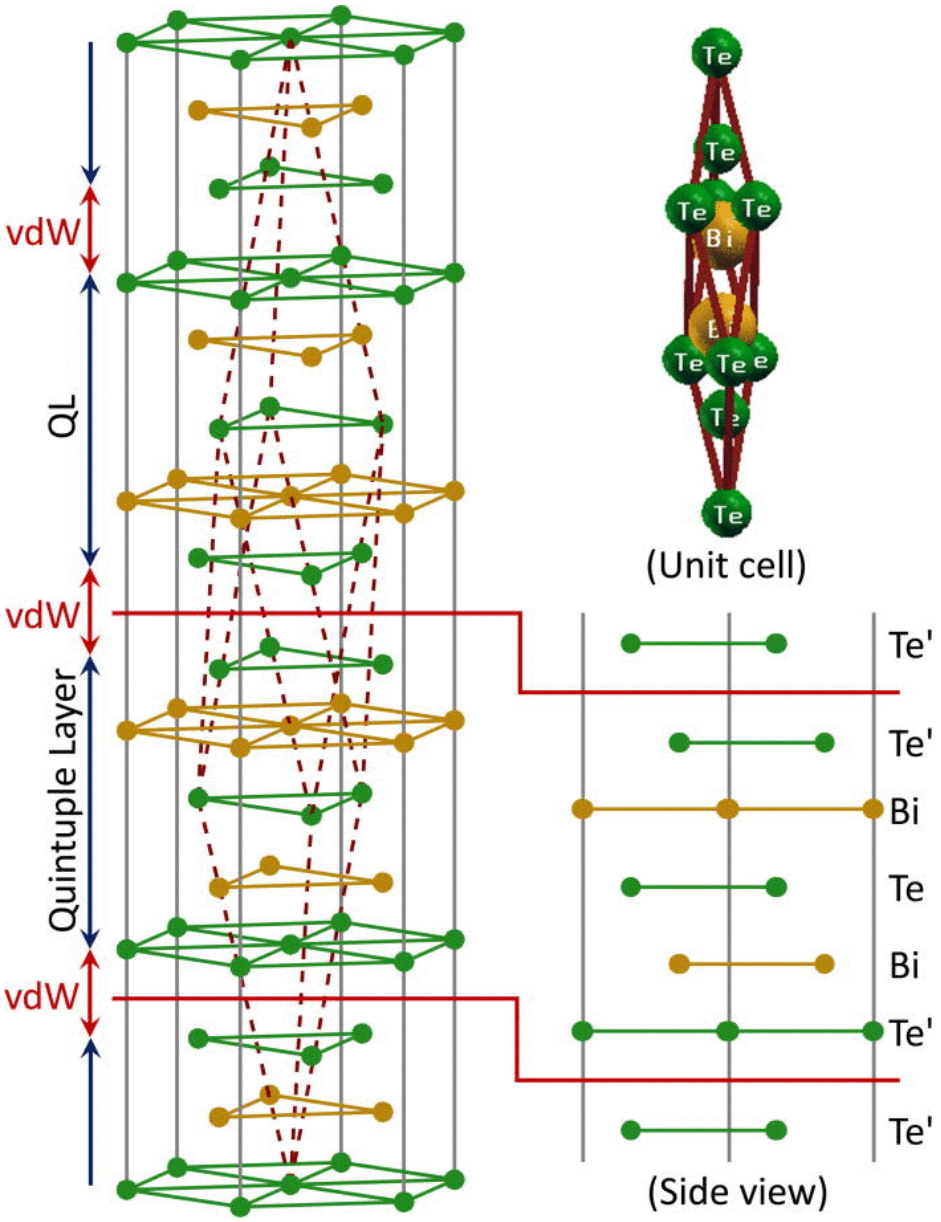

Figure-1.6. Crystal structure of Bi_2Te_3[53]

Since the discovery of applicability of semiconductors as effective TM, Bi_2Te_3 was and remains to be intrinsically high performing TM for room temperature applications, not only in

TEG, but also in TEC and topological insulators[54]. Excellent performance of Bi_2Te_3 relies on its highly anisotropic rhombohedral tetradymite-type crystal structure with R-3m space group and layered arrangement of atoms[54,55]. The unit cell of Bi_2Te_3 is formed by the stacking of three quintuple layers (Te'-Bi-Te-Bi-Te') along [001] direction. The van der Waals (vdW) coupling between adjacent quintuple layers through Te' atoms is much weaker than that covalent between Te and Bi inside the quintuple layer. Such arrangement results in 7 times longer c lattice parameter than a and b, thus highly anisotropic properties. Increased interest in Bi_2Te_3 nanoparticles increased after Hicks and Dresselhaus calculated that Bi_2Te_3 nanowires with diameter of 5 A can demonstrate zT of 14[7], while application of Bi_2Te_3 in superlattice can show zT of 13.[6]

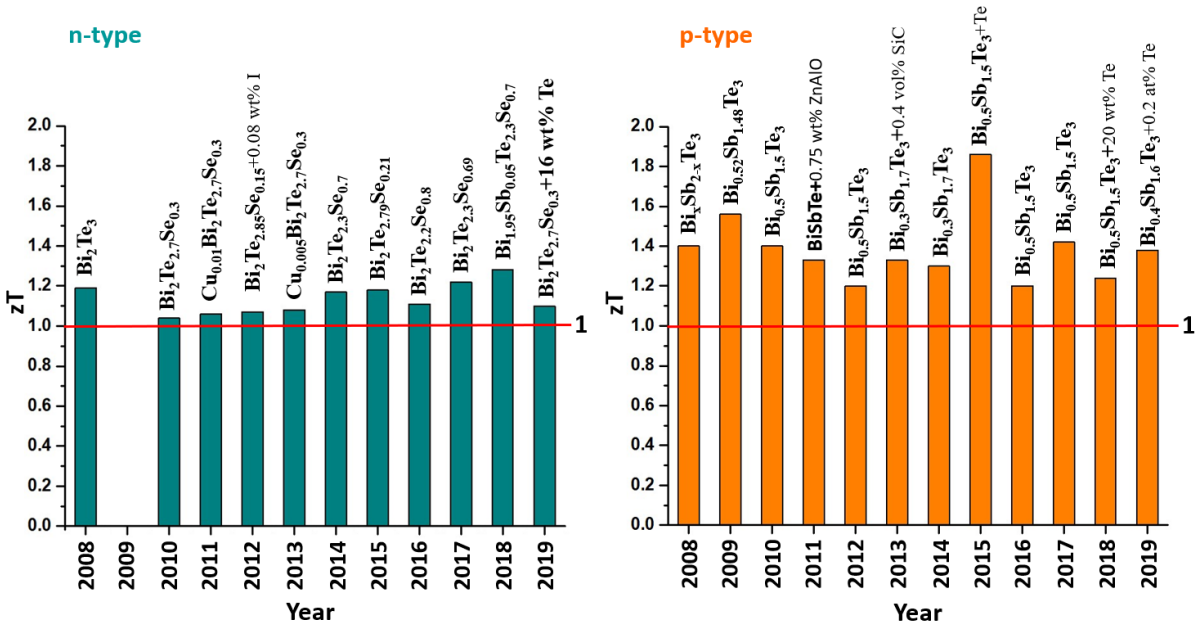

Figure-1.7. Bi_2Te_3 and related TMs with highest zT reported (adopted from reference[56])

Preparation of low dimensional materials, including TMs and Bi_2Te_3 nanoparticles, as mentioned earlier, firstly can be divided into top-down and bottom-up methods. Top down methods first require having a pure bulk structure, then divides it into small particles using different grinding techniques like mechanical grinding, ball milling and others. The main drawback of the top-down method is the lack of control over the morphology of the particles, except size. It results in possible enhancement of zT only by the decrease of thermal of the conductivity. Bottom-up methods are synthesis of nanoparticles from atomic and molecular scale precursors. Physical or chemical methods have been used for this purpose.

The principal physical methods are (co-) evaporation methods[57–59], sputtering methods[60–62], and pulsed laser deposition[63]. The main drawback of these methods is once again the lack of the control over the morphology of particles, but also a relatively high cost and a difficulty for big scale production. Yet, physical methods are effective to prepare nanostructured thin films.

The main chemical methods are aqueous solution synthesis, hydrothermal synthesis, solvothermal synthesis, electrochemical deposition, galvanic displacement, and chemical vapor deposition. Among these chemical methods electrochemical and chemical vapor deposition (CVD) should be discussed together and separate from others. Both methods are generally applied to prepare thin films on a substrate and mainly result in nanostructured thin films. Nevertheless, fine nanowires can also be obtained by electrodeposition under proper selection of substrate and deposition conditions.[64,65] Most often used substrates to prepare nanowires are polycarbonate and anodic aluminium oxide which define the morphology of the wires.[64] Structural properties of wires, such as density and composition, are defined by the deposition conditions. Most common solution used for the electrodeposition of Bi_2Te_3 is a solution of Bi^{3+} and TeO^{2+} in nitric acid. Freestanding nanowires can be obtained after selective removal of the substrate. Reported diameters of the nanowires synthesized by electrodeposition mainly varies from 15 nm[66,67] to 70 nm[68] and few with diameters exceeding 200 nm[69]. CVD reported to produce mainly grained and porous continuous films[70,71] on different substrates, but also size controllable nanoplates[72] and mixture of nanoplates with nanowires[73,74]. Yet, synthesis of morphologically pure nanowires by CVD was not reported.

Another notable method to prepare Bi_2Te_3 nanostructures is galvanic displacement. Upon careful selection of the displacement conditions and sacrificial template, this method promises to obtain any targeted morphology in terms of shape and size[75]. However, so far only 1D structures of Bi_2Te_3 particles such as nanowires[76], nanotubes[77] and composite belts[75] prepared by galvanic displacement were reported. Common templates are Ni, Cu and Co wires. Electrochemical reaction takes place in the acidic (nitric acid) solution/dispersion of Bi^{3+} and $HTeO_2^+$ (or TeO_2^+) precursors and templates.

The rest of the above listed chemical synthesis methods can be assembled into one category – so called wet chemical synthesis methods, because the synthesis takes place in a solution phase and follows few common reaction mechanisms. Those methods are hydrothermal, solvothermal, aqueous solution (sometimes referred to as aqueous reflux) and polyol synthesis methods. Also, few examples of Bi_2Te_3 nanoparticles synthesis in different

solvents under reflux or just elevated temperature (no pressure) were reported.[78] The main advantages of these methods are the possibility to obtain a wide range of morphologies (both shape and size) as rods, tubes, platelets, belts, flower-like, hexagonal sheets and the scalability of the process.

The most common reaction mechanism in a wet chemical synthesis is a redox reaction[79,80] and can be summarized as following:

1. *Reduction of Te precursor.* Common Te precursors are metallic Te particles, TeO_2 and Na_2TeO_3. After introduction into the solution they are reduced mainly by $NaBH_4$, KBH_4 or $N_2H_4*H_2O$ into different reduction states depending on the precursor and other species in the solution. When water is used as solvent (aqueous and hydrothermal), usually NaOH is added to control the pH of the solution. In those cases, along with the reduction of Te precursors its dissolution by disproportionation is claimed to take place.
2. *Addition of Bi precursor.* Commonly $BiCl_3$ and $Bi(NO_3)_3*5H_2O$ are used. Mostly they are directly added to the solution and produce Bi^{3+} upon dissolution.
3. *Redox reaction.* Redox reaction between Bi^{3+} and reduced Te precursor produces Bi_2Te_3. This reaction takes places upon reaching the set reaction conditions (temperature and pressure). Exact mechanism of the reaction depends on the reduction state of the Te precursor and other species present in the solution, but all lead to the formation Bi_2Te_3. This step, along with composition of the final product, defines its morphology. Morphology is governed by once again reaction conditions (method, temperature, concentration and etc.) and surfactant.
4. *Purification.* Due to the complex composition of the solution (balancing ions of precursors, oxidation product of reducing agent, surfactant and etc) and high surface area (sometimes porous structure) of the Bi_2Te_3 nanoparticles, the product can be contaminated upon separation from the solution. Purification of nanoparticles based on the fact that the pollutants are soluble in different solvents and implemented mainly by filtration washing or centrifugation in different solvents.

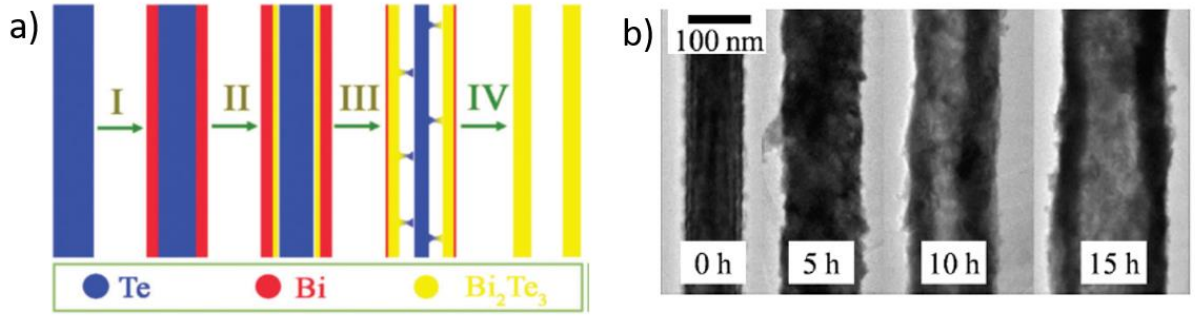

Figure – 1.8. Formation of Bi_2Te_3 nanotubes from Te rods by nanoscale Kirkendall diffusion: a – schematic representation[81]; b – experimental TEM observation[82]

Another common mechanism followed by wet chemical synthesis methods is low-dimensional Kirkendall diffusion[81]. This method involves utilization of Te templates in a metallic state as Te precursors and the morphology of the resulting product is governed by the morphology of this template. Trigonal tellurium, due to its anisotropic crystal structure, has a tendency to grow in one direction[83], therefore, upon recrystallization mostly produces elongated shapes as rods. As a result of utilization of rod-type Te precursors, reported Bi_2Te_3 obtained by low-dimensional Kirkendall diffusion mostly present nanotubular or nanorods morphologies as demonstrated on Figure-1.8. In difference from the redox mechanism, bismuth precursor needs to reduced from usual Bi^{3+} state to Bi^0 state, because Kirkendall diffusion takes place between zero charged species. In the reaction dispersion each Te particle is surrounded by Bi-species (with assistance of surfactant) and upon reaching the reaction conditions as high temperature or pressure, Bi and Te diffuse towards each other and usually forms hollow nanostructures. Certain cases of such diffusion resulted in rods were also reported. The purification step proceeds exactly as in the redox reaction mechanism.

Solvothermal synthesis method is used to produce nanoparticles at high pressure and high temperatures above the boiling point of the solvent. When the solvent is water, the method is distinguished as hydrothermal synthesis. This distinction could be explain by high number of reports published in hydrothermal synthesis in comparison with cases when other solvents than water are used (9 times higher)[84]. Reaction takes place in a sealed autoclave container which can vary in size as desired. High temperature and pressure facilitate the solubility of reactive species, while change of solvent properties (such as decrease of dielectric moment at high temperature) changes the equilibrium of the reaction towards precipitation of Bi_2Te_3. Aqueous reflux synthesis, both for nanoparticles in general and for nanosized Bi_2Te_3 is considered as green, cheap and easily scalable production method. As the name states, reaction takes place in water under reflux conditions. The drawback of this method is relatively long reaction duration

required to obtained desired morphology and composition[85]. In polyol synthesis nanoparticles are formed from the suspension of precursors in high-boiling polyols such as glycols[86]. The most common polyols used in the synthesis of Bi_2Te_3 nanoparticles are ethylene glycol and triethylene glycol. The main advantages of polyol synthesis is multifunctionality of the solvent as it can act as reductant and surfactant along with being a solvent[87]. Nevertheless, additional reducing agents and surfactants can be introduced to the reaction medium.

Table-1.1. Bi_2Te_3 morphologies obtained by wet chemical methods

Method	**Reported morphology**
Hydrothermal	Nanorods[88–90], hexagonal plates[91,92], nano-flowers[89,92], nanotubes[93,94]
Solvothermal	Nanowires[95], nanotubes[82], hexagonal plates[96,97], nanoflowers[98]
Polyol	Nanowires[99,100], nanotubes[101], nanosheets[102]
Aqueous reflux	1D particles[80], Nanowires[103]

Table-1.1 summarises different morphologies of Bi_2Te_3 nanoparticles obtained using wet chemical synthesis.

Thoroughly review every publication of Bi_2Te_3 nanoparticles synthesis is difficult, as when it comes to targeting to specific morphology, the field expands from only TMs to general nanomaterials science. However, to provide understanding to the process, one specific example of Bi_2Te_3 nanoparticles synthesis for each wet chemical method are discussed below.

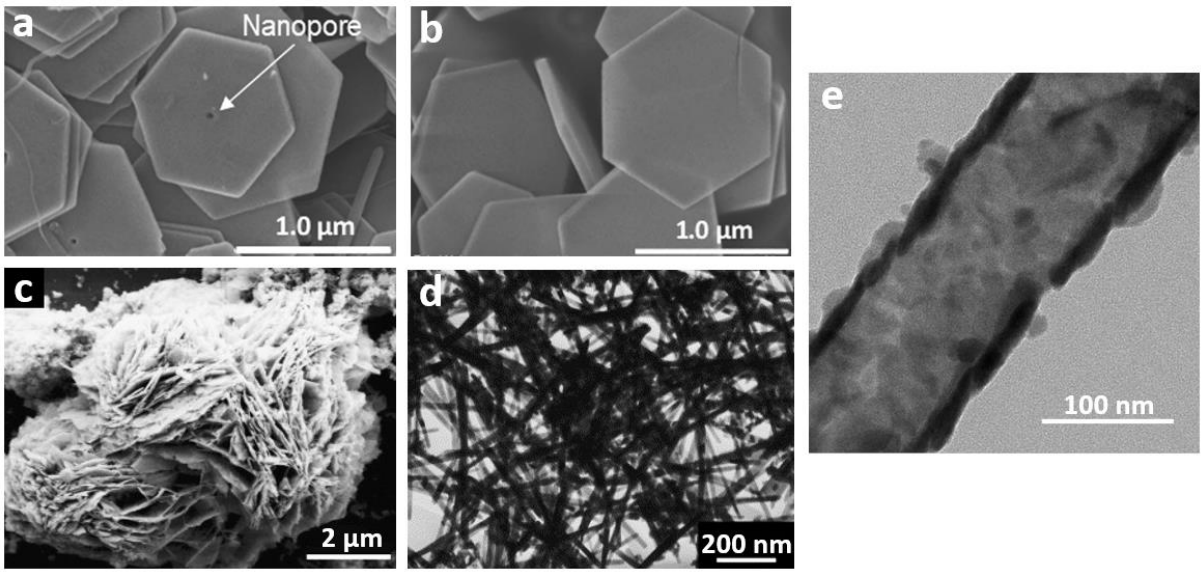

Figure-1.9. Microscopy images of Different Bi_2Te_3 nanoparticle morphologies obtained by wet chemical reaction methods: a and b – hexagonal nanoplates with (a) and without (b) pore by solvothermal synthesis[54]; c – nanoflowers by hydrothermal synthesis[89]; d – nanowires by aqueous reflux synthesis[103]; e – nanotubes by polyol method[104]

Hosokawa et al. reported synthesis of Bi_2Te_3 hexagonal nanoplates by solvothermal method.[54] In a general procedure PVP (0.4g), Bi_2O_3 (0.02M), TeO_2 (0.07M) and NaOH (2 ml of 5M solution) were placed in EG (18ml) and homogenised by mixing. Resulting reaction solution was sealed in an autoclave and heated to the reaction temperature for 4 h while being vigorously stirred. Resulting powder was washed several times and recovered by centrifugation. 4 reaction temperature were selected: 180°C, 190°C, 200°C and 230°C and resulting nanoparticles were compared. As SEM (Figure-1.9a) and TEM images showed, proceeding the reaction at lower temperatures as 180°C and 190°C resulted in hexagonal nanoplates with the edge length of 1µm and nanopore in the middle of the plates. Reaction carried out at 200°C and 230°C resulted in in hexagonal plates with the same dimensions, but without pore (Figure-1.9b). This difference explained by authors as a result of different agglomeration of nuclei at the beginning stages of plates formation.

Synthesis of flower-like nanoparticles is chosen as an example of hydrothermal methods. Zhao and Wang carried out hydrothermal synthesis of Bi_2Te_3 nanoparticles with different surfactants and using PVP resulted in flower like morphology of particles.[89] In a general procedure Te (3.75mmol), PVP (0.5 g), NaOH (2 g) and $NaBH_4$ were dissolved in distilled water (140 ml) and transferred into autoclave. Autoclave was sealed and Te allowed to reduce at 100°C for 4h. Then $BiCl_3$ (2.5mmol) was added to the reaction mixture and reaction

proceeded at 100°C for 36h in a sealed autoclave. Obtained powder was washed and then collected centrifugation. According to SEM images (Figure-1.9c), obtained Bi_2Te_3 powders had flower-like morphology where each flower is made by assembling and intergrowth of big, but thin (20-30 nm) nanoflakes. Proceeding the reaction at higher temperature (200°C) and shorter duration resulted in flowers assembled from much smaller nanoflakes.

One of the early examples of synthesis of Bi_2Te_3 by aqueous solution process at low temperature was reported by Sun et al[103]. They synthesised Bi_2Te_3 nanoparticles using different precursors and comparing synthesis with and without surfactant. The following reaction conditions resulted in Bi_2Te_3 nanowires. Te (7.5mmol), $BiCl_3$ (5 mmol), NaOH (2 g), surfactant SDBS (0.5 g) and $NaBH_4$ (1g) were placed in 200 ml of distilled water and refluxed for 48 h at 65°C. Obtained powder was washed and recovered by filtration. SEM images of the powder (Figure-1.9d) shows that Bi_2Te_3 particles has nanowire morphology with diameter mainly 15-20 nm and 1 μm length. Using other Te precursors or synthesis without surfactant resulted in less regular morphologies.

Another interesting example of Bi_2Te_3 morphology is nanotubes. Kim et al.[104] They obtained highly crystalline Bi_2Te_3 nanotubes by polyol method. First Te nanowires were obtained by reduction and re-crystallization of TeO_2 in EG by $N_2H_4*H_2O$. Then Bi precursor was added into the dispersion and Bi_2Te_3 nanotubes formed at elevated temperatures (usually 160°C) by nanoscale Kirkendall diffusion process. According to SEM and TEM images (Figure-1.9e) of obtained powder, the Bi_2Te_3 nanotubes had diameter of 100-200 nm and 10-15 nm wall thickness. This process was first reported by Zhang et al.[81] but successfully repeated by several papers[101], which designated for different applications of the Bi_2Te_3.

As a conclusion, the morphologies of Bi_2Te_3 nanoparticles obtained by wet synthesis are very diverse, and depending on the reaction conditions can follow different chemical mechanisms. Beyond their primary interest for inorganic thermoelectric materials processing, these nanoparticles recently have found applications for the development of hybrid or composite materials due to the interest in developing alternative easily processable thermoelectric materials for room temperature large scale applications.

I.4 Organic and composite TMs

Current climate change crisis and geopolitical situation resulting in fossil fuel supply crisis makes recovery of waste heat to produce energy critically important. Nearly 50% of waste heat is generated at temperatures below 150°C[105] which requires low temperature TMs. Among the state-of-the-art inorganic TMs only Bi_2Te_3 and its derivatives show reasonable efficiency (ZT around 1) at low temperature for actual application, but high production cost and non-flexibility restrict their mass application. Considering above said and advances made in the last decades in conducting organic materials, interest raised in the last years in developing organic thermoelectric materials (OTM) due to combination of properties such as natural abundance, low cost, non-toxicity, light-weight, flexibility, scalable and non-expensive large surface production[106–108]. These properties of OTMs in combination with their operating range which is below 200°C, make them good candidates for near room temperature mass application. Nevertheless, ZT of organic materials is often several magnitudes lower than their inorganic counters due to their intrinsic low electrical conductivities. The main methods to improve the ZT of OTMs and related challenges will be discussed in this chapter.

I.4.1 Organic Thermoelectrical materials

TE performance of OTM is characterized by its ZT (equation (6)) as for inorganic TMs. However, in contrast, OTMs have intrinsically low thermal conductivities, therefore enhancement of their ZT is mainly focused on improving its power factor (PF).[106] The most apparent method to improve the PF of OTMs is to increase the electrical conductivity by increasing the carrier concentration via doping.[106–109] Most of the OTMs have low electrical conductivities and attempts to increase it by heavily doping usually leads to lowing of Seebeck coefficient, as increase of carrier concentration adversely affect the Seebeck coefficient. Conduction and doping mechanisms of organic materials differ from the traditional inorganic semiconducting materials. Here, conduction mechanism of organics TMs is explained in the perspective of conjugated polymers because they are the most studied class of organic materials and have established transport mechanisms, then a few examples will be described.

I.4.1.a Conduction mechanisms in organic thermoelectric materials

The vast majority of Organic thermoelectric materials (OTMs) are based on the use of conjugated polymers. In conjugated polymers the delocalization of electrons caused by

conjugation of double bonds (π-orbitals) between carbon atoms extends across the polymer chains. However, in pristine conjugated polymers all the orbitals involved in conjugation are occupied and electrons mobility is low. This results in a low electrical conductivity (10^{-3}-10^{-8} S/cm) which does not suit for practical applications.

Doping of OTMs is carried out by introduction of strong electron donors (for n-type) or acceptor (for p-type) by chemical or electrochemical treatment of the polymer. For p-type doping, dopant accept an electron from polymer double bond and a polaron is formed. The charge carried by the polymer (hole in this case) can be displaced under the application of an electrical field making the doped conjugated polymer conductive (Figure-1.10). Conductivity values as high as 10^4 S/cm were reported after doping for OTMs[107]. Conversely n-type dopant are strong donors which introduce additional electrons on the polymer.

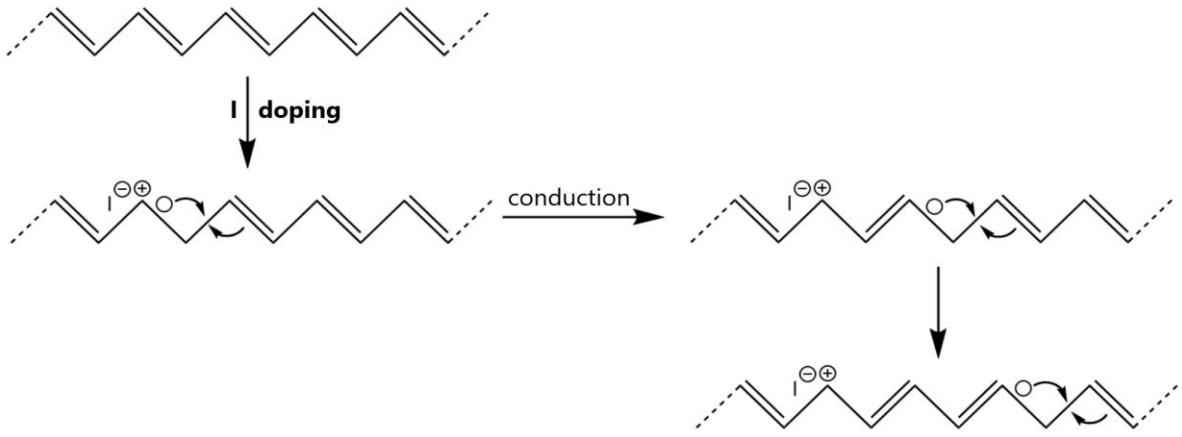

Figure-1.10. p-type I-doping of trans-polyacetylene and electron conduction in doped trans-polyacetylene

As a result, higher doping levels lead to higher electrical conductivities and record conductivities were recorded for heavily doped polymers.[108] Inverse effect of high carrier mobilities caused by increase of carrier concentration on Seebeck coefficient remains in organics systems as for inorganic systems. However, understanding the correlation between Seebeck coefficient and carrier concentration is more complicated in organics due to the weakly ordered morphology of the last. Although the introduction of dopant introduces additional charge carrier, it also introduces additional disorder which might reduce carrier mobility. The extent of this newly introduced disorder depends on the dopant morphology and size, thus its influence on Seebeck coefficient and PF is complex. Nevertheless, a compromise should be reached between positive effect on electrical conductivity and negative effect on Seebeck coefficient while selecting the doping level and type.

Organic (semi-)conductors have low order in contrast with crystalline inorganic ones. Existing ordered domains have relatively low extent. Thus, charge carriers might scatter while passing from one ordered domain to another, which decreases the electrical conductivity of the material. The higher the order the higher the charge carrier mobility and electrical conductivity. Thus, the morphology of polymers has an impact on its PF.[108] One method to enhance the TE properties of OTMs is mechanical stretching which increases the order in the polymers by aligning the polymer chains[109]. Number of examples demonstrated that stretching indeed improves the ZT of polymer TMs, as doped PANI[110] and 2,5-dialkoxy-substitutedphenylenevinylene[111]. Enhancement of electrical conductivity by stretching dominates its adverse effect on Seebeck coefficient, thus overall ZT increases upon increasing the order. Another interesting consequence of stretching is that it increases the anisotropy of properties in the material and power factor considerably increases along the stretching direction in comparison with other directions. There are other methods to improve the ZT of OTMs as solvent annealing, or designing new molecular structures.

The main classes of OTMs are briefly presented in the next paragraphs.

I.4.1.b Thermoelectric properties of organic materials

Conjugated polymers are the main organic materials considered for semiconductor application, including TEs.[112] The first conjugated polymer studied for TEs was trans-polyacetylene doped with iodine and oriented by stretching which demonstrated electrical conductivity of 10 000 S/cm at 28% of doping.[113] Nevertheless, due to oxidative instability, it did not find broad application.

The most studied of all conjugated polymer is PEDOT:PSS. Originally being designed as antistatic polishing finish, PEDOT itself is highly conducting (300 S/cm) and very stable at oxidized states, but rigid and insoluble, which makes it difficult to process.[114] The latter problem was solved by using the poly(styrene sulfonic acid) as charge balancing dopant (in the step of polymerization). This approach resulted in a water soluble PEDOT:PSS polyelectrolyte system which is easy to process, has relatively high conductivity and stability. In this system positively charged PEDOT chains is linked to the negatively charges PSS chains by Columbic attraction. As a result of PSS doping, the TE properties of PEDOT:PSS system drops significantly in comparison with pristine PEDOT.[115] Therefore, number of approaches were tried to improve the power factor of the system. Except aforementioned general methods of improving the power factor of conjugated polymers, methods such as secondary doping and

dedoping were also applied, being effective at certain conditions. Furthermore, control of the PEDOT morphology and molecular weight found to have certain influence on TE properties of the polymer. Record high electrical conductivity of 4600 S/cm was reported for the PEDOT:PSS aligned by shearing during the film deposition.[116] Highest ZT value was reported to be 0.42 at electrical conductivity of around 900 S/cm for DMSO annealed PEDOT:PSS films.[117]

Other famous conjugated polymers are doped polypyroles, polyanilines and polythiophenes. All these well studied TE conjugated polymers are p-type semiconductors. This is because n-type π -conjugated polymer generally have low ionization energy, therefore these polymers have high oxidation rate which results in instability in application conditions like humidity.[118] Therefore, the progress in n-type OTMs lags behind the p-type OTMs.

A few developments have also been achieved with Metal-Organic coordination polymers. These consist in the association of a metal ion and organic ligand where the last also carries the role of linker. They gained interest in TEs since Zhu et al demonstrated high TE characteristics in the range of poly(metal-1,1,2,2-ethenetetrathiolate)s.[118] Particularly, poly(Ni-1,1,2,2-ethenetetrathiolate) showed Seebeck coefficient of -122 μV/K which resulted in ZT of 0.2.[119] This was first the first n-type stable OTM with high performance. Recently conducting metal organic frameworks as well gained the interest as organic semiconductor including TE field[112].

Despite the achievements highlighted above in improving the thermoelectrical properties of OTMs, they still remain to be relatively difficult to process and expensive to produce. Additionally, n-type OTMs are highly unstable for environmental conditions. These reasons hinder the application of OTMs and leads the research of optimal thermoelectrical material towards alternatives as hybrid inorganic/organic composites.

I.4.1.c Hybrid thermoelectric materials

Preparation of hybrid organic-inorganic composite TMs can be considered as another method of improving the TE characteristic of organic TMs[105,120,121]. In an ideal scenario, a hybrid composite should possess positive features of OTMs such as processability, flexibility and low thermal conductivity in combination with high power factor of inorganic TMs. It is also facile method to prepare air stable organic based flexible TMs with n-type conductivity.[118]

Additionally, several hybrids combinations were reported to nearly decouple the advert correlation between electrical conductivity and Seebeck coefficient.[122]

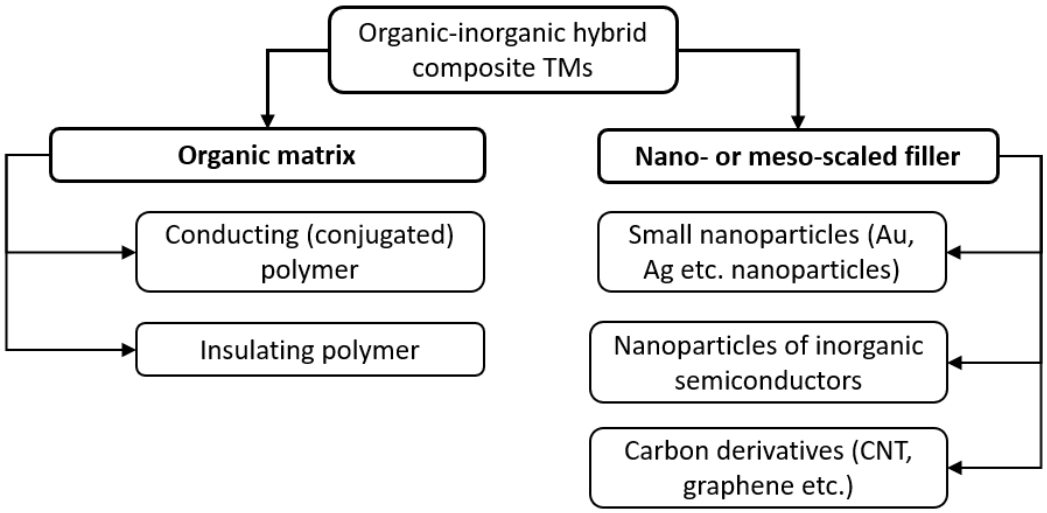

Figure-1.11. Common composition of hybrid organic-inorganic composite TMs

Usual combinations of matrix and fillers of hybrids for TM are shown on Figure-1.12.[105] In a conventional case, in order to benefit from the processability and flexibility, polymers are chosen as a matrix. Depending on the arrangement of the filler the matrix can be either conducting or isolating. In the case of the last, the filler must form percolated network[123] in the matrix to provide electrical conductivity to the composite, thus the minimum amount of the filler should be equal or higher than the percolation threshold. The advantages of isolating polymers over conjugated ones is low cost, even easier processability and better stability of the structure. However, such hybrids usually show very low electrical conductivity and consequently several order of magnitude lower PF and ZT. While when using conducting matrix, the filler is not required to percolate, thus depending on the optimized feature (σ, α or κ) amount and arrangement of the filler can be varied. Small organic molecules and metal organic coordination polymers are not well studied themselves as OTMs, thus their application in hybrids is even smaller.

Fillers used in hybrid composite can be divided into three main categories[120] : metal nanoparticles, carbon derivatives or inorganic thermoelectric nanoparticles. Since transport mechanisms of charge carriers, phonons and other species is not firmly established for OTMs itself, thus discussion TE properties of hybrid composites is even more difficult. Thus, most of the achievements in the field are obtained by empirical research. Due to the wide variety of both matrices and fillers, complicated by strong effect of processing conditions the comparison

of the obtained results can be difficult. In addition to the dissimilar transport mechanisms in organic matrices and inorganic fillers, different behaviours of the species at the interface should be considered. The interface between the matrix and filler is often considered as a filter for traversing species formed due mismatch of the energy levels. The possibility to decouple the relation between electrical conductivity and Seebeck coefficient is not apparent for all the systems, and many hybrids where the correlation between those properties remains were reported. Below, certain examples of hybrid TMs are discussed with the aim to show versatility of correlation of properties from system to system.

I.4.1.c.1 Composites with metallic nanoparticles

First category is metal nanoparticles – classical filler for composites. They are usually added in a small amount in order to increase the electrical conductivity of the conjugated polymers. Classical examples are Au, Pt nanoparticles[124]. Also, metal nanoparticles can be added as the second filler when additional enhancement of electrical conductivity is required. To obtain maximum improvement of composite properties from inclusion of metal nanoparticles, the last have to be homogenously distributed within the polymer matrix. Metal nanoparticles usually have small size of several dozen nanometres and tendent to agglomerate in the absence of stabilizing surfactant. Therefore, to incorporate the metal nanoparticles into a polymer matrix surfactant is applied alongside. However, the surfactant usually acts as insulator and decreases the electrical transport properties of the composite. Thus, balance should be made between insulating effect of the surfactant and adverse effect of nanoparticles agglomeration in the absence of the surfactant. For example, in the work of Toshima et al.[124] inclusion of 0.2 wt% Au nanoparticles into PANI increased the electrical conductivity from 150 S/cm to 300 S/cm. Further increase of nanoparticles ratio did not improve the properties of the composite due to the agglomeration of Au particles. While addition of PVP stabilized Au particles inversely led to decrease of the electrical conductivity of the hybrid to 50 S/cm. Here, PVP, in spite of providing excellent dispersion of the Au particles in the matrix, acted as insulator. Lately metal nanoparticles are mainly used in small amount and only to increase the electrical conductivity.

I.4.1.c.2 Composites with carbon derivatives

The most studied fillers for thermoelectric composites processing are low dimensional carbon derivatives such as carbon nanotubes (CNT) and graphene. Low dimensional carbon allotropes as CNT, graphene, carbon black are extensively used in material science for various purposes from increasing the mechanistical strength of the material to tuning the specific properties as catalytic selectivity or electric conductivity. Under certain combination and processing condition, very interesting TE performances such as a ZT as high as 0.5 can be obtained[125], which is very appealing considering abundance, relatively low cost and low TE properties of carbon derivatives alone.

In TE field, CNTs are the most used carbon derivatives, including the preparation of carbon/polymer composite TMs[123]. In contrast with the state-of-the-art semiconductor fillers, CNTs source is abundant. Additionally, because of their transport properties lying between metallic and semiconductor behaviours, CNTs themselves are relatively poor thermoelectric materials due to low Seebeck coefficient and high thermal conductivity. However, upon preparation of composites with conducting polymers, PF and ZT higher than that of individual components are reported. In most of such examples, improvement is achieved thanks to decoupling of the electrical conductivity and Seebeck coefficient relation and only slight increase of thermal conductivity of the polymer.

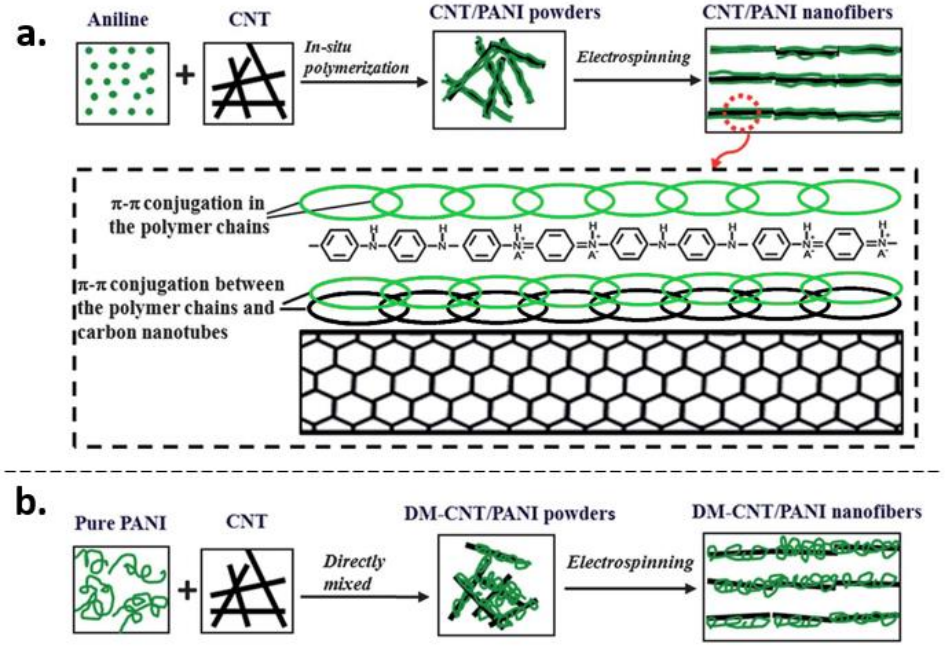

Figure-1.12. CNT/PANI hybrid composites with different conformational arrangement of PANI chains, prepared by a – in-situ polymerisation; b – ex-situ mixing[126]

One of the most interesting hybrid composite TMs of CNT is in situ polymerized SWCNT-PANI composites. During the synthesis, PANI polymerizes along the surface of the SWCNT because of strong π-π interactions between CNT and PANI, resulting in elongated conformation of PANI (Figure-1.12a) in contrast with coiled conformation which would be formed in the absence of directing SWCNT[127–129]. Elongated (expanded) conformation of the PANI results in increased carrier mobility which leads to enhancement of electrical conductivity and Seebeck coefficient of the polymer. π-π interactions between SWCNT and PANI results in further ordering of the PANI chains and an efficient wrapping of each tube by polymer. Homogenous wrapping decreases the overall interfacial barrier which is usually caused by energy level mismatch between polymer and filler, thus increasing the carrier mobility at the interface. The first composite of this kind was reported by Yao et al. where maximum PF of 20 μV/ m*K^2 and ZT of 0.004 were obtained.[128] Later number of papers reported similar hybrid composites with enhanced properties which were achieved by adjusting the film preparation methods, which allowed further ordering of the PANI chains. PF and ZT equal to 176 μV/ m*K^2 and 0.12 were reported for CSA-doped-PANI/SWCNT hybrid composite films prepared by casting[129].

Another category of the CNT filled hybrid composites are those where the matrix is an insulating polymer as PVA, PC, PP, PU, PS and others. For the composite to be TE active the only electrically conductive component – CNT filler must form segregated network. Dispersion of CNT in the matrix governs the performance of such composites, while the morphology itself is governed by miscibility of the filler with matrix[123]. For examples Yu *et al.* prepared samples of SWCNT/PVA composites where SWCNT was stabilized by varying amount of arabic gum[130]. With increase of the of the stabilizer ratio conductivity of the sample increased up to 900 S/m, while Seebeck coefficient and thermal conductivity remained in a constant range. With an increase of the stabilizer ratio it is assumed that the dispersion of CNT improves, forming more homogeneous arrangement of the filler, thus increasing the electrical conductivity. Constant values of Seebeck coefficients and thermal conductivities upon increase of stabilizer ratio demonstrates that this type of composite one of the ones where decoupling between Seebeck coefficient, electrical conductivity and thermal conductivity could be reached. Choi et al compared the effect of CNT type on CNT/Nafion hybrid composites.[131] The results showed that while electrical conductivity is varied by the type of CNT (MWCNT, FWCNT and SWCNT), the Seebeck coefficient of the composite remained nearly constant.

I.4.1.c.3 Composites with inorganic semiconductor fillers

Interest in using inorganic thermoelectric nanoparticles as fillers raised since the boost in the research on the synthesis of nanosized semiconductors. Although their addition enhances the TE performance of the organic matrix, the overall PF and ZT are usually much lower than for pure sintered filler. However, sintering the pure semiconductor nanoparticles is generally energy consuming, thus expensive. Therefore, when easily processable hybrid composites show relatively high ZT, a trade-off between cost and efficiency can be met. One of the interesting representatives of this category filler is Bi_2Te_3 and its derivatives because their optimal operating temperature is close the operating temperatures of the organic matrix.[132]

Du et al. compared the effect of fabrication method on the TE properties of $Bi_{0.5}Sb_{1.5}Te_3$/PEDOT:PSS composite[133]. In a general procedure, fine suspension/solution of hexagonal $Bi_{0.5}Sb_{1.5}Te_3$ sheets and (DMSO)/PEDOT:PSS in EtOH with varying content of the filler. Then hybrid TM films were prepared on a glass substrate by two methods: drop casting and spin coating. Both type of films had rough surface and certain agglomeration, but their TE characteristic were rather interesting. Both electrical conductivity (from 750 S/cm up to 1300 S/cm) and Seebeck coefficient (from 10 μV/K up to 17 μV/K) increased with the increase of the filler content for drop casted films (Figure-1.13a). While spin coated films demonstrated dramatic decrease of electrical conductivity (from 700 S/cm to 110 S/cm) and increase of Seebeck coefficient (from 10 μV/K up to 48 μV/K) with an increase of the filler amount. Overall, both type of films demonstrated increase of PF with an increase of the filler content (Figure-1.13b). The spin coated hybrid films represent the classical inverse correlation between σ and α, while drop casted films demonstrates rare cases where both σ and σ were enhanced simultaneously. It can be attributed to the different alignment of the filler particles governed by processing method, thus as an effect of the composite morphology.

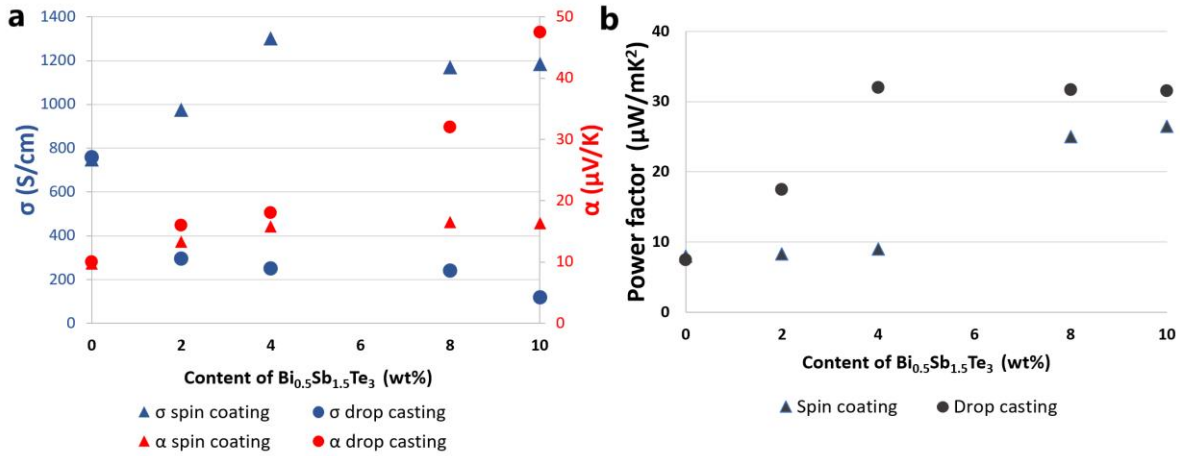

Figure-1.13. Electrical conductivity, Seebeck coefficient and PF of $Bi_{0.5}Sb_{1.5}Te_3$/PEDOT:PSS hybrid composite films prepared by spin coating versus drop casting[133]

Regarding the composites with an insulating polymer matrix, but with an end application which requires electrical conductivity, the most important feature is percolation of the conducting filler[134] therefore it was closely studied.. Namely the effect of amount, size and shape on percolation threshold was investigated. The main collusion is that the percolation threshold is reached for lower filler amounts when filler particles size decreases or particles aspect ratio increases. Moreover, the percolation threshold also depends on the quality of the filler dispersion in the matrix which is mainly affected by preparation mechanism. Yet, after the reaching the percolation threshold, the overall properties of the material will depend on many parameters such as the respective properties of the matrix, the filler and the interface, the filler amount and its aggregation level.

Up to date only few papers reported Bi_2Te_3/insulating polymer composites for TE application. This can be related to the fact that Bi_2Te_3 is relatively expensive compound. Obtaining small sized Bi_2Te_3 particles by top down methods usually accompanied with oxidation of particles surface which deteriorate the TE properties. Also, the size of particles remains relatively large and aspect ratio low, which would require high amount of the filler for reaching the percolation. Synthesis of Bi_2Te_3 filler particles by bottom up methods are usually small scaled and time consuming.

One of the first such works was reported by Madan et al where they prepare Bi_2Te_3/epoxy resin composite by dispenser printing method.[135] Bi_2Te_3 nanoparticles with average size of 10 μm were obtained by ball milling the commercial powder. The printing slurry was prepared by mixing the components of epoxy resin – DGEBA resin and

methylhexahydrophtalic anhydride hardener along with catalyst, Bi_2Te_3 particles and solvent for adjustment of the viscosity in a vortex mixer. The slurry was then dispenser printed on glass substrate with the thickness of 100-200 μm and printed composite was cured at different temperatures and for different duration of time. The loading of the filler was 80 wt%. TE properties of the films varied depending on both, curing temperature and time. When cured for 12 h, electrical conductivity of the composite slightly decreased with an increase of the curing temperature from 24 S/cm at 200°C to 17 S/cm at 350°C. On the contrary Seebeck coefficient significantly increased from -168 μV/K to -275 μV/K. Yet it had net positive effect as PF increased from $6.8*10^{-5}$ W/m*K^2 to $1.28*10^{-4}$ W/m*K^2. Authors suggest that at elevated temperature the particles sinter and aggregate, which decreases the electrical conductivity but do not comment on the more important effect on the Seebeck coefficient.

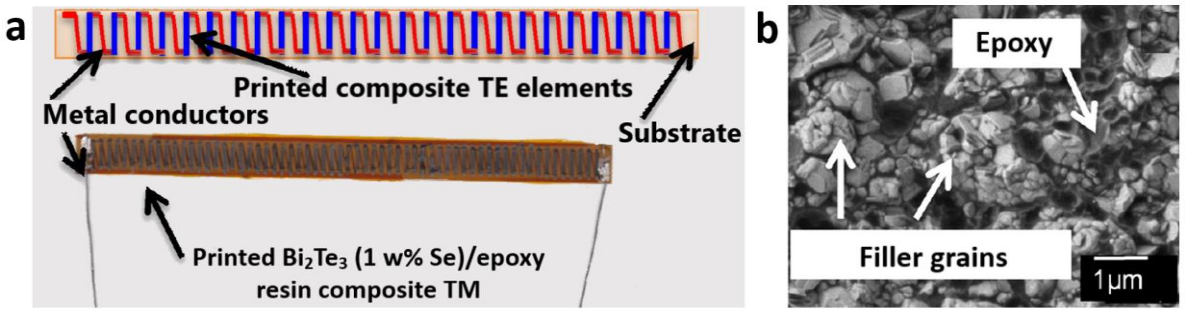

Figure-1.14. Dispenser printed Bi_2Te_3 (1w% Se)/epoxy resin composite TM : a – schematic and image of printed device, b – SEM image[136]

The same authors later reported improvement of electrical conductivity of the composite which lead to improvement of the power factor by changing the Bi_2Te_3 preparation method and doping (the filler).[136] The filler particles were prepared by ball milling, but by bottom-up method from elemental components Bi and Te with Se dopant. The composites were prepared following the similar procedure as in previous report by dispenser printing and the effect of the dopant concentration in the filler on the TE properties of the composite were evaluated. Both electrical conductivity and Seebeck coefficient varied with the dopant concentration, which suggest, that those characteristics in composites highly depend on the fillers intrinsic properties. In the optimally doped composites, the effect of curing temperature was completely different in comparison with the previous report. Thus a much better electrical conductivity of 100 S/cm and a slightly lower Seebeck coefficient of -175 μV/K were obtained at higher curing temperature in contrast with 25 S/cm and -182 μV/K at lower temperature. PF was once again were better for the samples cured at higher temperature, this time due to the increase of electrical conductivity. No solid explanation was given for such change of the behaviour with changing

the curing temperature. Additionally, due to inconsistencies of the calculations, the ZT values in these reports should not be considered for comparison. Authors of the above discussed papers also published several similar papers where different derivatives of Bi_2Te_3 was used as filler.[137,138]

Cao et al. also reported $Bi_{1.8}Te_{3.2}$/epoxy resin composite prepared by screen printing methods. Filler particles had relatively high particles size as it was used as received[139]. Printing slurry was prepared by mixing the filler with resin components and along with solvent triple roll mill, then was screen printed on a Kapton substrate through polyester screen. Deposited film was cured at 250°c for 3h. Then electrical conductivity and Seebeck coefficient of the films were evaluated over time. While conductivity of the samples slightly decreased gradually over time from 4 S/cm to 2.8 S/cm after 100 days, the Seebeck coefficient remained relatively unchanged around -125 μV/K.

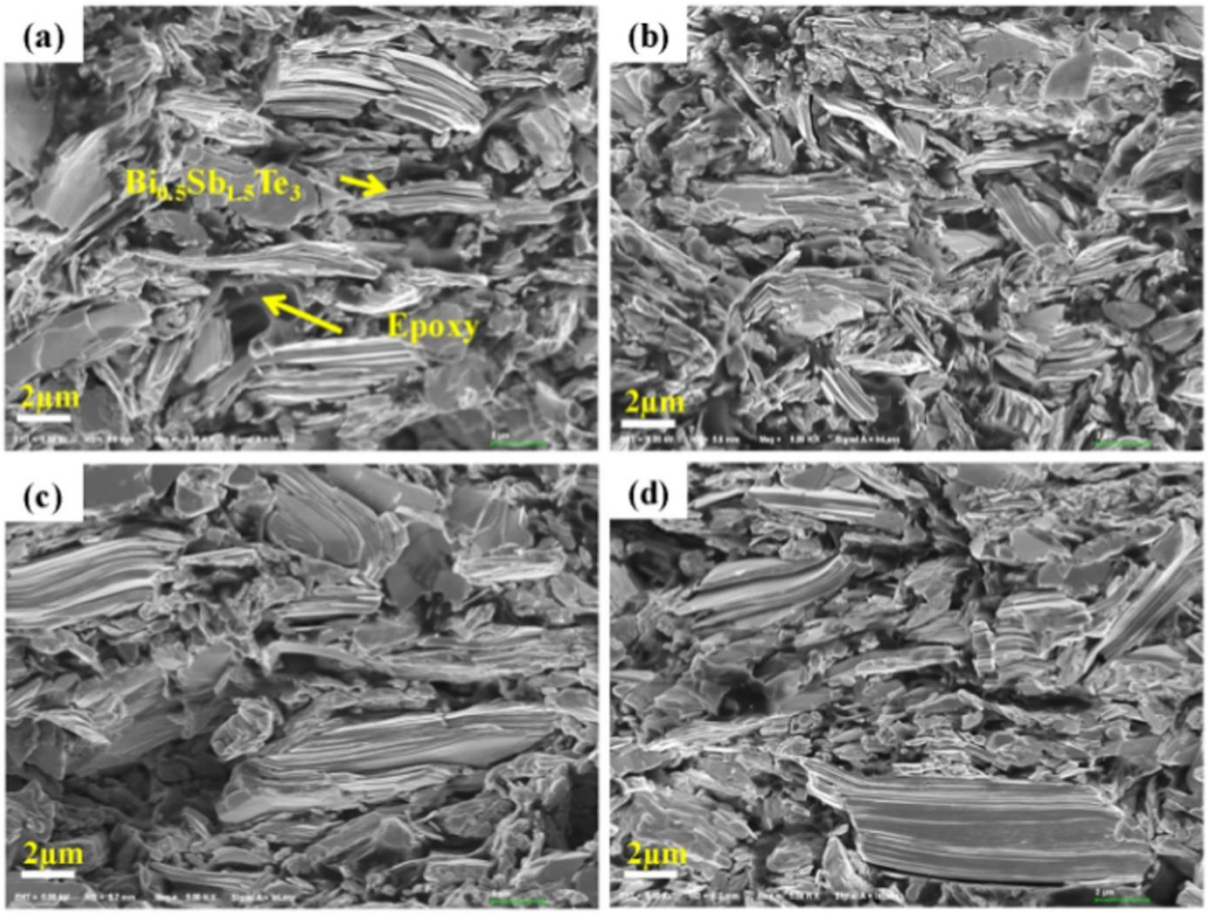

Figure-1.15. SEM images of $Bi_{0.5}Sb_{1.5}Te_3$/epoxy resin composite films cross-sections prepared by brush printing and subsequent hot pressing at temperature a – 200°C; b – 250°C; c – 300°C; d – 350°C[140]

More recently Hou et al. prepared $Bi_{0.5}Sb_{1.5}Te_3$/epoxy resin composite films for thermoelectric cooling application by brush printing and subsequent hot pressing[140]. They closely evaluated the effect of hot pressing and curing temperature on morphology and TE properties of the composite. Filler particles with the size 1-10 μm were obtained by ball milling the $Bi_{0.5}Sb_{1.5}Te_3$ ingots. Slurry for printing was prepared by mixing the epoxy resin - DGEBA, hardener - methylhexahydrophtalic anhydride, catalyst – 2-ethyl-4methylimiazol and filler by mechanical stirring and ultrasonic dispersion. It was then brush printed on a templated flexible polyimide substrate and cured by hot pressing. Both increase of the curing temperature and pressure results in better preferential orientation of the filler particles and dense packing. From the images from Figure-1.15, which shows $Bi_{0.5}Sb_{1.5}Te_3$/epoxy resin composite films prepared at constant pressure but different curing temperatures, it is clear that the alignment of particles (perpendicular to the pressing direction) is better with increase of the temperature. Higher temperature leads to decrease of the resin viscosity which facilitate re-arrangement of particles in the pressing direction and elimination of bubbles which leads to denser packing. Surface 3D images of the samples showed that surface roughness decreased from 259 nm to 85 nm at highest curing temperature. Increasing the pressure has similar effect as temperature. As can be seen on Figure-1.16a, the filler particles in the sample prepared at 0 MP pressure are randomly oriented while rough surface and presence of bubble holes and cracks can be seen from the surface image. Increasing the pressure leads to better orientation of the particles and better surface (Figure-1.16b and c). Denser packing of the of particles and decrease of the faults such as bubbles and cracks expectedly leads to improvement electrical transport properties as can be seen on Figure-1.17. Highest PF of 0.85 (Table 1.2) was obtained when film was cured at 350°C and 4 MPa. These value so far is the highest reported for PF for Bi_2Te_3 derivative/ epoxy resin hybrid composites.

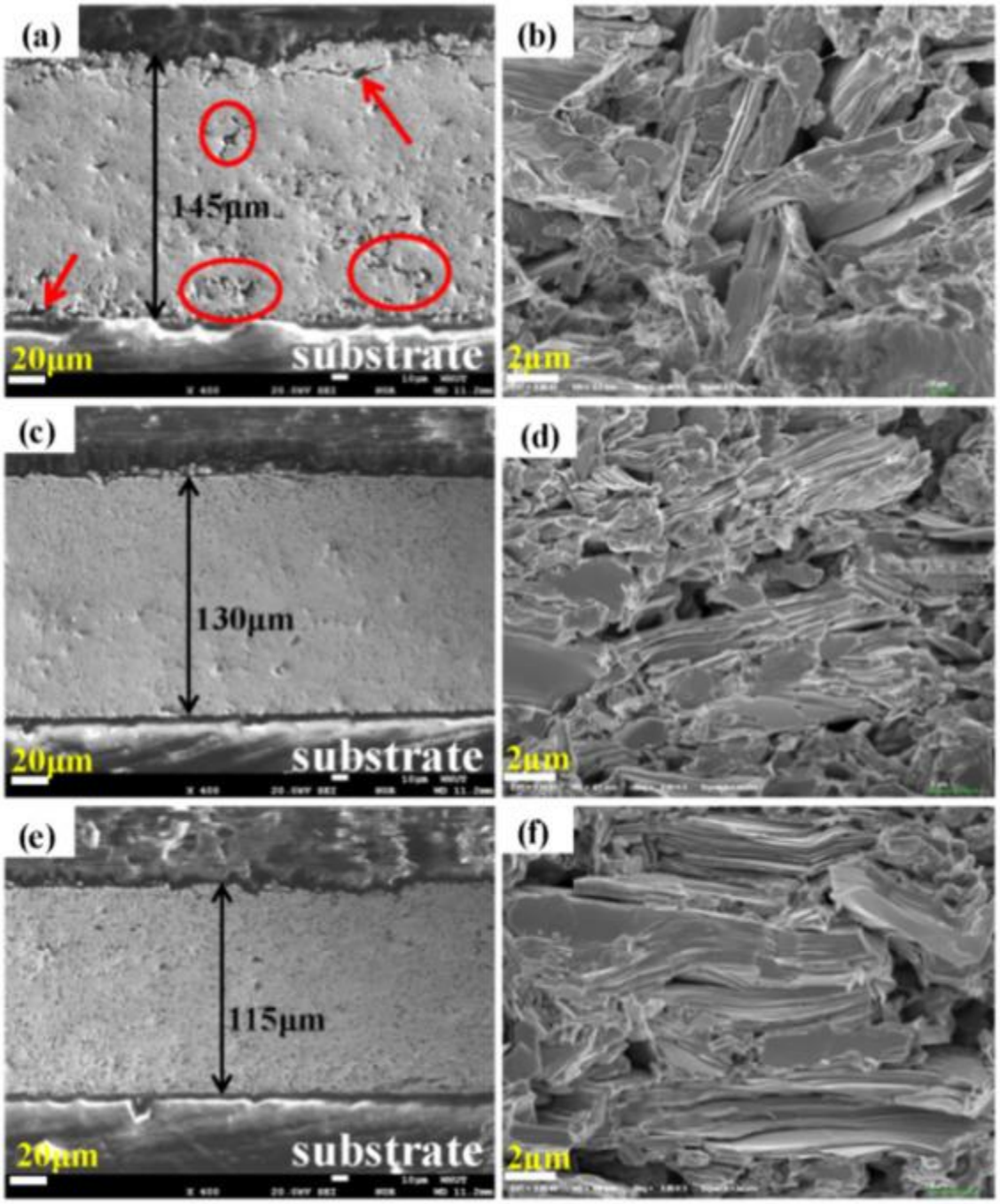

Figure-1.16. SEM images of $Bi_{0.5}Sb_{1.5}Te_3$/epoxy resin composite films cross-sections prepared by brush printing and subsequent hot pressing at pressures: a – 0 MPa; b – 2 MPa; c – 4 MPa[140]

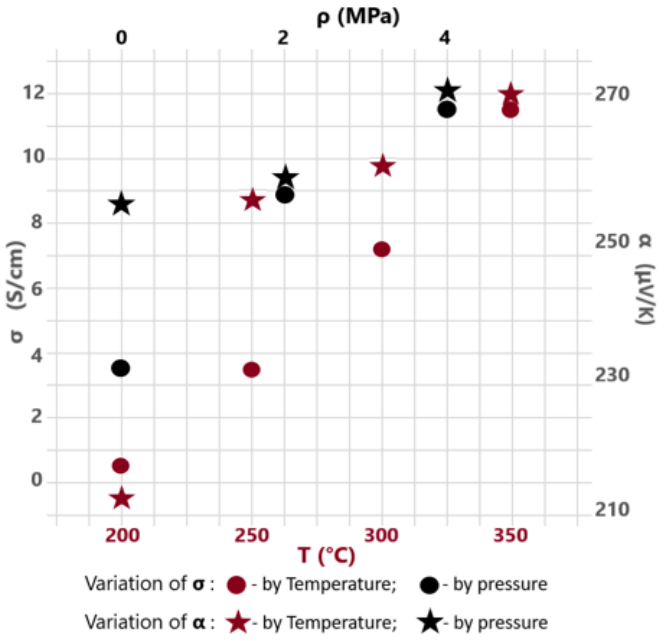

Figure-1.17. σ and α of $Bi_{0.5}Sb_{1.5}Te_3$/epoxy resin composite films obtained at different curing temperature and pressures[140]

Table-1.2 PF $Bi_{0.5}Sb_{1.5}Te_3$/epoxy resin composites[140]

Curing T (°C)	$\alpha^2\sigma$ (mW K^{-2} m^{-1})
200	0,023
250	0,24
300	0,5
350	0,84

Curing ρ (MPa)	$\alpha^2\sigma$ (mW K^{-2} m^{-1})
0	0,24
2	0,58
4	0,84

For the best of our knowledge, above discussed papers are only publications reporting Bi_2Te_3/insulating polymer hybrid TMs where TE properties, at lease electrical conductivity and Seebeck coefficient were reported. Yet, few conclusions for this class of composite (epoxy resin matrix) can be drawn as considerable influence of curing temperature and packing density on transport properties of the TMs.

I Conclusion

This literature review summarized the TE field from concept through history to the state-of-the-art materials. The current motivation of the field to grow further is mass commercial application. Both organic and inorganic materials offer their advantages and disadvantages for commercial application. Organic TMs are more available, cheaper and easy processible, but have low conversion efficiency, while inorganic TMs are exactly the opposite. Preparation of hybrid composites might offer a trade-off solution, but Is still it in their early stages of development.

Inorganic TMs efficiency already reached quite high values, yet most of them are for high temperature application. Physical laws do not prohibit the efficiency of the current TMs to grow further, even predicting ZT as high as 14 for Bi_2Te_3 quantum wells. Thus, research in inorganic TMs should be continued with an emphasis on abundant, non-toxic and low temperature operating TMs development. On the opposite, fully organic TMs field currently lacks the fundamental studies to understand the charge carrier transport

Hybrid composite TMs are quite in an early state of the development and realized by empirical method of randomly trying different systems. Efficiency of hybrid TM is expected to be in between its constituents efficiencies. However, some hybrid TMs with efficiencies even lower that the efficiency of the least efficient component are sometimes reported. One way to improve the efficiency of hybrid materials, might be to work on the synthesis of thermoelectric nanoparticles specifically designed for this kind of application and simultaneously develop processing techniques which would allow to obtain composite materials benefiting from each of his components intrinsic properties.

Chapter II – 1-DDT assisted reflux synthesis of Bi_2Te_3 nanoparticles

II Introduction

The aim the Chapter 2 is to obtain Bi_2Te_3 nanoparticles with tubular morphology according to the main objectives of the thesis. In this chapter various methodologies of 1-DDT assisted reflux synthesis of Bi_2Te_3 nanoparticles which allowed increasing nanotubes content in the product from 30% to 100% are presented. All methodologies follow two distinct mechanisms: rolling up and nanoscale Kirkendall diffusion. While both mechanisms are well reported in the literature, current methods offer alternative easy scalable, mild reaction conditions. Nanoscale Kirkendall effect requires a sacrificial template, therefore, development of the in-situ preparation method of the template is also reported. Synthesized nanoparticles were characterized by SEM, TEM and XRD.

First methodology, 1-DDT assisted reflux synthesis of Bi_2Te_3 nanoparticles via rolling up mechanism is developed based on preliminary results of the research group.[141] The content of the particles with nanotubular morphology in the obtained particles is 30%. Increase of this value is expected to improve the thermoelectrical properties of the final material and also reduce the percolation threshold in composite preparation. In order to increase the nanotubes content, the second synthesis methodology of Bi_2Te_3 nanoparticles via nanoscale Kirkendall diffusion was developed. The methodology is kept similar to the first one in order to keep the advantage of mild reaction conditions and it yields Bi_2Te_3 phase with nanotubes content from 50% up to 100% depending on the template quality. Thermoelectrical properties of the obtained Bi_2Te_3 nanoparticles are discussed in the final sub-chapter.

II.1. 1-DDT assisted reflux synthesis of Bi_2Te_3 nanoparticles via rolling up mechanism

II.1.1 Experimental Protocol

Synthesis was carried out in 2 L reactor equipped with stirrer and condenser. The temperature of the reactor is controlled by fluid flow through the jacket of the reactor. The reaction temperature can be controlled in two modes: jacket temperature and reaction temperature.

Synthesis itself was carried out in three steps as described on scheme 2.1.1. In the first step Te(0) (99.99% purity, 3.47 g, 27.19 mmol, 1 eq.) was reduced by $NaBH_4$ (96% purity, 4.18 g, 106.07 mmol, 3.90 eq.) in 1.3 L of water degassed in advance by sparging with argon. The pH of the solution was 13 and was regulated by addition of NaOH (98% purity, 9.68 g, 237.16 mmol, 8.72 eq.). The temperature of the reaction is set to 100°C and reaction is allowed to reflux for 24 h. Prior addition of the following components, the obtained Te^{2-} solution was cooled down to room temperature. Second step – preparation $Bi(DDT)_3$ complex solution was carried out in parallel to the first step. 1-dodecanethiol (DDT) (98% purity, 72.2 mL, 61.00 g, 295.84 mmol, 10.88 eq.) was mixed with THF (361 mL) degassed by argon purging in advance, then $BiCl_3$ (99.99% purity, 5.75 g, 18.23 mmol, 0.67 eq.) was added to the solution and stirred for 24 h. During the course of stirring, $BiCl_3$ gradually dissolves and solution turns to yellow, indicating the formation $Bi(DDT)_3$ complex. Excess of DDT prevents $BiCl_3$ oxidation. Once both components were ready, solution of $Bi(DDT)_3$ complex is gradually added to the reduced Te solution by cannula without breaking an inert atmosphere. The mixture was refluxed at 70°C under continuous stirring for 72 h. All the reaction steps carried out under argon atmosphere. The obtained black powder is filtered, consecutively washed by THF, ethanol, acetone and water and dried.

II.1.2 Results and discussion

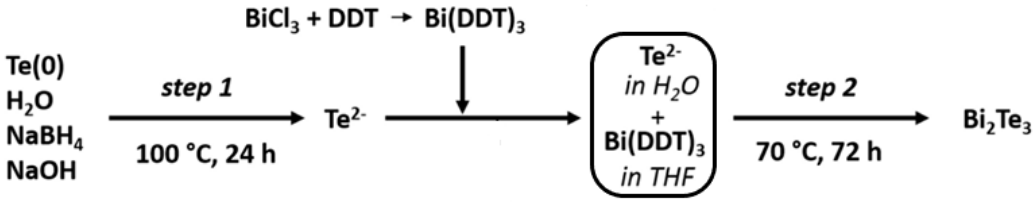

Scheme 2.1.1. Schematic two-steps process for the preparation of the Bi_2Te_3 via rolling-up mechanism

The preparation of Bi_2Te_3 nanoparticles was carried out in 2 L Jacketed stirred reactor vessel with precise temperature control which enables obtaining 7.00 g of pure Bi_2Te_3 for each reaction. The aqueous synthesis depicted on Scheme 2.1.1 was performed in two steps via an ionic reaction process[142] under argon atmosphere preventing oxidation risks. First, the reduction of tellurium into Te^{2-} was performed with $NaBH_4$ in distilled and degassed water at a pH of 13 under heating at 100 °C, during the process, the mixture coloured pale purple. For the second step, $Bi(DDT)_3$ complex was freshly prepared from the reaction with bismuth (III) chloride ($BiCl_3$) and DDT in tetrahydrofuran for 24 h. A large excess of DDT was used to prevent oxidation and favour the anisotropic growth of Bi_2Te_3 particles. The layered structure of $Bi(DDT)_3$ precursor was checked on the collected yellow powder isolated after evaporation of $Bi(DDT)_3$ solution and filtration followed by washings with ethanol. The indexation of the diffraction peaks is in good agreement with literature data[143] (Figure-2.1a). Then, at room temperature, the solution composed of $Bi(DDT)_3$ and an excess of DDT was directly added to the Te^{2-} containing mixture before heating the reaction mixture at 70 °C. Finally, the sample was collected after 72 h. The powder was isolated after filtration, washed successively with water, ethanol, acetone and THF and finally dried at 60 °C for 6 h. Bi_2Te_3 powder was obtained with a yield of 97%.

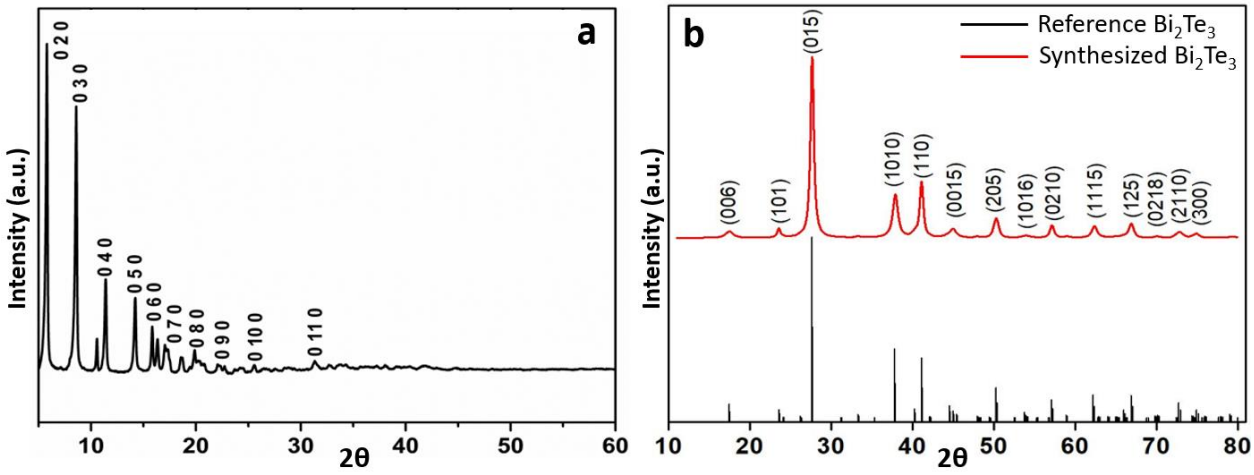

Figure – 2.1.1. X-ray diffraction patterns of: a - $Bi(SC_{12}H_{25})_3$ precursor; b - Synthesized Bi_2Te_3 in comparison with literature data (space group R-3m, COD ID 23108039)

Figure-2.1.1b depicts the XRD patterns of obtained Bi_2Te_3 (red line). The indexation of the diffraction peaks is in agreement with the rhombohedral lattice structure of Bi_2Te_3 (space group R-3m, COD ID 23108039). The broadening of diffraction peaks can be attributed to the nanometric size of the crystallites which has been confirmed by TEM observations. No diffraction peak from unreacted Te (0) or any impurities are observed.

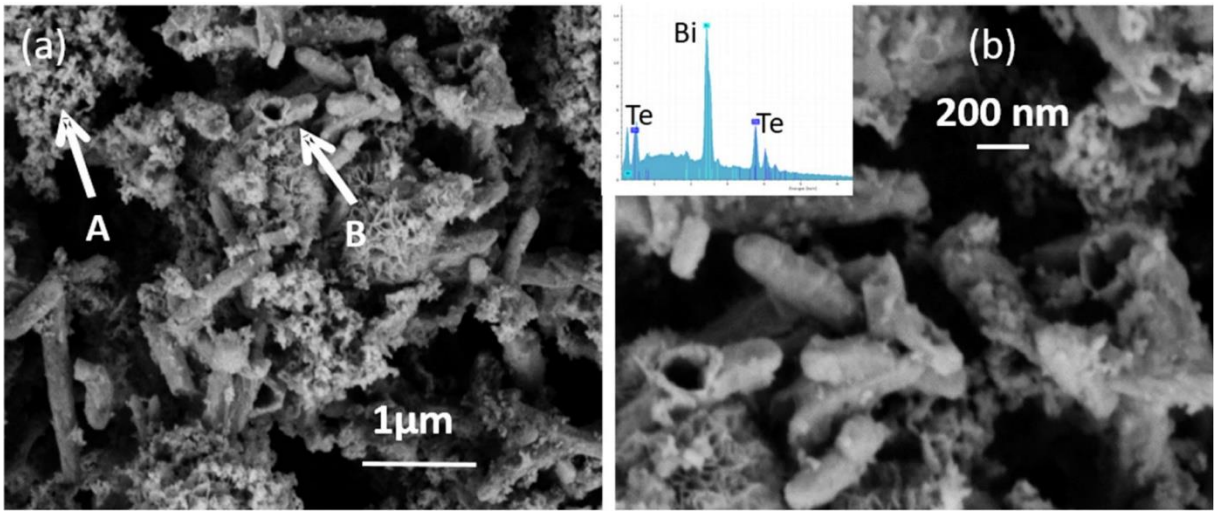

Figure – 2.1.2: a – Typical SEM images of Bi_2Te_3 sample, within inset EDX spectra of the powder (a) blocks of matter are made of two type of Bi_2Te_3 crystals; b – enlargement evidencing small isotropic Bi_2Te_3 nanocrystals aggregated (white arrow A) and open Bi_2Te_3 nanotubes (pointed by white arrow B)

The SEM pictures in Figure-2.1.2 show the typical morphology of the Synthesized Bi_2Te_3. The powder is made of micron size particles (Figure-2.1.2a). As can be seen on the enlarged picture (Figure-2.1.2b) those particles are composed of nanotubes in a proportion of 30% (Figure-2.1.2a, arrow B) packed into a nest-like structure and surrounded by aggregates of isotropic nanoparticles (Figure-2.1.2a, arrow A). The opening of the tubes is clearly evidenced (arrow B), characteristic of the hollow tubes similar to reported studies.[144] The length of the tubes varies from 200 to 500 nm. The EDX spectra recorded on the two types of Bi_2Te_3 particles and depicted in the inset of Figure-2.1.2b indicate that, in each case, the Bi/Te ratios are close to 40/60 in a good agreement the expected formula. In addition, the key role played by DDT in the reactivity and in the formation of the nanotubes has been evidenced by performing the synthesis under the same conditions but without DDT. XRD pattern of the obtained product depicted in comparison with XRD pattern of pure Te on Figure-2.1.3a and EDX of particles on Figure-2.1.3b show that it contains mainly Te(0) rods and a few aggregates of Bi_2Te_3 isotropic particles.

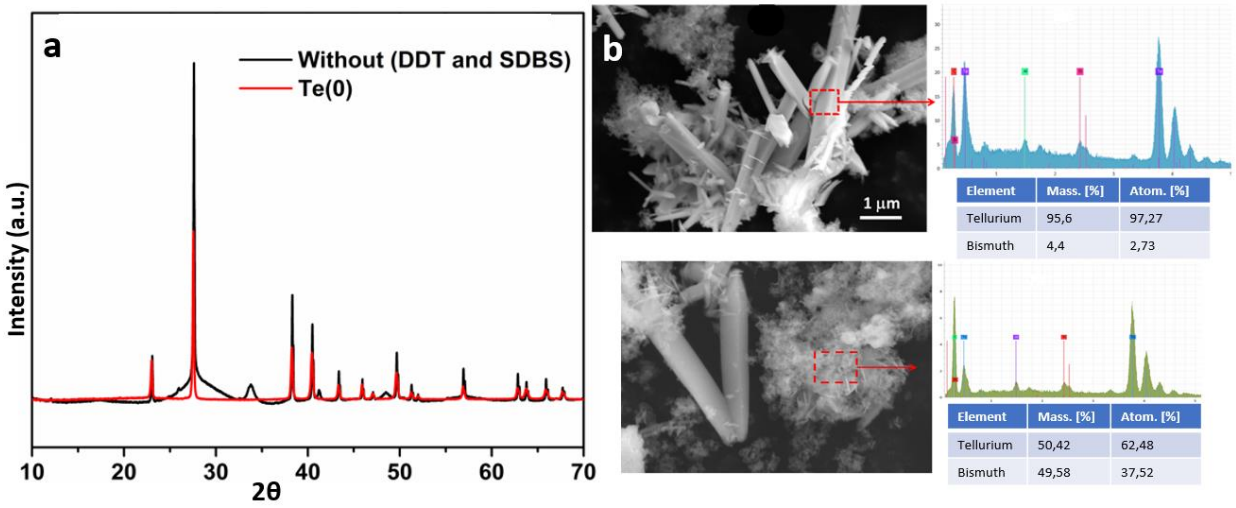

Figure – 2.1.3: a - X-ray diffraction patterns of pure Tellurium Te(0) (in red) and synthesized sample without using DDT (in black); b - SEM images and corresponding EDX spectra of the aggregates for the sample synthesized without using DDT

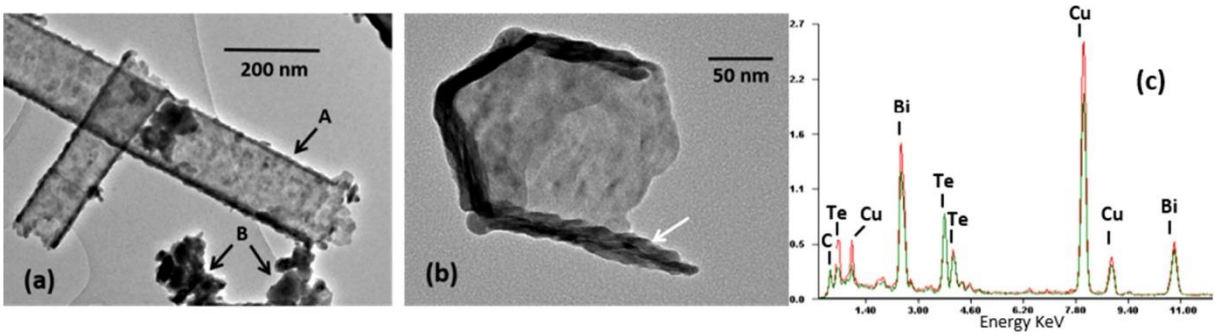

Figure – 2.1.4: a – TEM pictures of Bi_2Te_3 nanotubes and aggregates; b – zoom on a tube with spiral walls (white arrow), open ends of the tubes are clearly evidenced; c – superimposed EDX spectra respectively recorded on nanotubes (A) and aggregates (B).

TEM was used to investigate more precisely the morphology of these nanoparticles. The TEM picture in Figure-2.1.4a shows Bi_2Te_3 nanotubes (arrow A) with small nanoparticles aggregates (arrow B). The nanotubes diameter varies from one tube to another but an average value of 50–100 nm can be estimated. EDX analysis in Figure-2.1.4c confirms at the very low scale that the atomic ratio is in agreement with the chemical formula of Bi_2Te_3.

Figure-2.1.4a and b reveal the specific morphology feature of a hollow tube showing respectively its extended shape along its main axis with spiral walls and the opening of a tube shown on the image taken along its longitudinal axis. The thickness of the walls is estimated at 20–30 nm. These observations are in agreement with TEM characterizations reported in the literature.[144–146] No differences in the chemical formula can be observed in the two types of Bi_2Te_3 shapes. In all cases the Bi/Te ratio deduced from these analyses is close to 2/3, in good agreement with the nominal composition of the samples. On the EDX spectra carbon and copper peaks are systematically observed. These C and Cu contributions are coming from the holey carbon coated copper grid supporting the observed samples.

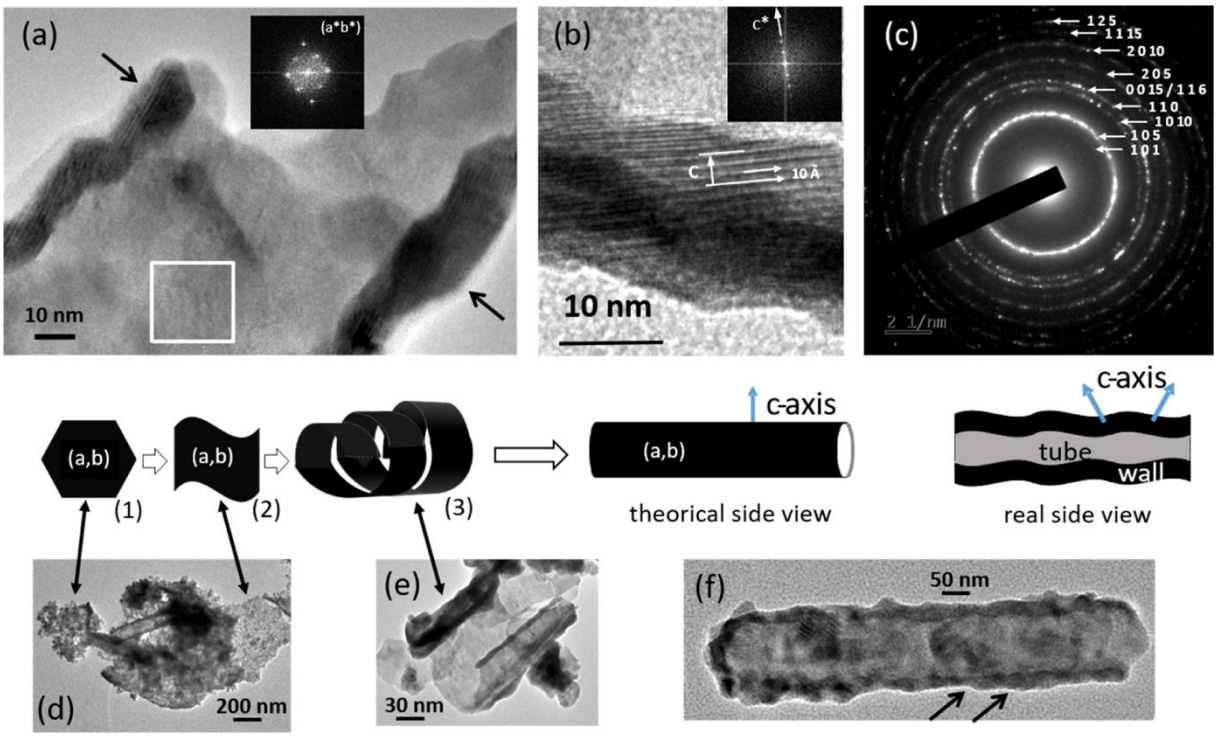

Figure – 2.1.5: a – TEM picture of a Bi_2Te_3 nanotube with its spiral wall indicated by black arrows; in inset Fast Fourier Transform of the white square area perpendicular to the plane of the wall showing the average hexagonal orientation of the plane of the crystals; b – HRTEM of a tube wall with white arrows indicating the c parameter close to 30.4 Å and the basic quintet of Bi_2Te_3 (close to 10 Å) in inset Fast Fourier Transform perpendicular to the wall where the C axis orientation is clearly evidenced in the wall of the tube , c – typical SAED diffraction pattern of the Bi_2Te_3 aggregates indexed referring to ref[6] parameters. d, e and f – Bi_2Te_3 typical images of respectively nanograin aggregates (d,1), flat sheets (d,2) and sheets beginning to roll (e,3) to form a nanotube (f)

In order to further investigate these nanotubes structure, HRTEM analyses have been performed. Figure-2.1.5a shows a TEM picture of a representative nanotube. The HRTEM picture in Figure-2.1.5b displays the atomic arrangements which evidence the good crystallinity of domains extending over 20–30 nanometres. The contrasts are blurred due to the fact that these small domains are slightly disoriented one to each other, revealing the poly-crystallinity of the tubes. A lot of defects and stacking faults are also clearly evidenced. Although Bi_2Te_3 is often referenced with rhombohedral settings, its description is easier using a hexagonal cell. Indeed, the hexagonal cell is made of layers of atoms stacked perpendicularly to the c-axis with the following stacking sequence $–Te^1–Bi–Te–Bi–Te^1–$. The superscript labelling refers and exemplifies the difference of bonding within the quintet, e.g., the Te layer is bonded to two Bi layers whereas the Te^1 layer is bonded to Bi on one side and to another Te^1 layer on the other. The $Te^1–Te^1$ bonding is of Van der Waals type whereas the interaction

between Bi and Te is rather ionic–covalent. This 5 layer-sequence is called a quintet and there are 3 quintets per unit cell. The cell parameters are a = 4.3835 Å and c = 30.360 Å at 77 K.[147] It is, therefore, reasonable to estimate the thickness of a quintet around 10 Å. The measurement in Figure-2.1.5b of a distance close to 10 Å along the c direction between two bright dots rows corresponds to the thickness of the quintet. The HRTEM observations correlate well with the structural features of Bi_2Te_3 crystalline structure. The fast Fourier transform performed in white square area perpendicular to the plane of the wall indicates the average hexagonal orientation of (a, b) plane of the crystals (inset in Figure-2.1.5a). HRTEM of tube wall endows us to evaluate the c parameter close to 30.4 Å (Figure-2.1.5b). Figure-2.1.5c displays SAED pattern of the sample. The good indexation according to literature data and hkl planes identification evidenced the confirmed Bi_2Te_3 rhombohedral, R(-3)m crystalline structure features. Figure-2.1.5b also shows that the c-axis is not exactly perpendicular to the nanotube axis. This slight disorientation towards that direction is caused by the orientation of the Bi_2Te_3 (a, b) planes from the nanotube wall plane probably caused by their formation via a rolling-up mechanism as previously proposed in the literature.[80,145] The observation of intermediate shapes particles in the powder like nanograin aggregates (Figure-2.1.5d) such as sheets (Figure-2.1.5d), sheets beginning to roll (Figure-2.1.5e) and nanotubes (Figure-2.1.5a and f) comforts the likeliness of this mechanism.

Recalling that one of the goals of the work is to use the synthesized nanoparticles as a filler to prepare hybrid composite with percolating Bi_2Te_3 network, 30% of nanotubes content in the sample is quite low to ensure the percolation of the particles at lower filler loading. Therefore, other strategies to increase the content of nanotubes are explored and reported in the following sections.

II.2 Preparation of Te-template rods

During our first attempts to increase the content of nanotubes in bismuth telluride nanoparticles synthesized according to method described in § II.1, we noticed that Bi-DDT could also react with Te^0 nanoparticles, by a diffusion process known as nanoscale Kirkendall effect. During such syntheses, the morphology of the final compound is governed by the morphology of Te^0. To obtain Bi_2Te_3 tubular particles, it is important to have elongated rod like Te^0 species as a template. Mechanism of synthesis by Kirkendall diffusion is discussed in § II.3, while in this chapter results of attempts to obtain better Te templates are discussed. Reactions in the following protocols were not carried out in 2 L reactor as in the previously reported reaction protocol, but in smaller conventional round bottom flasks in order facilitate the post reaction work up by scaling it down.

II.2.1 Reaction mechanisms

Sodium borohydride ($NaBH_4$) has been studied due to its potential for hydrogen generation, but later was extensively used as a reducing agent for metal ions to generate nanosized particles of zero valent/pure metals or metal borides.[148,149] Hydrolysis of $NaBH_4$ has potential to generate 0.213g of hydrogen per 1 g of the compound according to equation [1]:

$$NaBH_4 + 2H_2O \rightarrow NaBO_2 + 4H_2 \quad [1]$$

However, according to Chatenet et al, to use BH_4^- as a reducing agent and avoid its hydrolysis, reactions must be performed in alkaline media (pH>12).[150] In that case the following reduction reaction can take place:

$$BH_4^- + 8OH^- \rightarrow BO_2^- + 8e^- + 6\,H_2O \qquad [2]$$

The reaction of interest in our case is a reduction of Te(0) in water by $NaBH_4$ in a basic media (pH>13). Considering the reaction [2], it is reasonable to state that the following reaction takes place since the redox potential of Te^0/Te^{2-} is -1.14V:

$$4\,Te + BH_4^- + 8OH^- \rightarrow 4Te^{2-} + BO_2^- + 6H_2O \qquad [3]$$

The next mechanism to discuss is the oxidation of Te^{2-} back to Te(0) in contact of the solution with oxygen. Exact stoichiometry of the reaction is not presented in the articles, however Chen et al.[151] state that oxygen is used to precipitate the Te^{2-} ions in a similar reaction.

They do not present any mechanism but considering the alkaline pH of the solution, could probably be reduced following one of the to the standard oxygen reduction reaction (ORR)[152]:

$$O_2 + 2H_2O + 4e \rightarrow 4OH^- \qquad [4]$$

Overall reaction can be estimated as following:

$$2Te^{2-} + O_2 + 2H_2O \rightarrow 2Te + 4OH^- \qquad [5]$$

II.2.2 Tellurium template synthesis

II.2.2.a Standard protocol (Protocol 2.1)

Te template rods are obtained by precipitation of the Te^{2-} ions, which were prepared as in the first step of the Bi_2Te_3 synthesis via rolling up mechanism. Unless other amounts of chemicals are stated, in a standard synthesis protocol metallic Te is reduced by placing 3.36 g (84 mmol) of NaOH, 1.2 g (9.4 mmol) of Te and 1.45 g (38 mmol) of $NaBH_4$ in 450 ml of degassed water and refluxing for 3 h at 100°C under Ar flow. Reduction is visually accompanied by effervescence and changing of the reaction mixture from suspension to dark purple solution, then to clear pale purple solution. The effervescence, suggest that partial $NaBH_4$ hydrolysis also takes place leading to the hydrogen formation.

After complete reduction of Te, it is re-precipitated by allowing the oxygen from air to access the reaction mixture. After complete precipitation of Te, which visually observed as formation of black-grey suspension in a clear transparent solution, it is filtered and washed repeatedly by water, EtOH and acetone, then dried.

This standard procedure is followed several times, each time changing a single parameter, to evaluate the effect of changed conditions on the quality of Te rods. Varied parameters are stirring intensity, oxygen access time, and oxygen application mode.

All the reactions conducted with this protocol produce pure Te phase nanoparticles with elongated morphology of particles according to its XRD spectrum and SEM images. XRD spectra of all synthesised samples presents the peaks pattern of trigonal tellurium with space group P 3_121 (blue spectrum on Figure 2.2.2). Matching and refinement of XRD spectra were carried out on Maud software in comparison with the standard Te phase[153], data taken from crystallography open database (COD). Formation of particles proceeds by reaction of the solution with oxygen, which is applied through the surface of the solution. Therefore, Te particles start to form on the surface, and

later due to mixing, and in certain cases due to saturation of the solution surface, particles start to appear in the solution. SEM images of synthesized Te particles show that it consists in elongated rod like structures (Figure-2.2.1a, A) and bigger sized block like structures with small aspect ratio (Figure-2.2.1a, B). The size of elongated particles varies vastly from several hundred nanometres up to 10 µm. Closer examination of those particles (Figure-2.2.1b) shows that they have sharpened ends and hexagonal cross-section, which confirms hexagonal unit cell (trigonal crystal structure). Therefore, later on those particles referred to as "rods with hexagonal cross section". Block like particles have bigger size, and if due to small aspect ratio they are considered as spheres, their diameter varies from 5 µm up to 20 µm. Interestingly, the majority of the block particles form sheet like agglomerations, consisting mainly of big blocks, but mixed with occasional rods (Figure-2.2.1c). When the reaction stirred at slow rate, those agglomerations first cover the surface of the solution (Figure-2.2.1d), therefore it is possible to isolate them and observe by SEM.

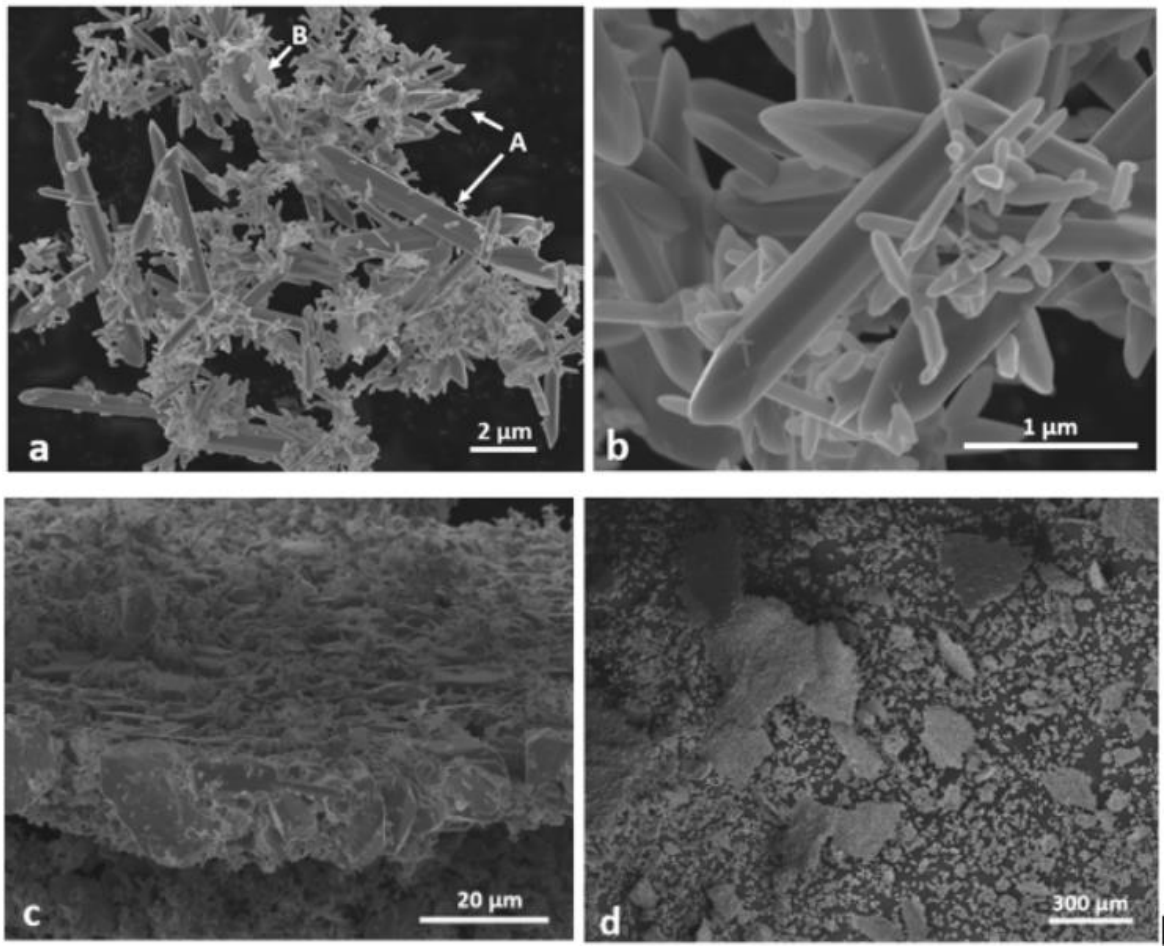

Figure – 2.2.1: SEM images of Te particles prepared according to the Protocol 2.1: a – general view: A - Te-rods with hexagonal cross-section, B - Te blocks; b – closer view of Te rods with hexagonal cross-section; c – agglomeration consisting of B type blocks and occasional Te-rods; d – particles from the surface layer of the reaction solution with view of giant agglomerations

The role of prepared Te particles is to be a template for the formation of Bi_2Te_3 tubes by diffusion, therefore their morphology has to be rod like, in our case rods with hexagonal cross-section. To improve the quality of the template, it is favourable to eliminate or decrease the amount of shapeless blocks and increase the ratio of rods. For this purpose, the effect of different reaction conditions on the final morphology of Te particles have been investigated.

II.2.2.b Effect of stirring intensity

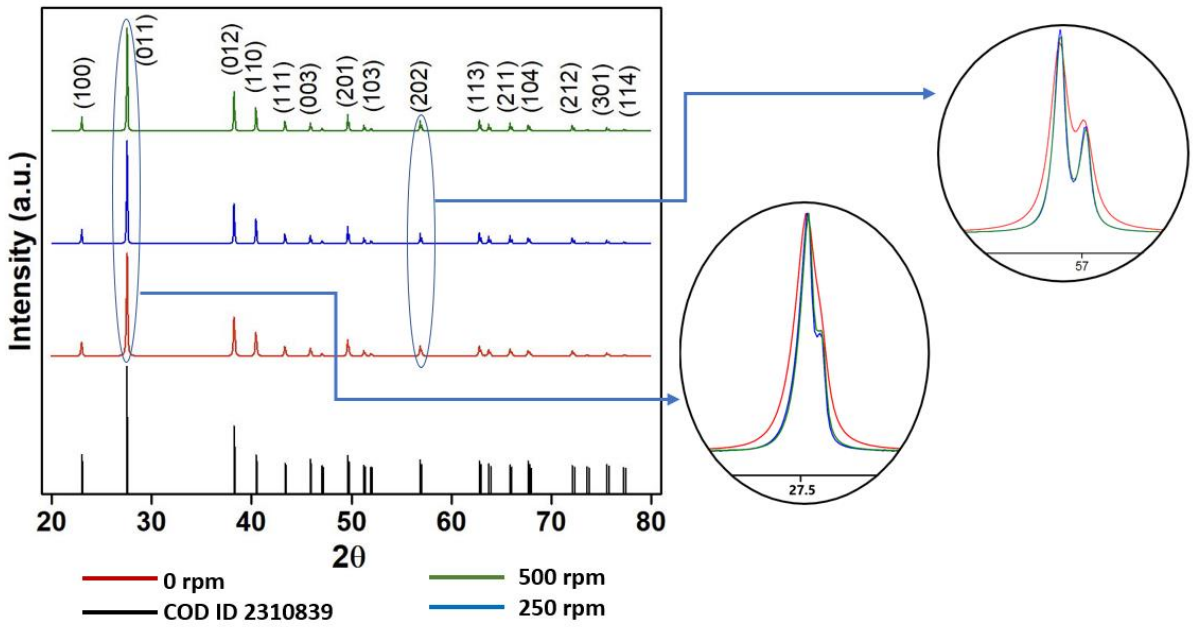

Figure – 2.2.2. XRD spectra of Te nanoparticles prepared according to standard protocol (II.2.2.a) under different stirring speed in comparison with the standard from COD (COD ID 23108039)

Firstly, the change of the stirring intensity on the final particle morphology was investigated. Reduction of Te is carried out in a standard way, but stirring intensity varied on the step when the reduced Te solution is reacted with oxygen while being cooled down. The oxygen is applied to the reaction mixture from the top of the reaction flask through needle thin hole, therefore gradually through the surface of the reaction solution. Slow rate of oxygen dissolution in a such supply mode lets Te^{2-} closer to the surface of the solution react first, forming above mentioned agglomerations (Figure-2.2.1c and d) consisting big blocks and some rods. It is certain that the concentration of oxygen on the surface is much higher than in the solution, therefore, particles (crystals seeds) forming on the surface have quick access to higher amount oxygen, which results in their size being bigger. High rate of crystal formation does not allow it to arrange itself in an energetically favourable shape (elongated hexagonal). Formation

of such agglomerations is not favourable, firstly because they mainly consist of big blocks and secondly, they are densely packed, which makes their further separation into individual particles difficult or impossible. Increase of the stirring intensity might help to decrease the size of particles formed on the interface by disturbing the crystal growth, as well as preventing agglomeration of the particles. Also, increased stirring rate increases the oxygen dissolution rate, thus allowing the rate of Te oxidation in the solution to increase. To verify this hypothesis, along with the standard stirring rate of 250 rpm, the reaction is carried out at without stirring and at 500 rpm.

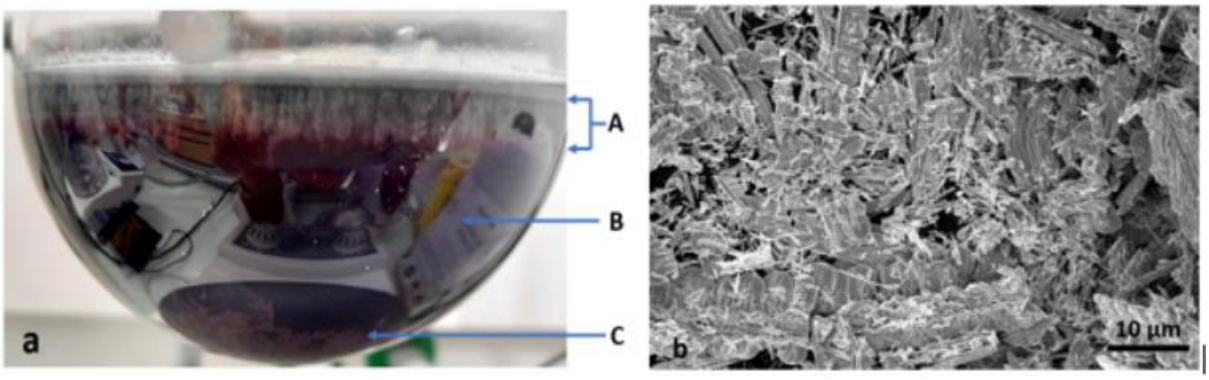

Figure – 2.2.3: a – Precipitation of Te without stirring after 3 days: A - Te particles growing downwards; B - reduced Te solution (darkens due to certain amount of oxygen); C - Te particles fallen from the top forest due to vibrations; b – SEM images of Te particles precipitated without stirring

In the absence of stirring Te particles are formed first on the interface, then grow downwards from top, like a forest turned upside down (Figure-2.2.3a: A). Due to limited access of O_2 reaction proceeds very slow and does not reach complete precipitation in one week. SEM images of precipitated part (Figure-2.2.3b) shows that it consists mainly of big continuous particles without specific morphology, some of them being feather like made from collection of rods or wavy structures. Some occasional rods also encountered, but their proportion is negligible. Increasing the stirring speed up to 500 rpm triggers vigorous stirring forming vortex. It allows to avoid formation of agglomerations and accumulation of particles on the surface. As a result, the amount of big blocks drastically decreases. Therefore, vigorous stirring (500 rpm) is considered as a favourable stirring speed. Figure-2.2.2a shows the XRD spectra of Te particles prepared at different stirring rate. Comparison of normalized diffraction patterns (Figure-2.2.2a zoomed insets) shows that peaks of Te particles synthesized in the absence of stirring has broadening in comparison with other two, which suggests that crystal domains are smaller in this sample. Although the particle size is considerably bigger in the absence of stirring, the particles are made of smaller crystalline domains.

II.2.2.c Influence of Oxygen access duration

Variation of the oxygen access duration during the precipitation step proves that the formation of Te^0 particles indeed proceeds via redox reaction involving oxygen (reaction [5]). In the absence of oxygen upon cooling down, if the reaction mixture is well sealed, Te^{2-} ions can stay in the solution without precipitation for weeks. When the oxygen (air) allowed to enter the reaction flask, as described above, but only for limited amount of time, then the solution is sealed again, only partial precipitation takes place. At short periods of oxygen access as 3 to 30 min, only partial precipitation takes place, which is visually noticed as a reaction solution remaining dark purple coloured with some particles in it for days after it is cooled down. Allowing the oxygen access only for 1h and then sealing it, leads to increase of the time required for complete precipitation, which is visually observed as a formation of suspension in a clear solution, up to 4h. While when the oxygen access allowed till the completion of the reaction, in a standard reaction, complete precipitation takes place between 2 to 3 h. Ceasing the oxygen access probably mainly affects the concentration of dissolved oxygen in the solution, leading to its decrease. Therefore, more reaction takes place in the interface, as the surface remains saturated with oxygen, leading to slight increase of unfavoured Te blocks ratio in the final powder. Therefore, it can be concluded, that for increase of the favoured elongated morphology in the precipitated Te, keeping the constant oxygen access is beneficial.

II.2.2.d Influence of Oxygen introduction mode

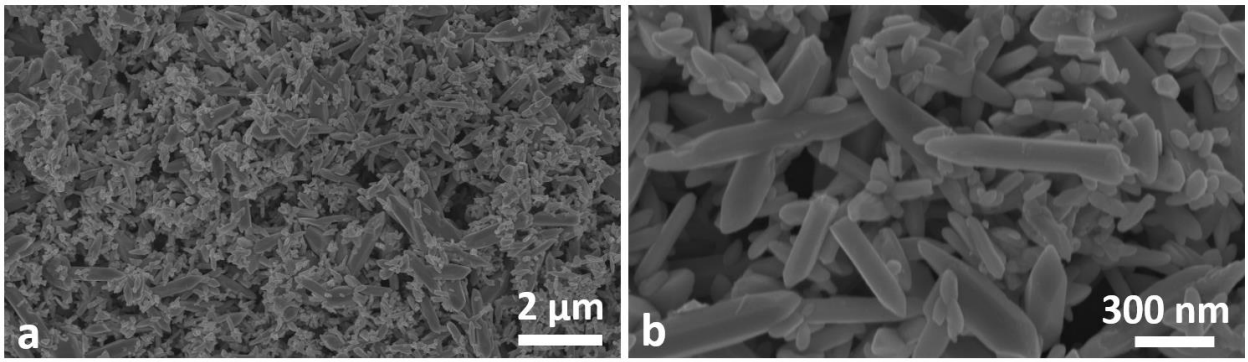

Figure – 2.2.4. SEM images of Te particles precipitated by direct oxygen application

Last, the mode of oxygen introduction on the morphology of Te particles was evaluated. In the standard protocol oxygen is introduced through the hollow needle inserted into the septum sealing the reaction mixture, where it reaches the solution through its surface. In the alternative method, oxygen is introduced directly into the solution by inserting a needle attached

to the air filled balloon into the solution, otherwise described as bubbling. The idea was to increase the oxygen concentration in the solution in order to favour the formation of the particles in the solution, rather than at its surface. As mentioned earlier, particles formed at interface, due to high concentration of oxygen at the surface, have tendency to grow into big sized irregular shaped blocks and also form dense packed sheet like agglomerations of particles (Figure-2.2.1c and d). Additionally, to avoid the accumulation of high concentration of O_2 at the surface, as a result of bubbling, another needle attached to argon filled balloon is also inserted into the solution. This novel oxygen introduction method indeed, allows to avoid formation of sheet like agglomerations of particles and vastly decreases the amount big blocks, thus improving the quality of the template. The major drawback of such direct oxygen introduction method is that formed Te rods are shorter (Figure-2.2.4). In general, two major clusters of rods forms: small rods with average length of 200-300 nm and long rods with length of 2 to 3 µm. Decrease of the rods size is likely to be triggered by increase of the oxygen concentration and thus, simultaneous formation of many seeds. This hypothesis is supported by increased rate of complete the precipitation, which occurs in 1 h in comparison with 2 to 3 h in standard protocol. Figure-2.2.5 shows the XRD spectra of Te particles prepared at two different oxygen application modes and direct application of oxygen leads to slight decrease of crystalline domain size.

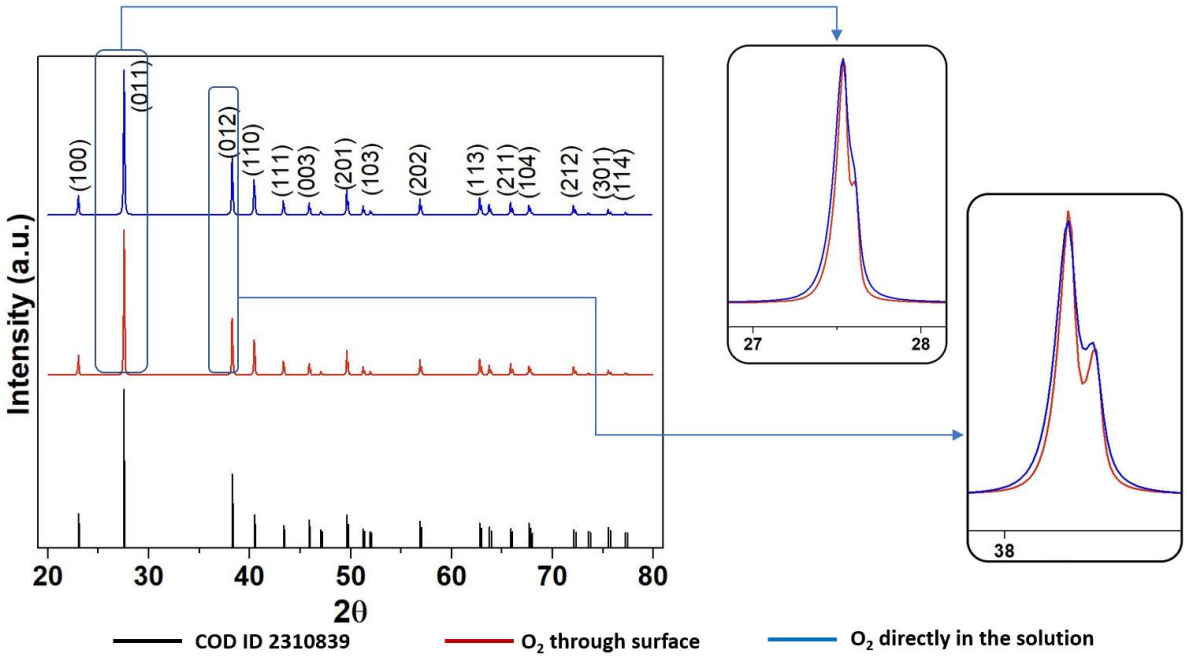

Figure-2.2.5. XRD spectra of Te nanoparticles prepared according to protocol 2.1 changing the oxygen introduction mode

Considering the results summarized in table-2.2.1, the set of the following conditions (highlighted in green) is concluded to be the best to improve the quality of Te hexagonal rods by increasing the rods ratio to the unfavoured irregular blocks: increased stirring rate to avoid surface agglomeration and improved oxygen application way via injection in the solution.

Table-2.2.1. Effect of reaction and precipitation conditions on the morphology Te particles (favoured conditions highlighted in green)

Stirring intensity	**0 rpm**	**250 rpm**	**450 rpm**	
Results	Isotropic big particles	Mixture of rods and blocks, flakes consisting from agglomeration of blocks	Mixture of rods and blocks with decreased amount of the last, no flakes	
Oxygen supply duration	0 min	Up to 30 min	1h	∞
Results	No precipitation	Partial precipitation	Complete precipitation, slightly higher amount blocks	Complete precipitation, highest ratio of hexagonal rods
Oxygen supply mode	Through surface	Through solution		
Results	Mixture of rods and blocks, flakes consisting from agglomeration of blocks	Mainly hexagonal rods, but shorter than usual (small aspect ratio), very few small blocks		

In order to further improve the quality of the tellurium templates, alternate protocols have been developed. First logical approach is to introduce surfactant. SDBS is selected as a surfactant thanks to its frequent application to prepare elongated nanoparticles, as well as Te rods.[25]

II.2.3 Surfactant assisted long Te rods synthesis

In this second method (Protocol 2.2), Te template is prepared with the aid of surfactant SDBS. As in the standard reduction procedure Te is reduced by placing 3.36 g (84 mmol) of NaOH, 1.2 g (9.4 mmol) of Te and 1.45 g (38 mmol) of $NaBH_4$ in 450 ml of degassed water and refluxing for 3 h at 100°C under Ar flow. Solution of reduced Te is then cooled down, but still under Ar flow for 2 h (until it is close to the room temperature) to not allow the Te^{2-} to react with oxygen and precipitate. Then 0.16 g (0.45 mmol) of SDBS is dissolved in a reaction

mixture. After complete dissolution of SDBS, oxygen is introduced into solution through a needle attached to an air-filled balloon. Needle is inserted into solution, allowing direct contact of air with Te ion particles in the solution. On the other hand, to avoid accumulation of oxygen on the top of solution, thus preventing the precipitation from the surface, a needle attached to an Ar-filled balloon is also attached. Solution is allowed to stir for 1 h and after formation of black stabilized suspension, it is filtered and washed repeatedly with water, EtOH and acetone and dried.

Trigonal structure of Te crystals favours its growth along 001 plane, giving it tendency to form particles elongated in one direction (rods, tubes, belts).[83,154] Although method to prepare Te rods was already set above, increasing the rods ratio came in cost of decrease of their length. As all the possible parameters in the Standard synthesis protocol (II.2.2) were varied, additional approach to increase the aspect ratio of the Te rods was searched. Despite number of reported synthesis methods of Te particles from solution with controlled morphology and dimensions[83,155–158], in order to keep reaction conditions similar to the already developed method, which would allow further synthesis of Bi_2Te_3 synthesis in one pot, we decided not to vary a lot the conditions from the Standard protocol.

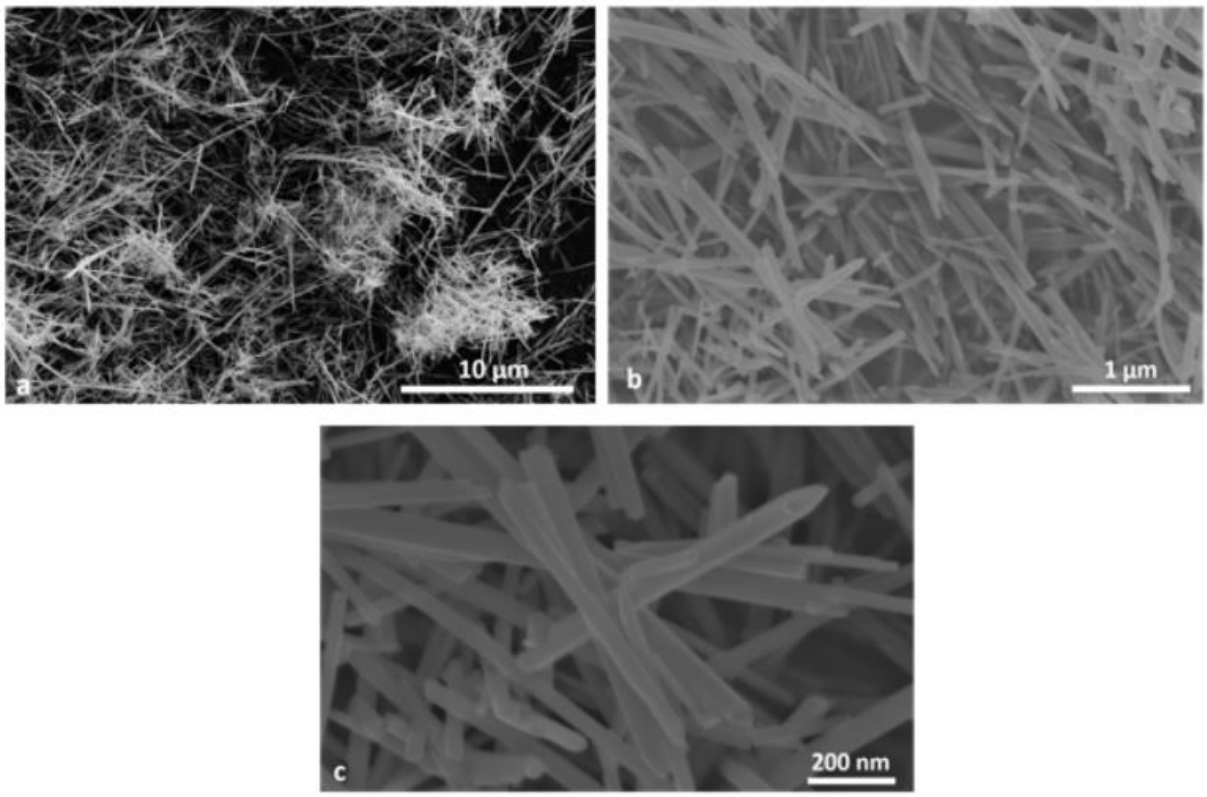

Figure-2.2.6. SEM images of Te particles prepared with SDBS (Protocol 2.2)

Reaction carried out according to this protocol 2.2 produces Te nanorods with higher aspect ratio than in the synthesis without surfactant (Figure-2.2.6). The length of the rods varies from 2 µm up to 10 µm, but small portion of rods with length as 500 nm also exist. Apart from change in length, diameter of the rods is decreased. Although the aspect ratio of rods is not homogeneous throughout the sample, but has a tendency to increase with the length of the rod, if the 500 nm length rods prepared in standard Te reduction way (improved protocol 2.1) has a diameter of 100 nm, rods prepared with SDBS with corresponding length have diameter of only 50 nm. This difference increases with increasing length of the rods, as the diameter of Te rods prepared with SDBS remains small. Another noticeable difference in the rods is that the last ones lose the hexagonal cross-section with apparent edges and round up.

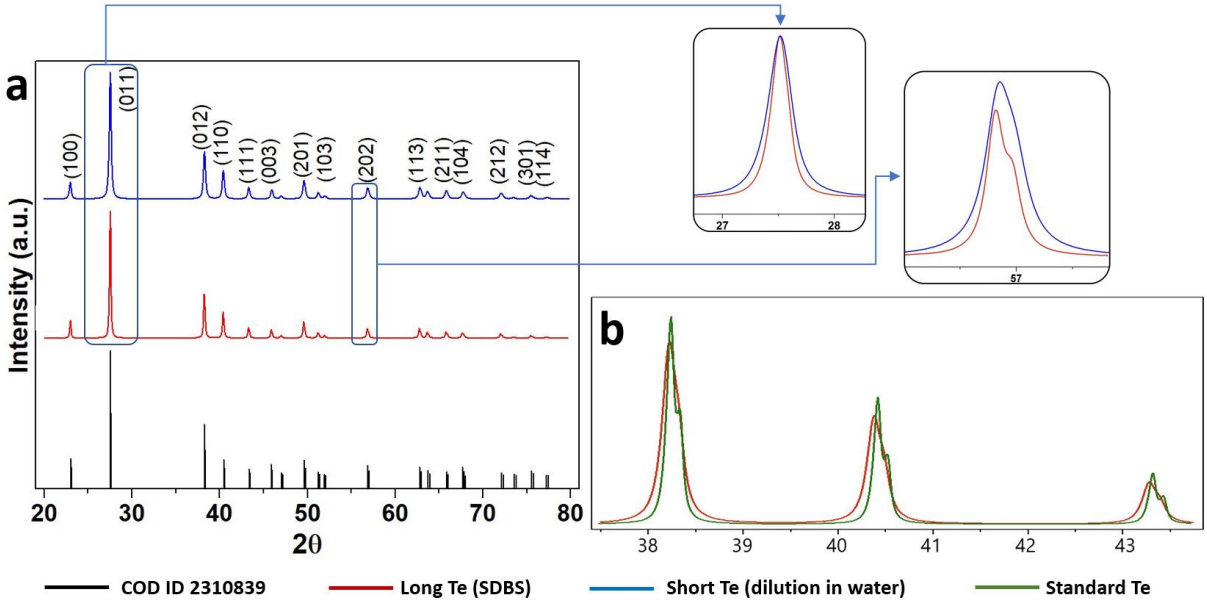

Figure-2.2.7. a - XRD spectra of long Te nanoparticles prepared with SDBS (Protocol 2.2) (red line, long Te rods) and short homogeneous Te nanoparticles prepared by dilution (Protocol 2.3) (blue line, short Te rods); b – Comparison of peak broadening of long Te rods (red line) versus Te prepared by improved standard protocol (blue line)

The high length and relatively small diameter of the rods is attributed to the hindering effect of SDBS as in many systems.[158,159] SDBS ions (anions) are adsorbed on/attaches to the side faces of growing Te hexagonal rods ({100} family plane faces) and hinders its growth towards normal to those planes. In turn, it facilitates the growth of crystal along those planes. Figure-2.2.7a (red line) shows XRD peaks of Te particles which corresponds to trigonal Te phase. Figure-2.2.7b depicts the section of XRD pattern of these Te particles in comparison with the XRD peaks of Te prepared without surfactant. In spite the considerable increase in the rods length, the peaks

are broader in the first case. It suggests that long Te rods prepared by SDBS are polycrystalline with smaller crystal domain size.

II.2.4 Synthesis of short homogeneous Te rods (Protocol 2.3)

Earlier described methodologies allow to obtain two types of Te rods with high size distribution of the particles, having either length from 200 nm up to 2 µm for synthesis without surfactant, and 2-10 µm for the surfactant assisted synthesis. An alternative protocol in which the Te^{2-} solution is injected in an oxidation bath has been experimented.

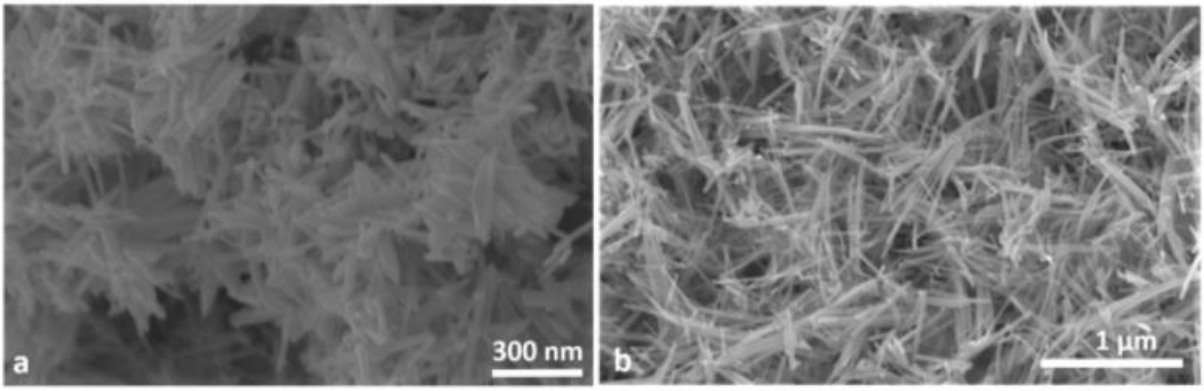

Figure-2.2.8. Te rods prepared according to protocol 2.3: a – without surfactant; b- with SDBS

The third method of Te-template preparation aims at obtaining small rods by fast precipitation. For that purpose, the reduction step of Te (conducted as in standard protocol), the solution is cooled down to room temperature under Ar flow to prevent the precipitation. 60 ml of the reduced Te solution is then taken out by syringe, without allowing in any air bubbles, and gradually injected into 360 ml of distilled water or of an aqueous SDBS solution under stirring. During the injection, the final solution first turns rusty then into black. After 10 min of stirring under air, Te fully precipitates. Te powder is then filtered, washed by water repeatedly and then by acetone and dried.

This method does not allow to continue the synthesis of Bi_2Te_3 in one pot, however it produces Te rods with narrower size distribution: length 200-350 nm, diameter 25-50 nm (Figure-2.2.8a) even without SDBS. Using SDBS surfactant in this method by dissolving it in the water before the injection of reduced Te solution leads to increase of the formed Te rods length, however, it also increases the size distribution range of the rods. The length of rods with application of 7 mmol/L of SDBS produces rods with lengths ranging from 200 nm up to 1 µm (Figure-2.2.8b). It can be concluded that for the preparation of Te rods, size distribution is best

controlled with shorter rods. It worth noting that the redox reaction, when reduced Te solution is injected, proceeds very fast. It completes in approximately 10 mins, producing suspension with clear solution and silvery particles, even in the absence of direct oxygen application via bubbling, but only through surface. Figure-2.2.7a blue line shows XRD pattern of Te particles which corresponds to trigonal Te phase.

Improvement of the Te nanoparticles morphology towards increase of the nanorods ratio is expected to improve the morphology of Bi_2Te_3 towards increase of the nanotube ratio when the Te is used as sacrificial template. In the following section of the chapter the Te preparation methods, discussed above, were integrated into Bi_2Te_3 synthesis methods via nanoscale Kirkendall diffusion.

II.3 Synthesis of Bi_2Te_3 nanoparticles via in-situ templating mechanism

II.3.1 Mechanism

Synthesis methods of Bi_2Te_3 nanoparticles reported in this section of the thesis follows nanoscale Kirkendall diffusion mechanism. This mechanism, schematically depicted on figure-2.3.1, otherwise called non-equilibrium diffusion, because the diffusion rate of two elements are not equal. In a conventional case, the template core element (Te rod in our case) has higher diffusion rate towards the shell – Bi, which results in formation of hollow structures.

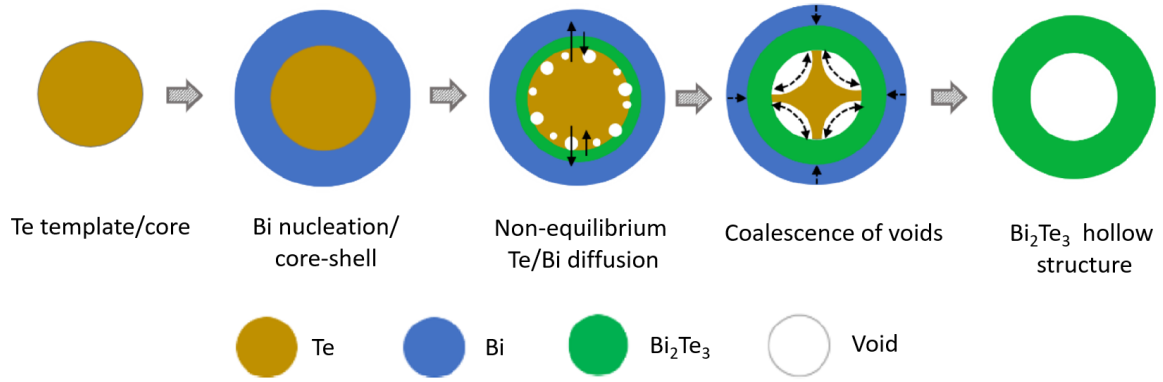

Figure – 2.3.1. Schematic illustration of Bi_2Te_3 nanotube formation by nanoscale Kirkendall diffusion, view from top of the tube[160]

Synthesis of Bi_2Te_3 hollow nanostructures by nonequilibrium diffusion was first reported by Zhang et al.[81] A solution of $BiCl_3$ is added to a suspension of Te long rods and the reaction proceeds at 160°C in ethylene glycol. A gradual change of the phase from pure Te to Te-Bi_2Te_3 and eventually pure Bi_2Te_3 phase is observed over time. The dimensional distribution of the final Bi_2Te_3 is in accordance with the dimensions of core Te rods. Another work reported by Wang et al. on preparation of Bi_2Te_3 hollow species by nanoscale Kirkendall effect highlights the importance of using a reducing agent[161] to form Bi^0 which further interacts with Te template following nonequilibrium diffusion route. In the absence of sufficient amount of the reducing agent, Bi remains in ionic state and diffusion does not take place.

Number of other articles reporting similar synthesis routes of Bi_2Te_3 hollow nanostructures via Kirkendall effect under reflux were also published.[99,101,104,160,162] In these synthesis procedures mainly Te(0) and $BiCl_3$ are used as precursors along with hydrazine hydrate reducing agent and various surfactants. Another common feature for those reported

synthesis procedures is that the final Bi_2Te_3 is formed in glycols, either EG or TEG, at 160°C or higher temperatures under reflux. Only, Kim et al reported the synthesis of Bi_2Te_3 at lower temperature, when nanotubes were obtained in the mixture of oleic acid-oleylamine and smaller portion of precursor carrying trioctylphosphine at 85°C[154], which suggests that it can be performed at lower temperatures.

We chose to use a low temperature protocol similar to the above described reported routes, but without adding a reducing agent to reduce the Bi^{3+} ions into Bi^0 species, since we use $Bi[DDT]_3$ complex solution as Bismuth source. Thiolate anion in the complex reduces the Bi^{3+} ions on the template surface to Bi(0) through electron transfer and forms thiolate radicals, which eventually forms disulfate. Thus, this process eliminates the use of aggressive reductant.

II.3.2 One pot Synthesis of Bi_2Te_3 by in-situ templating

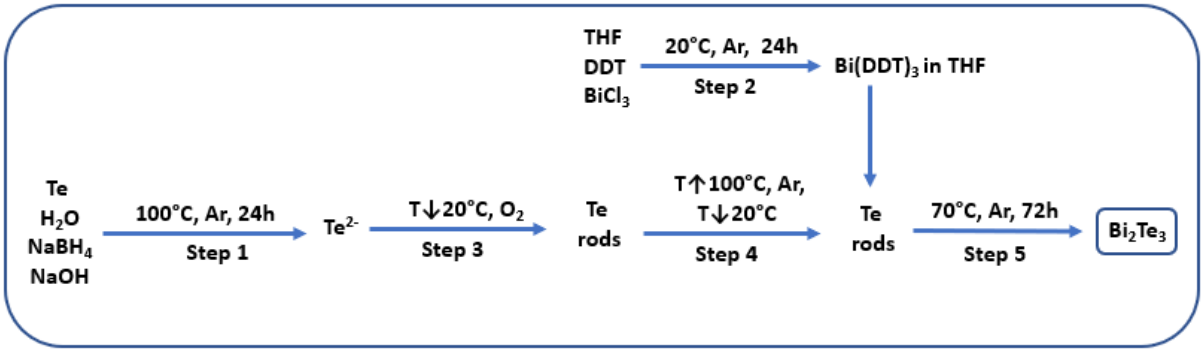

Scheme-2.3.1. General synthesis procedure for Bi_2Te_3 via diffusion mechanism on in-situ synthesized templates

General synthesis procedure for Bi_2Te_3 nanoparticles via templating is depicted on Scheme-2.3.1. The reaction consists of 4 main steps. In the first step Te is reduced by placing 3.36 g (84 mmol) of NaOH, 1.2 g (9.4 mmol) of Te and 1.45 g (38 mmol) of $NaBH_4$ in 450 ml of degassed water and refluxing for 24h at 100°C. First 2 hours of reflux is carried out under Ar flow to ensure the removal of hydrogen gas. The remaining time of reflux is carried out under steady Ar atmosphere. In the following step (Step-3) reduced Te-solution is slowly cooled down by removing the heat source and allowing slow, but steady air access for 2h, through a needle attached to the top of the reaction flask. This leads to precipitation of Te. Such process of Te precipitation corresponds to the standard process of Te template preparation (Protocol 2.1 in the previous section of the chapter). Since the inert atmosphere of the reaction mixture is compromised by air/oxygen, in the step 4 the reaction mixture is degassed by Ar under reflux, and again cooled down without breaking the Ar atmosphere. Step 2 is carried out in a separate reaction flask. 25 ml (104 mmol) of 1-DDT and 2.01 g (6.37 mmol) of $BiCl_3$ are placed in 125 ml of degassed THF and stirred under Ar atmosphere for 24h until complete dissolution of the salt. Formed Bi-DDT complex is then transferred into re-precipitated Te suspension via cannula without breaking the inert atmosphere in both flasks. The final reaction mixture is refluxed under moderate stirring for 72h. Obtained Bi_2Te_3 powder was filtered, washed repeatedly with THF, acetone, EtOH, H_2O and dried. This protocol is referred as protocol 3.1.

This reaction yields rhombohedral Bi_2Te_3 phase according XRD spectra (Figure-2.3.2 red line). Peaks positions and intensities are in a good agreement with XRD spectra of standard Bi_2Te_3 phase[163] with space group R3m-H from Crystallography Open Database (COD ID 9011962). No additional peaks were observed, which allows to conclude that the sample is single phase Bi_2Te_3.

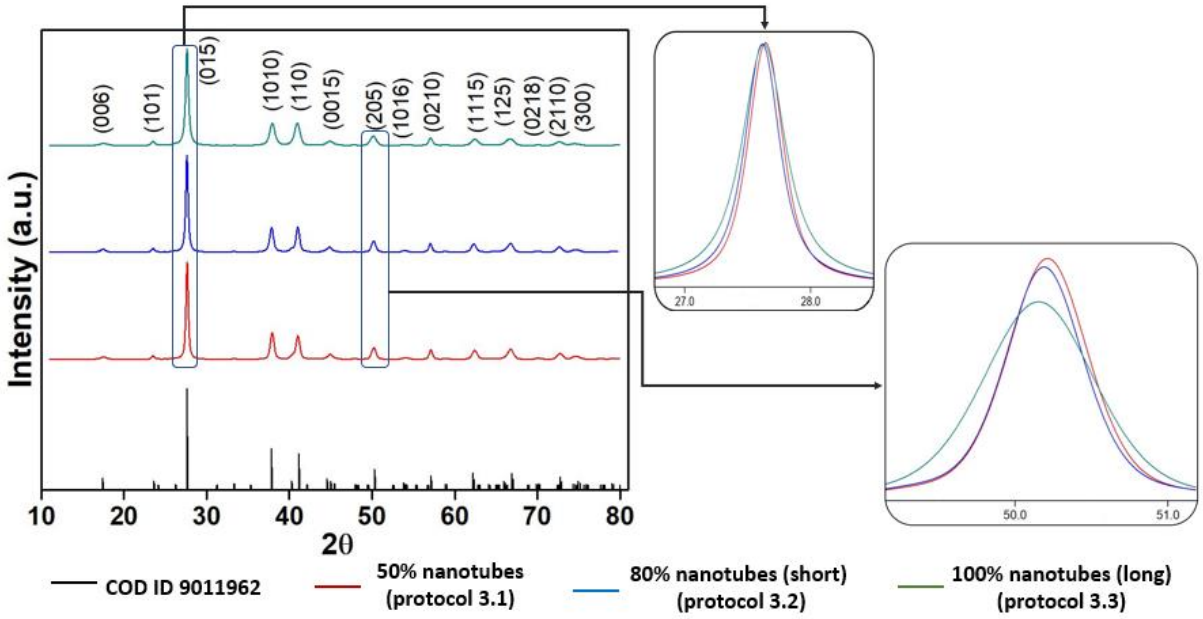

Figure-2.3.2. XRD spectra of synthesized Bi_2Te_3 nanoparticles in comparison with the standard from COD (COD ID 9011962)

Morphologically, according to SEM images (Figure-2.3.3), these particles consist in a mixture of tubes (a), grain like short particles (b) and isotropic particles (c). The length of the tubes varies from 500 nm up to 2.5 µm, with diameters ranging from 150 nm up to 500 nm, increasing proportionally with the length. Few large tubes with the length up to 6 µm are also encountered. Majority of the tubes have closed ends, but several with open ends. Open ends are apparent in bigger sized tubes, which allows to estimate a wall thickness of approximately 100 nm for the tubes with diameter of 500 nm (length approximately 2.5 µm). The grains have length from 100 nm up 700 nm. The grains have tendency to be elongated having shorter dimensions perpendicular to the length (diameter). This tendency is apparent with the increase of the particle size: small particles closer to spherical morphology, while longer ones close to the closed tubes. The size of bigger grains exceeds to the size of small tubes, however they are designated as grain like, because in the powder they are encountered along with small sized grains. Isotropic particles are too irregular to characterize, in terms of shape and size. The surface of all particles is rough. Volume fraction of tubes and grains (since they meet elongated particles definition) is approximately 50% from analysis of small fraction of Bi_2Te_3 powder by SEM. Therefore, sample prepared by above procedure is designated as Bi_2Te_3 with 50% nanotube content. Since these particles might not be anisotropic enough for the processing of nanocomposites, the protocol has been improved to increase the quality of the tellurium templates.

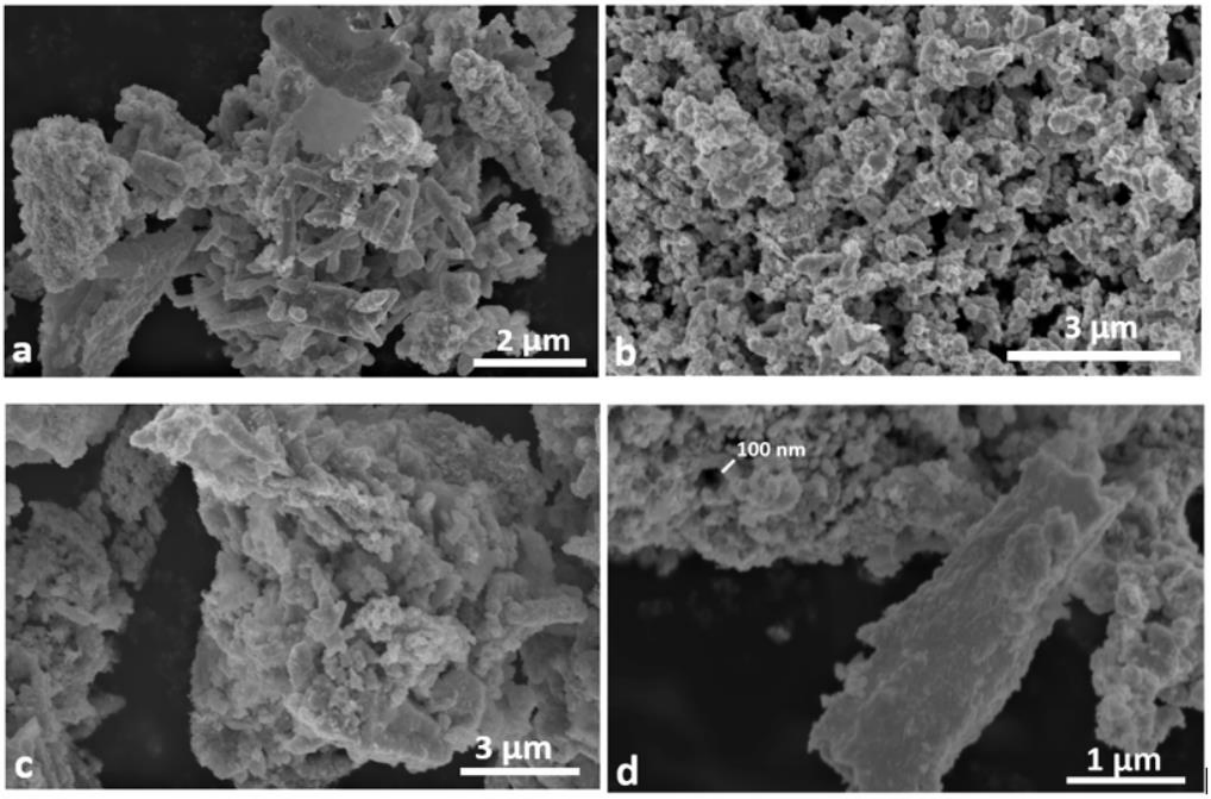

Figure-2.3.3. SEM images of Bi_2Te_3 nanoparticles with 50% nanotube content (Protocol 3.1): a – tubes; b – grains; c – isotropic particles; d – tubes in grains

II.3.3 Improvement of the protocol for One pot Synthesis of Bi_2Te_3 by in situ templating

The protocol of Bi_2Te_3 by in-situ templating has been modified to evaluate the effect of the tellurium template formation conditions on the quality and yield of the Bi_2Te_3 nanoparticles. As described in the previous chapter, we first played on stirring intensity and oxygen introduction method, then developed a surfactant assisted oxidation step (which produces long tellurium rods) and finally used a 2 steps synthesis from previously isolated tellurium rods.

II.3.3.a Improved oxygen introduction mode (Protocol 3.2)

In order to improve the quality of the Bi_2Te_3 nanoparticles, the procedure of template formation has been improved according to the results previously obtained in § II.2. After the reduction of Te in a standard way, upon cooling down, the oxygen is introduced via needle attached to an air-filled balloon. The outlet end of the needle is inserted into the solution, thus

facilitating better interaction of oxygen molecules with Te ion particles in the solution. Precipitation is carried out under vigorous stirring 450 rpm to avoid formation of particles on the surface of the solution. Along with the air-balloon, Ar-balloon is also inserted into the solution in the same manner to avoid accumulation of air on the surface of the solution. Precipitation is carried out under vigorous stirring 450 rpm to prevent formation of big sized particles on the surface of the solution. The rest of the reaction carried out according to the protocol 3.1.

Composition of the particles remains to be pure Bi_2Te_3 phase with space group R3m-H according XRD spectra in comparison with standard (Figure-2.3.2 blue line). Direct introduction of oxygen, as described in the previous section of the chapter (II.2), leads to an increase of the reaction rate, which in turn results in shorter Te templates (Figure-2.2.4), but with narrower size distribution. Morphology of the final Bi_2Te_3 particles changes accordingly: majority of the particles have length in the range of 300 nm-500 nm and diameter 50 nm (Figure-2.3.4), with very few portion of longer particles (Figure-2.3.4c). Open ends of the tubes are less apparent than previously (Figure-2.3.3), but coincide with the earlier conclusion that the clear open ends are encountered in bigger sized tubes. The surface of the particles remains to be rough. The ratio of tubes to random particles can be estimated to be up to 80% according to SEM images. Current protocol designated as protocol 3.2 and the sample obtained by it as Bi_2Te_3 with 80% nanotube content.

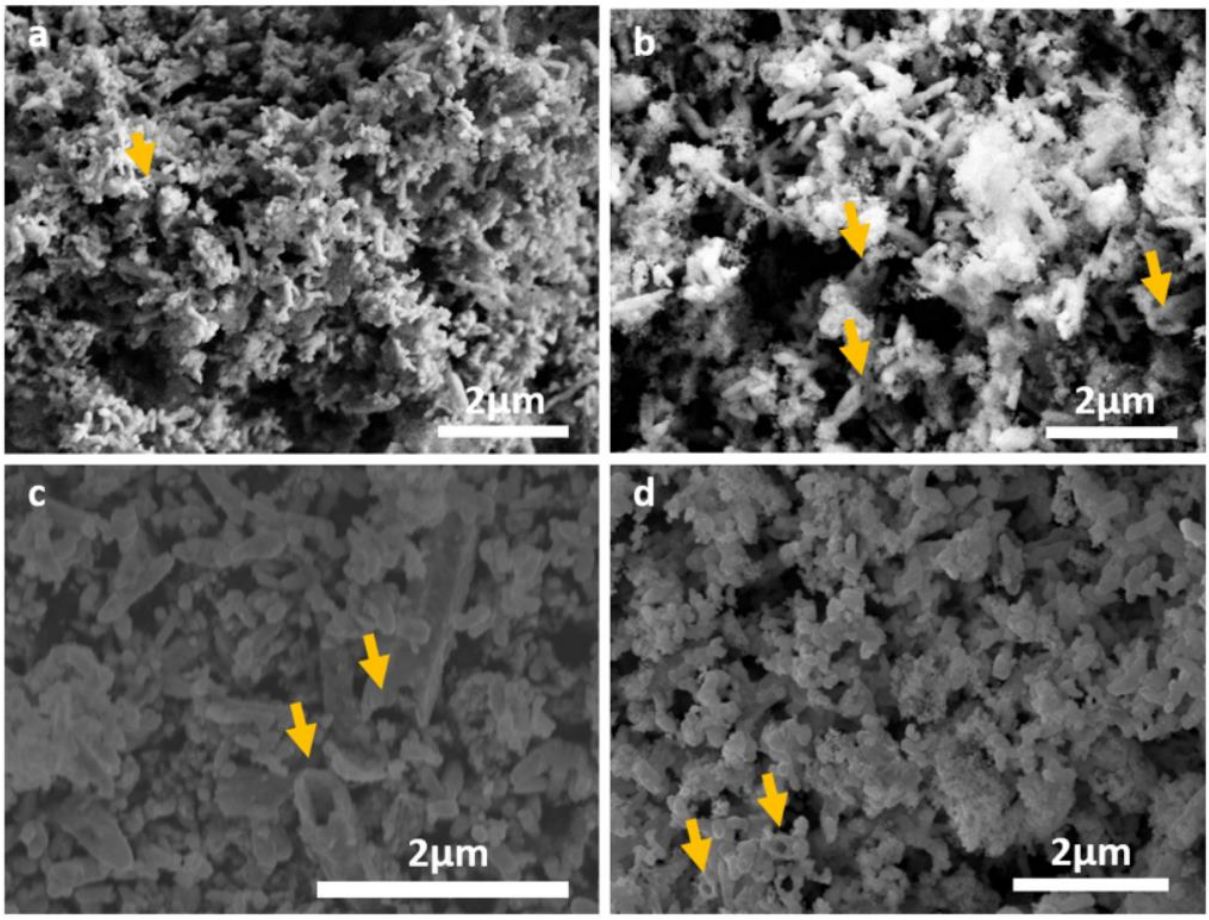

Figure-2.3.4. SEM images of Bi_2Te_3 nanoparticles with 80% nanotubes, synthesised according to the protocol 3.2, but in different batches: yellow arrows – open ends of tubes

II.3.3.b Application of surfactant during template formation (Protocol 3.3)

Bi_2Te_3 nanoparticles fully consisting of elongated particles (tubes and rods) are obtained with the help of additional surfactant – SDBS. As in a standard Te reduction procedure 3.36 g (84 mmol) of NaOH, 1.2 g (9.4 mmol) of Te and 1.45 g (38 mmol) of $NaBH_4$ are placed in 450 ml of degassed water and refluxed for 24h at 100°C under Ar atmosphere. The reduced Te-solution is cooled down under Ar-flow to room temperature. Upon reaching a required temperature, 0.16 g (0.45 mmol) SDBS is dissolved and Ar- and air-filled balloons are inserted into the solution and Te allowed to precipitate for 1 h. Due to the surfactant, formed Te templates are well stabilized in the solution, therefore form black suspension. To eliminate the oxygen introduced during precipitation, the suspension heated to boiling, then it is refluxed for 1h under Ar-flow. Ar flow is introduced only after the reflux started to avoid soaping/foaming. Then the suspension is cooled down under Ar atmosphere. Meanwhile, in a separate flask, as in a standard procedure, Bi-DDT complex is prepared in a separate flask by placing 25 ml (104

mmol) of 1-DDT and 2.01 g (6.37 mmol) of $BiCl_3$ are placed in 125 ml of degassed THF and stirred under Ar atmosphere for 24h until complete dissolution of the salt. The complex solution is then transferred via cannula to the main reaction flask with Te suspension. Reaction mixture is stirred and refluxed under inert atmosphere for 72 h. Obtained Bi_2Te_3 particles are filtered and washed by THF, water, EtOH and acetone repeatedly and finally dried.

As described in earlier sub-chapter, application of surfactant leads to the formation of high aspect ratio long Te rods. This change in template morphology leads to the change in the morphology of the final Bi_2Te_3 particles accordingly, resulting in long nanotubes with the length mainly from 1 µm up to 2 µm and diameter 50 nm – 80 nm. Small portion of shorter tubes also exists. Interestingly, diameter of the tubes remains relatively small despite the significant increase in the length, in contrast to the particles morphology of tubes obtained without SDBS. The surface of the particles is rough, but significantly smoother that earlier obtained Bi_2Te_3 particles surfaces. XRD diffraction pattern is in accordance with standard Bi_2Te_3 crystal structure with R3m-H space group (Figure-2.3.2 green line). The peaks are broader (zoomed insets of Figure-2.3.2) in comparison with Bi_2Te_3 samples prepared without additional surfactant (protocol 3.1 and 3.2) which suggests that the size of crystal domains is smaller. According to SEM images (Figure-2.3.5) the morphological composition of the obtained Bi_2Te_3 particles is 100% tubes corresponding to the template quality which is pure rods.

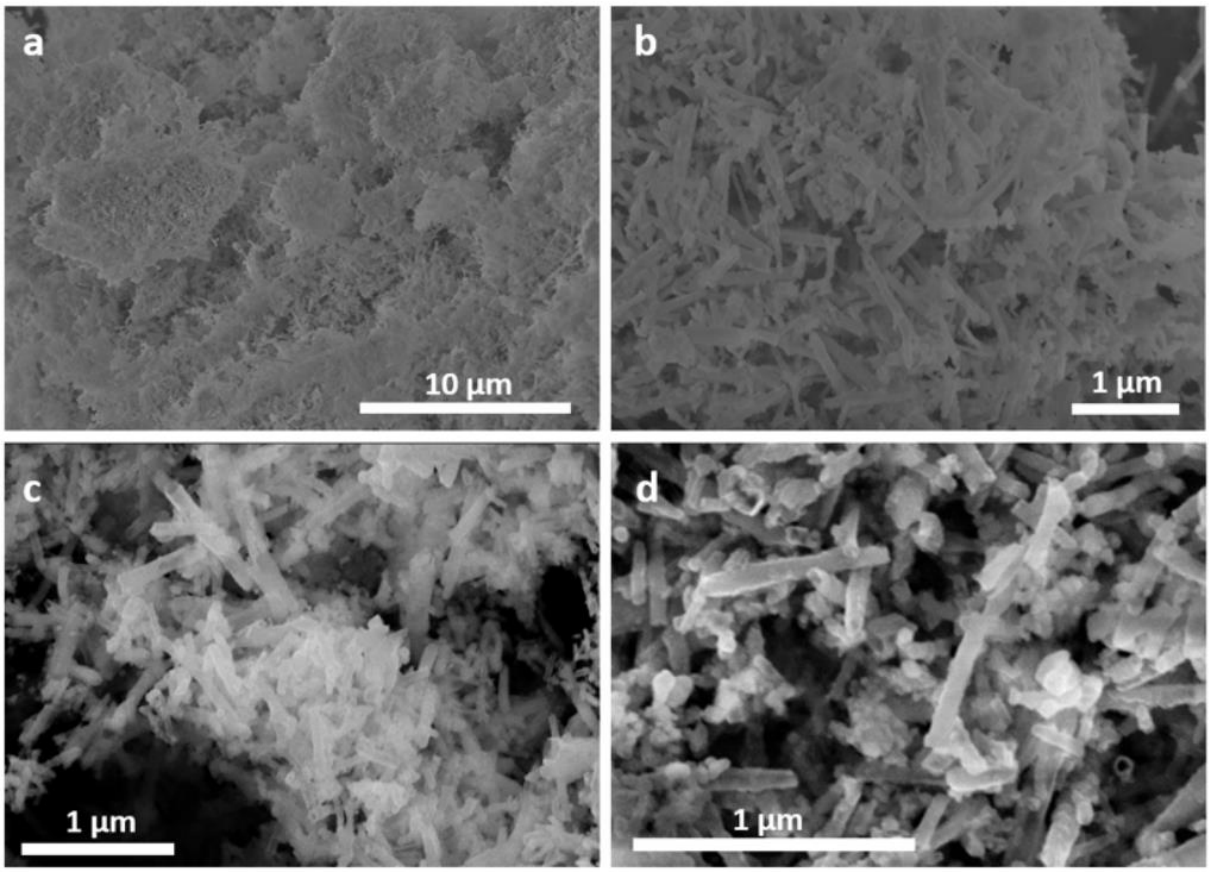

Figure-2.3.5 - SEM images of Bi_2Te_3 nanoparticles synthesised with SDBS during template formation

II.3.3.c Two-step synthesis process using preformed homogeneous rods (Protocol 3.4)

In two pot reaction, firstly Bi-DDT complex is prepared in a standard way by mixing 25 ml (104 mmol) of 1-DDT with 2.01 g (6.37 mmol) $BiCl_3$ in a THF for 24 h under inert atmosphere. Then, pre-prepared Te rods, are placed in a 450 ml of degassed water with dissolved 0.16 g (0.45 mmol) of SDBS in it. The suspension is formed by mixing it by sonication tip for 10 min with pulse 5 s on, 10 s off under an inert atmosphere. Then, Bi-DDT complex solution is introduced into the suspension via cannula and reaction mixture is refluxed for 72 h at 70°C under stirring and Ar atmosphere. Obtained particles are filtered, washed with THF, water, EtOH and acetone and dried.

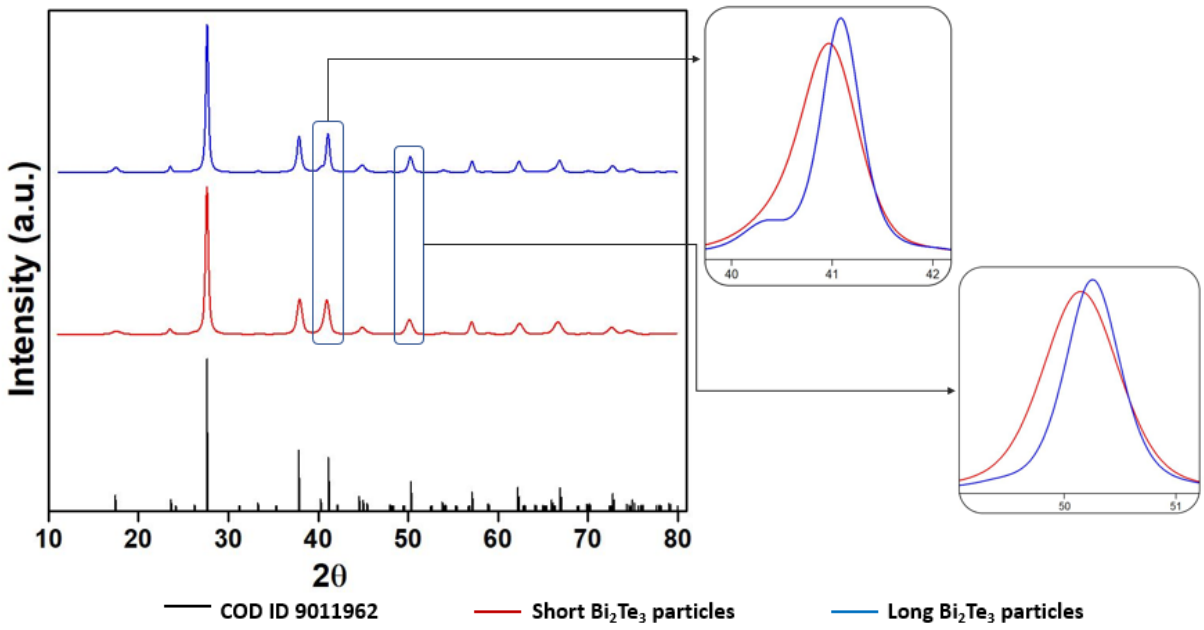

Figure-2.3.6. XRD spectra of Bi_2Te_3 nanoparticles synthesized according to two-step (pot) synthesis process in comparison with the standard from COD (COD ID 9011962)

To check the potential effect of chemicals added for Te precipitation step on the final Bi_2Te_3 synthesis step and to verify the possibility of obtaining different hollow morphologies from different Te templates morphologies, earlier described reaction of Bi_2Te_3 synthesis is carried out in two steps. The reaction is carried out on two types of pre-prepared Te templates: 1 – long rods prepared using SDBS (§II.2.3); 2 – homogeneous short rods (§II.2.4). Both reactions lead to formation of Bi_2Te_3 particles dimensionally corresponding to the used template. XRD diffraction of obtained particles yet corresponds to Bi_2Te_3 with space group R3m-H (Figure-2.3.6). The peaks are broader in short particles (Insets of Figure-2.3.6). As in the case of Bi_2Te_3 synthesis in one pot, it suggests that the longer particles have bigger crystalline domains. Interestingly, no open ends are observed on SEM observation of the particles (Figure-2.3.7 and Figure-2.3.8). The absence of residuals compounds boron, resulted from oxidation $NaBH_4$, simplifies the workup of the obtained Bi_2Te_3, obtaining clean powder after fewer washing steps than earlier.

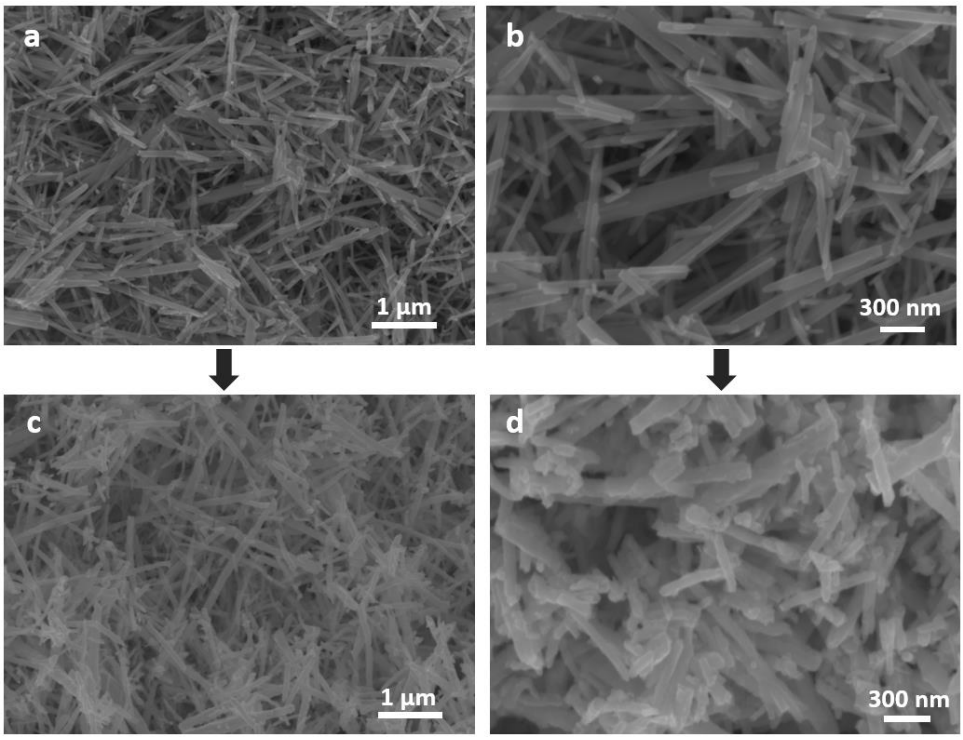

Figure-2.3.7. SEM images of nanoparticles: a, b – Te long rods; c, d – Bi_2Te_3 particles corresponding to the template

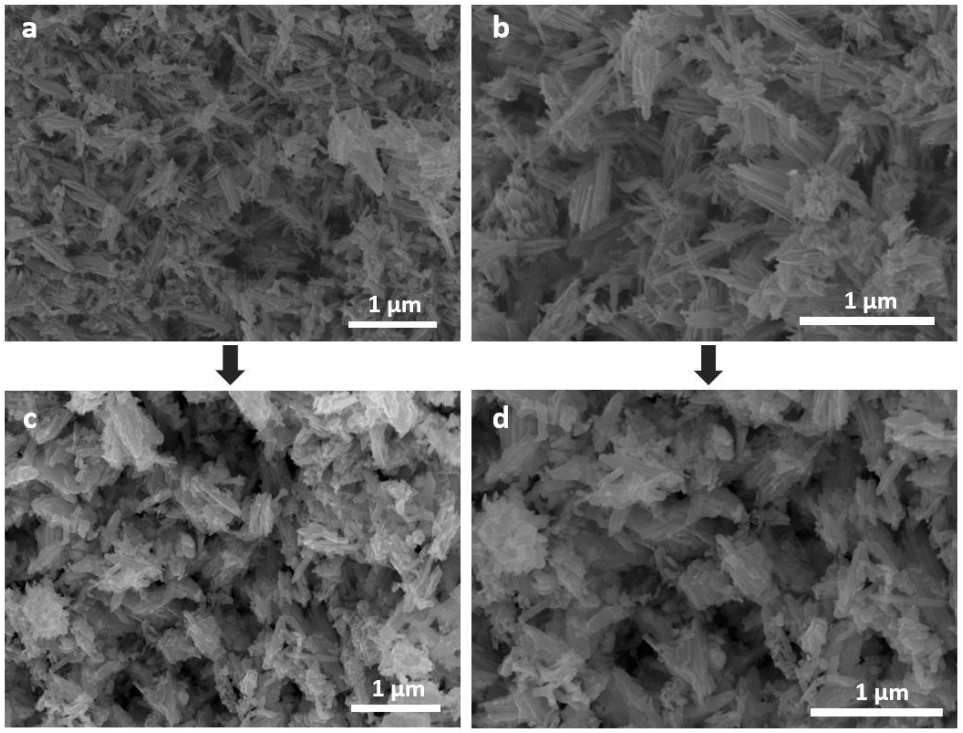

Figure-2.3.8. SEM images of nanoparticles synthesised: a, b – Te short rods; c, d – Bi_2Te_3 particles corresponding to the template

This two-step procedure also allowed to confirm the importance of using $Bi[DDT]_3$ as Bismuth source where thiol groups simultaneously acts as reductant. Since the NaBH4 is not added to the reaction solution in any prior steps the likeliness of residual BH4- to reduce Bi^{3+} to Bi(0) is eliminated which confirms the reductant role of thiol groups.

II.4 Thermoelectrical characterization

Thermoelectrical properties of three types of synthesized Bi_2Te_3 samples are characterized. First sample is designated as "R-30" and corresponds to the Bi_2Te_3 nanoparticles with 30% nanotube content synthesized following rolling up mechanism described in the section II.1 section of the chapter. Second sample is named "nK1-50" and corresponds to the Bi_2Te_3 nanoparticles with 50% nanotube content prepared by nanoscale Kirkendall diffusion in one pot in-situ templating method described in section II.3.2. The last sample designated as "nK2-100" corresponds to the Bi_2Te_3 nanoparticles with 100% nanotube content prepared by two-step templating method where reaction follows also nanoscale Kirkendall diffusion, but where template was prepared in advance as described in section II.3.3.c.

To characterize thermoelectrical properties of the obtained Bi_2Te_3 nanoparticles, the powders were sintered into pellets with d = 10 mm by spark plasma sintering (process and machine is described in appendix-x). Electrical resistivity and Seebeck coefficient were measured by ZEM3 (appendix-3) as a function of temperature. Thermal diffusivities of the samples were measured by laser flash analysis (appendix-5.1) at varying temperatures and the values were used to calculate the thermal conductivity according to the formula:

$$\kappa = D \cdot C_p \cdot \rho$$

where: D – thermal diffusivity [m^2/s]; C_p – specific heat capacity [J/kg·K]; ρ – density [kg/m^3]. Herein, C_p is estimated according to Dulong-Petit law with assumption that it does not vary with temperature, while density is measured by Archimedes method. All properties were measured perpendicularly to the sintering direction. Bi_2Te_3 is highly anisotropic due to its layered crystal structure. n-type Bi_2Te_3 exhibits 6-fold higher electrical conductivities along the ab plane in contrast with c-axis direction[164] (along the van der Waals gap between Te (1) – Te (1)). While the thermal conductivity is only two-fold higher.[165] Therefore, ZT is expected to have higher values along the ab plane. According to the HRTEM investigation of the sample R- the ab plane is located along the nanotubes wall, therefore, it is expected that nanotubes will have better TE performance along the tube walls direction. Sintering applies pressure on the powder which leads to the alignment of the tubes perpendicular to the sintering direction.

High surface area of nanoparticles led to failure of sintering step and subsequent loss of powders until conditions for stable sintering were set up (more air is released when the surface area is high, which leads to the increase of pressure beyond the capability of the sintering dye

to withhold, end eventually to explosion). Additionally, several samples were lost after successive sintering during the resistivity and Seebeck coefficient measurements. When a sample is set in ZEM3, to ensure stable positioning and a good thermal contact, the sample is sandwiched between cold and hot elements with certain pressure in a direction perpendicular to the sintering direction. Under these conditions due to the layered structure of the sample (nanotubes alignment), the sample is likely to break into non-uniform sheets at high temperatures. Due to these losses, thermoelectrical characterization of only three types of Bi_2Te_3 samples were carried out.

Figure-2.4.1 depicts the SEM images of the sintered Bi_2Te_3 samples (after ion polishing). Two of the depicted structures show porosity. The porosities in sample nK1-50 (a and b) probably result from both, the holes of the bigger tubes (arrows on b) and interparticle space due to non-dense packing. Meanwhile, the porosities in the second sample (c and d) are more likely due to a packing default. These porosities resulted in densities of the samples to be lower than the theoretical density of the bulk Bi_2Te_3 (7700 kg/m^3) and reached only 94% for nK1-50 and 95% for nK2-100 of the theoretical value.

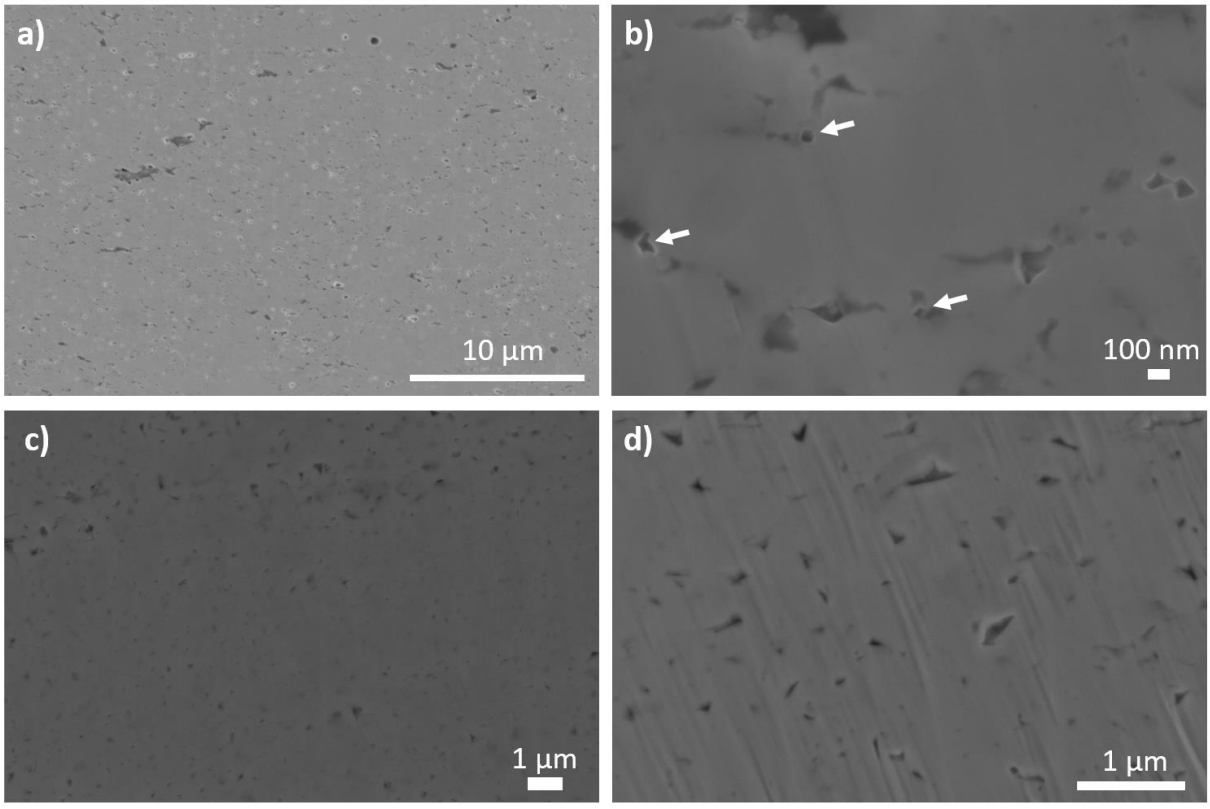

Figure-2.4.1. SEM images of Bi_2Te_3 samples after sintering: a and b nK1-50; c and d – nK2-100

Thermoelectrical properties of synthesized Bi_2Te_3 samples, presented on figure-2.4.2, corresponds to the behaviour of classical Bi_2Te_3.[166–169] Resistivities of the samples increases with temperature which correspond to the behaviour of degenerate semiconductor.[167,170,171] Seebeck coefficient has negative sign meaning that the conduction is n-type. Considering that the samples were not doped extrinsically charge carriers concentration arises from antisite point defects in the crystal structure of the Bi_2Te_3 (also known as intrinsic or self-doping).[166,171,172] Antisite point defects occurs when an atom in certain lattice point is replaced by the other atom from the lattice.[173] Higher electronegativity of Te results in positively charged Bi and negatively charged Te. Thus, in Bi_2Te_3, to produce electron charge carriers corresponding to n-type conduction by antisite defects, certain lattice points occupied by Bi have to be replaced by Te (Te_{Bi}). Stoichiometric Bi_2Te_3 demonstrates p-type conduction caused by intrinsic Bi_{Te} defects. Thus, since the samples demonstrate n-type conduction, it can be concluded that they are Te-rich. The values of Seebeck coefficients rise with temperature which is explained by increase of the charge carrier mobilities. However, for samples nK1-50 and nK2-100, upon further increase of the temperature the Seebeck coefficients drops after going through maximum (around 150°C). Such behaviour is explained by bipolar conduction, where both electrons and holes exist.[174] Increase of temperature leads to generation of minority charge carriers - holes, which eventually leads to decrease of the Seebeck coefficient, as an increase of the carrier concentration leads to decrease of the Seebeck coefficient.[166] The PF of samples with nK1-50 and nK2-100peaks due to the peak in Seebeck coefficient. Slight peaking in the PF of sample with 30% nanotubes (around 180°C) is explained by increase of inversely affecting resistivity, while directly proportional Seebeck coefficient is also increased with temperature. The peaking of the ZT of nK2-100 is more prominent due to the increasing thermal conductivity. ZT of R-30 ample gradually increases with temperature due to the increase of thermal conductivity. Due to earlier mentioned processing problems, thermal conductivity of nK1-50 was not measured, thus ZT was not calculated.

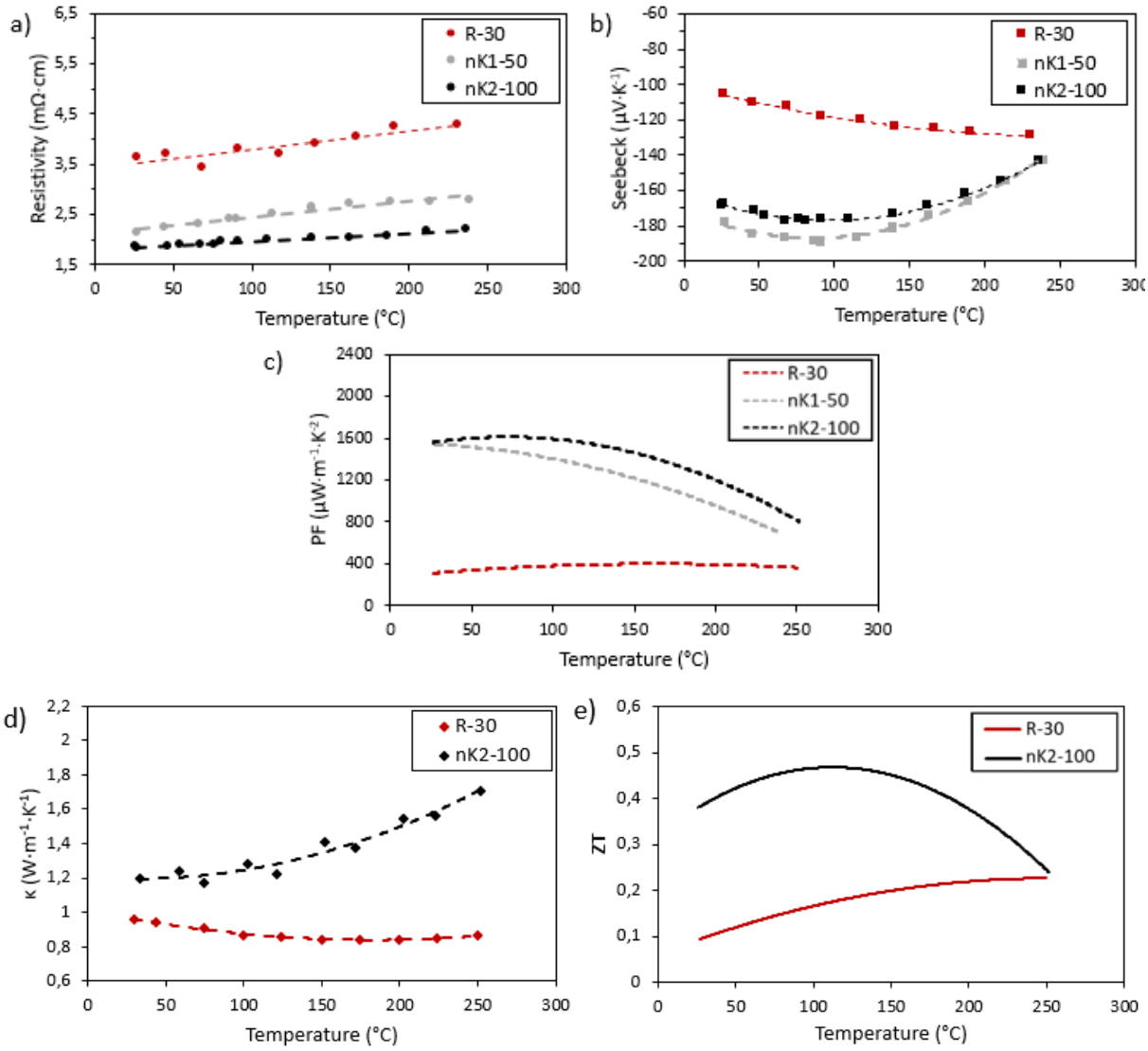

Figure-2.4.2. TE properties variation with temperature of Bi_2Te_3 samples: a) Electrical resistivity; b) Seebeck coefficient; c) Power factor; d) Thermal conductivity; e) ZT

The resistivities of the Bi_2Te_3 samples decreases with an increase of the nanotubes content. Three samples were prepared by different methods, which led to increase of both, crystallinity and nanotubes content. Both factors contribute to the decrease of the electrical resistivity. Seebeck coefficient values does not correlate with the nanotubes content. The carrier concentration and mobilities were not measured, which complicates the explanation of the Seebeck coefficient behaviour.

Comparison of thermal conductivities shows that the sample R-30 has considerably lower thermal conductivity. If the Lorenz constant is assumed to be $1.5 \cdot 10^{-8}$ [V^2/K^2] as usually used in the literature for near-degenerate and degenerate semiconductors[167,175], then

Wiedemann-Franz law allows to calculate electronic contribution of samples from its resistivity values according to the formula:

$$\kappa_e = \frac{L \cdot T}{\rho}$$

where, κ_e – electron thermal conduction [$W/m^{-1} \cdot K^{-1}$], L – Lorenz constant; T – temperature [K]; ρ – electrical resistivity [Ω·m]. Remembering that thermal conductivity is a sum of electron and lattice thermal conductivities, the lattice thermal conductivities can be easily calculated by subtraction. The results of the calculations shown in the Figure-2.4.3a. Both electron thermal conductivity and lattice thermal conductivities of the nK2-100 sample are higher, which explains considerably high total thermal conductivity. Out of plane thermal conductivity of the R-30 sample was also measured and compared with in-plane thermal conductivity on the Figure-2.4.3b. As theoretically predicted, the out-of-plane thermal conductivity is two times less than in-plane value. This allows to evidence the influence of alignment of tubes during sintering on thermoelectrical properties of the samples.

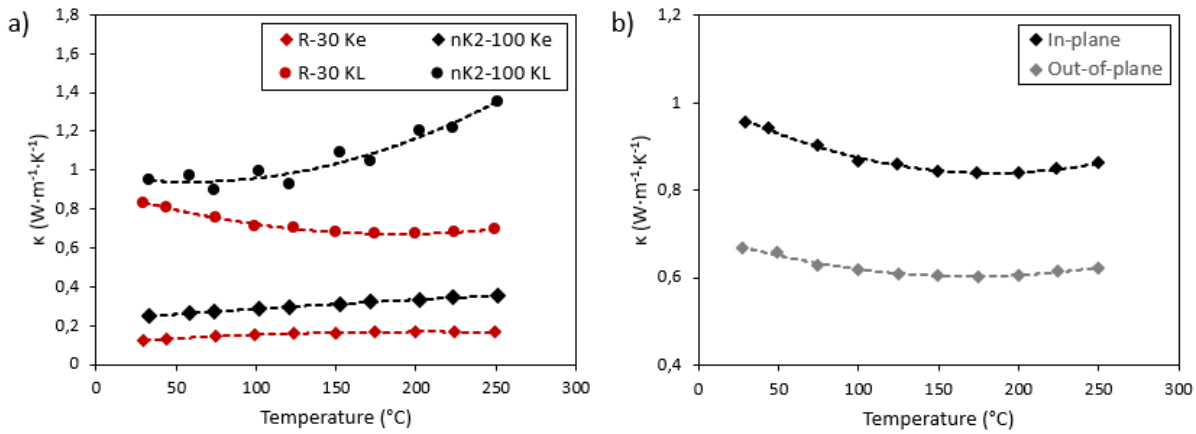

Figure-2.4.3: a) Electron and lattice thermal conductivities of Bi_2Te_3 samples R-30 and nK2-100; b) in-plane and out-of-plane thermal conductivities of R-30

In spite the low thermal conductivity sampler-30, due to its high electrical resistivity and low Seebeck coefficient, it demonstrates lowest PF and ZT with PF_{max} = 405 μW/m·K^2 and ZT_{max} = 0.23. nK2-100 demonstrates PF_{max} = 1650 μW/m·K^2 and ZT_{max} = 0.49. In spite the higher Seebeck coefficient, the PF of nK1-50 is lower than for nK2-100and show PF_{max} = 1530 μW/m·K^2. Low ZT values of prepared samples mainly results of the relatively high electrical resistivities which are 3-4 times lower for the tested samples (0.5 versus 2 mΩ·cm)[174,176,177] [51,53,54] in contrast with state-of-the-art Bismuth telluride, while Seebeck coefficient values are quite competitive (180 μV/K versus 150-200 μV/K). In spite achievement of reduction of thermal conductivities with nano-structuring, the values remain higher in comparison with state

of the are materials where lower κ is obtained by extrinsic doping (by Sb). Therefore, higher thermal conductivities further decrease the ZT. Yet, for pure Bi_2Te_3 without extrinsic doping the ZT of 0.49 is quite competitive.

II Conclusion

In this chapter Bi_2Te_3 nanoparticles with different nanotubes contents were synthesized by 1-DDT assisted reflux synthesis method. Although the main step of the reaction between Bi and Te precursors proceeds under the same conditions, difference in the Te precursor state lead the particles to grow in two completely different mechanisms. When Te is in an ionic state prior the reaction with Bi source, reaction follows "rolling-up" mechanism and yields powder with 30% of nanotubes. When Te is in elemental state (0 charge), the reaction follows nanoscale Kirkendall diffusion mechanism, and yields powders with different content of nanotubes, depending on the morphology of the Te particles. Thus, when the quality of Te template is improved by adjusting the re-crystallization (precipitation) condition of Te^{2-} to Te^0 or by application of surfactant, the content of nanotubes rises from 50% to 80%, and finally reaches 100%. The aspect ratio of the nanotubes also can be varied by varying the template characteristics.

The uniqueness of this method, apart from allowing to vary the morphological content of the powder, is mild reaction conditions. All Bi_2Te_3 nanoparticles are obtained at 70°C under reflux and water is used as a major solvent. The reaction is easily scalable, as produces morphologically same powder at ranging the scale from 575 ml up to 1.8 L in the case of rolling up mechanism, and from 57 ml up to 575 ml in the case of Kirkendall diffusion mechanism. Despite the difference in the mechanisms, this method always produces pure Bi_2Te_3 phase with rhombohedral arrangement of atoms in the crystal lattice according to XRD patterns. The succeeded attempt to carry out the reaction with pre-prepared templates and closed ends of the obtained nanotubes opens up a possibility to transfer this method into different morphologies as spheres.

Thermoelectrical characterization of selected samples demonstrates competitive n-type Seebeck coefficients around 180 μV/K. Although certain improvement in reduction of thermal conductivity is achieved, yet further improvement is needed to compete with state-of-the-are materials. The main aspect restraining the thermoelectric performance of the tested samples are low electrical conductivities. Recalling that the sintered samples were porous, the first way to enhance their properties would be to improve the sintering conditions to decrease or eliminates the pores. Yet, considering the absence of extrinsic doping and relatively mild reaction conditions, the ZT of 0.49 is a competitive value. Presented characterization of transport

properties represents the feature of the bulk samples affected by their structure (arrangement of particles), rather than the single particles.

Chapter III – Preparation & Characterization of Bi_2Te_3/epoxy resin hybrid composites

III Introduction

Percolation of the Bi_2Te_3 nanoparticles is crucial since the matrix has isolating nature and TE process will take place only through the Bi_2Te_3 network. Disruption of continuity of the network would lead to the loss of the TE properties of the material. Epoxy matrix is selected due to number of reasons. Firstly, low viscosity of uncured epoxy resin mixture allows its good miscibility with filler and its impregnation in all cavities in the network. Being a thermoset, after curing, epoxy resin insures stability of the structure even at elevated temperatures. Epoxy resin has good chemical, thermal and mechanical resistivity. Flexibility of the epoxy resin, as well as of the final hybrid composite can be easily varied by changing the curing agent, while processing conditions can be easily adjusted to selected system. Low viscosity of the uncured epoxy resin mixture allows easy processability in deferent shapes.

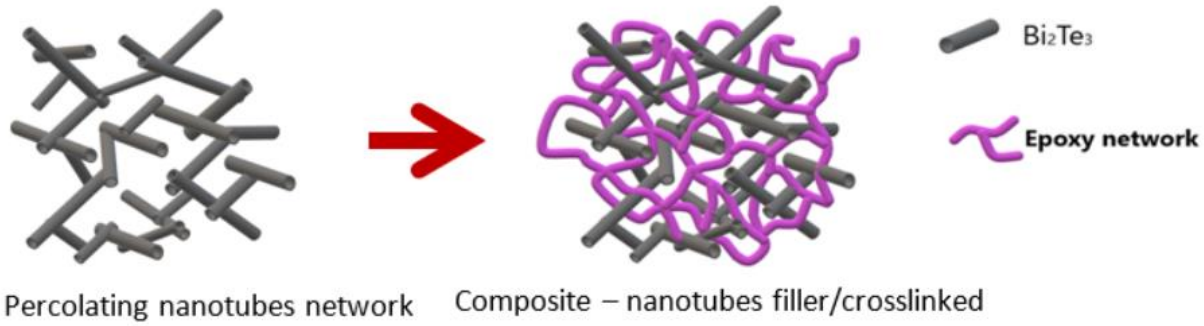

Figure-3. Schematic representation of the Bi_2Te_3 nanotubes/epoxy hybrid structure

The aim of Chapter 3 is to establish a method to prepare Bi_2Te_3/epoxy resin composite with segregated filler network as depicted in Figure-3 for thermoelectric application. The value is to use processability of the resin to form continuous structure from Bi_2Te_3 nanoparticles avoiding high energy consuming and costly methods as sintering. Epoxy resin is electrically insulating, therefore, considering the low aspect ratio of semiconductor particles, the challenge of this work is to reach percolation of the Bi_2Te_3 filler to obtain TE active composite. So far, only thin film composites of Bi_2Te_3 nanoparticles with an insulating matrix were reported, while current work aims to prepare bulk composite.

Bi_2Te_3/epoxy resin composites were attempted to be prepared by two mixing methods – manual mixing and speed mixing; and by infusion method. Composite preparation experiments were carried out along with improvement of the Bi_2Te_3 nanotube content. Therefore, Bi_2Te_3 nanoparticles with different morphological content were used at different stages of the composite preparation. Due to limited amount of the filler only few composites were prepared, especially with mixing methods which require high quantity of the mixing components. Yet, valuable conclusions were obtained. Among employed methods infusion is the most notable one as it is first time it was employed for Bi_2Te_3 nanoparticles and final composite showed highest potential.

III. 1. Composite preparation by mixing

III.1.1 Manual mixing

To prepare composite via manual mixing DGEBA/IPDA resin mixture (Appendix-7) (T_g = 150°C) was selected as a matrix. As a filler Bi_2Te_3 particles R-30 with 30% of nanotubes were used. In a general procedure stoichiometric ratio of DGEBA (20.49 g, 53.8 mmol) and IPDA (4.67 g, 27.4 mmol) were mixed with 10w% (2.51 g, 3.13 mmol) of Bi_2Te_3 by spatula for 5 min. The mixture was degassed in a vacuum line for 30 min while being stirred with magnetic stirrer. After the first step of the degassing aliquots were taken for DSC and rheology analysis and the rest of the mixture was transferred into silicon moulds (2.5 cm, 5 cm) and degassed for another 30 min under slow vacuum. Degassed mixture was then cured at 100°C for 30 min and post cured at 160°C for 40 minutes according to the selected curing conditions for pure DGEBA/IPDA resin system.

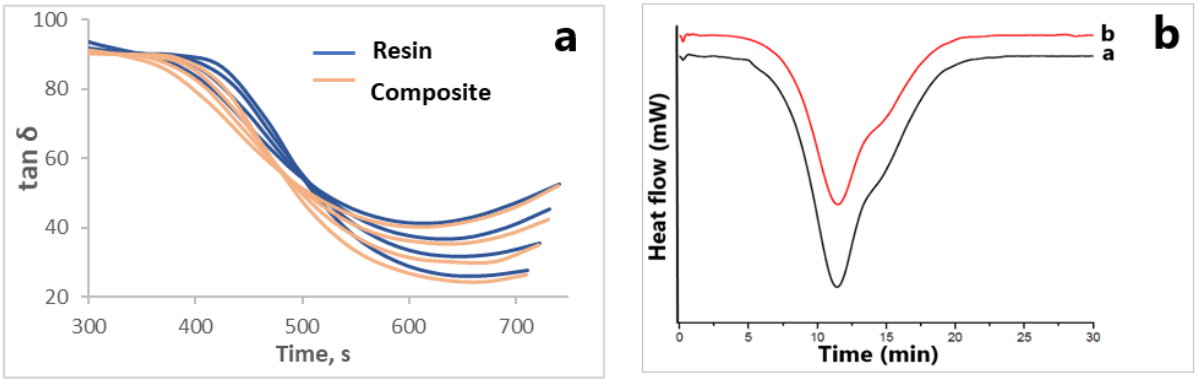

Figure-3.1.1. a) rheograms of pure DGEBA/IPDA resin – blue lines, and composite with 10w% Bi_2Te_3 – orange lines measured at 100°C and multifrequency mode (frequencies 5 rad/s, 10 rad/s, 23 rad/s, 50 rad/s); b) DSC traces of a – pure DGEBA/IPDA resin and b - composite with 10w% Bi_2Te_3 (heating ramp 10°C/min, T_0 – 0°c, T_{max} – 300°C)

When homogenous mixing is ensured and suitable ratio of the resin to hardener is selected, the network density (extent of the cross-lining reaction) depends on the curing profile – temperature and duration of the curing. Thus, to ensure the maximum curing density the effect of the filler addition on the curing kinetics and rheology evolution is important, as changes to the curing profile should be introduced depending on the impact of the filler. One of the important characteristics of crosslinking reaction is gelation. Gelation is an abrupt increase of the viscosity and change of a state from a liquid-like to solid-like.[178] Structurally it corresponds to the formation of a giant macromolecule which percolates throughout the system. Conversion

or time at which gelation takes place is known as gelation point and determination of gelation point is important for selection of processing conditions. In our case, gelation arrests the structure of the composite, restraining the movement of filler. One of the methods to identify the gelation point is evaluation of the curing rheology at multi-frequency mode. Depending of the applied frequency, the loss factor tan δ (G'/G'') evolves differently, but at gelation point the rheological properties of the resin are independent of the frequency. This marked with intersection of all tan δ (t) curves at this point. Figure-3.1.1a depicts the evolution of tan δ of pure resin and composite, measured at isothermal (100°C), multi-frequency mode. According to the measurements the gelation point of the pure resin and composite is 500 s and 475 s accordingly. Figure-3.1.1b depicts the DSC trace of the curing of the resin (trace a) and composite (trace b) and show almost identical curing profile. Close gelation points and similar curing kinetics allows to conclude that no changes are required to be introduced for the curing profile of the resin when it is loaded with Bi_2Te_3 filler since it does not impact significantly the network curing kinetics.

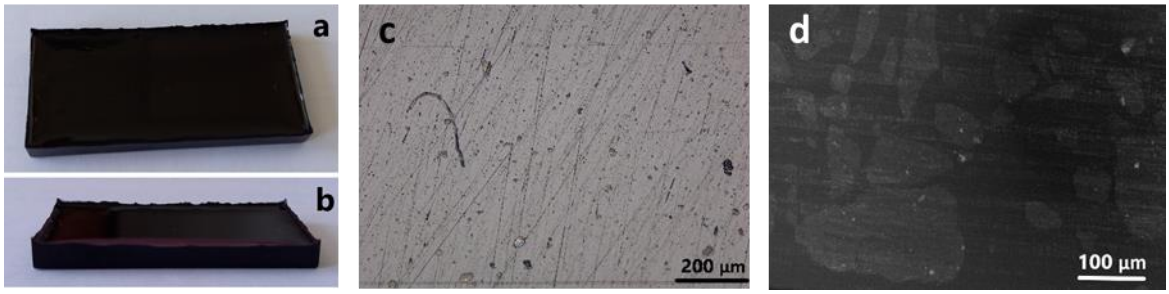

Figure-3.1.2. a) top and b) side images c) optical microscope and d) SEM images of the cross section of the DGEBA/IPDA/Bi_2Te_3 composite

Distribution of the filler in the matrix was evaluated by optical microscope and SEM (Figure-3.1.2c and d). Complete black coloration of the composite (Figure-3.1.2a and b) suggests homogeneous distribution of the particles throughout the resin. However, unevenly distributed big aggregates were also observed on SEM images (Figure-3.1.2d), with the size ranging from 20 µm up to 300 µm. Mapping of the cross section along the vertical direction of the sample shows no aggregates on the upper region, less and smaller aggregates in the middle, big and denser packed aggregates on the bottom of the composite. It is very likely that particles sedimented at the beginning of the curing, when the viscosity of the resin drops dramatically due to the temperature increase and allows particles settle easily by gravitation. Random size and shapes of the aggregates suggests that they did not form during the mixing, but rather existed in the powder state before the mixing. In general, it can be concluded that the Bi_2Te_3 filler is evenly distributed in the matrix and partly unevenly aggregated. Optical microscope

images of bigger area (Figure-3.1.2c) shows pores, meaning that degassing was not efficient. Electrical conductivity test showed high resistance of the material for current flow, which suggest that percolating network did not form. Probably reason is insufficient amount of the filler and its aggregation.

Several conclusions can be drawn from the above experiments:

- Addition of Bi_2Te_3 does not introduce considerable changes to the curing kinetics of the resin, therefore, in composite preparation the curing profile selected for pure resin can be used;
- Manual mixing does not provide sufficient distribution of the filler as part of it remained aggregated, which further settled in the bottom of the composite forming uneven morphology of the composite;
- Resin mixture probably does not suit to be used in composites with Bi_2Te_3 as composite had tiny pores even after long degassing steps.

Whether 10% of Bi_2Te_3 is sufficient for formation of the percolating network is not conclusive since it is not clear how the filler would be distributed if part of it did not aggregate. High amount of insulating epoxy resin did not allow to observe the distribution of the well distributed part of the filler at higher magnification.

III.1.2 - High speed rotational mixing (speed mixing)

High speed rotational mixing of composite components was carried out on speed mixer. Mixing in a speed mixer takes place by dual asymmetric centrifugation, where holder of the mixing container rotates clockwise, while the container itself rotates counter-clockwise around its vertical axis, providing centrifugations in opposite directions.[179] Thus, the shear caused by two rotational movements of the mixture in opposite directions mixes the components. Speed mixing is proven to be effective and often used to mix pure resin components as well as filler/matrix systems. It also efficiently removes bubbles, but not completely. Small containers (12 ml) available for speed mixer makes it possible to efficiently mix small quantities. This allowed to prepare composite with high filler loading, considering the limited amount of the filler particles. High filler loaded composite obtained by adding small amount of the matrix, which led to overall small volume of the composite mixture. Mixing small quantities efficiently is challenging for many other mixing techniques.

To prepare composite via speed mixing RIMR 135/RIMH 137 resin mixture (Appendix-7) (Tg = 80°C) was used as a matrix. Bi_2Te_3 particles nK1-50 with 50% nanotubes content prepared by nanoscale Kirkendall diffusion in one pot was used as a filler. For preparation of composite with speed mixing the resin system has been changed to RIMR-135/RIMR-137, because micro-sized pores remained in the composite with previously used DGEBA/IPDA resin mixture even after prolonged degassing. RIMR-135 is a mixture of epoxy resins Bisphenol A-Co-epichlorohydrin and 1.6-bis(2.3-epoxyperoxy) hexane in a ratio 70-90% to 15-20%. The corresponding hardener RIMH-137 advised by the producer (Epicure) is a mixture of two common hardeners poly(oxopropylene)diamine and IPDA in a ratio 50-75% to 35-50%. The resin mixture prepared from these two components provides better curing and less gas emission at mixing and widely used both in laboratory and industrial scale for hybrid composite preparation.

In a general procedure the mixture of RIMR-135 resin (0.48 g) with RIMH-137 hardener (0.12 g) in a mass ratio 100 to 30 (stoichiometric ratio recommended by manufacturer) was loaded with 75 w% (1.8 g, 2.25 mmol) Bi_2Te_3 nanoparticles nK1-50. The mixture was briefly homogenized by spatula, then mixed by speed mixer at 3000 rpm for 3 min. Homogenous mixture was then degassed at room temperature for 10 min, transferred into a Teflon mould with d = 15 mm and l = 5 mm, degassed again in mould at 60°C for another 10 min the cured at 80°C for 2 h.

The Bi_2Te_3 filler ratio was selected to be 75 w% as it was maximum possible loading to prepare the composite by speed mixing. Bi_2Te_3 filler has nanosized morphology which creates big surface area. Increasing further the filler amount, while keeping the matrix amount constant, did not allow complete wetting of the all filler particles by resin. The mixture of the resin and filler is required to be preliminarily homogenized by manual mixing prior speed mixing. Considering this requirement, maximum loading amount from empirical study was identified to be 75 w%. Selected amount of the filler was placed in a container and resin mixture added on it starting from 5% in an increasing order by increment of 5 until all the filler particles surface was wetted.

High level of filler loading led to highly viscous RIMR-135/RUMH-137-Bi_2Te_3 mixtures. Therefore, degassing carried out at 50°C in order reduce the resin viscosity and facilitate degassing. In spite of the elevated temperature, high viscosity of the mixture (before curing) did not allow complete degassing, which lead to a porous composite with rough surface. The cured composite had dimensions d = 15 mm, and the h = 4.5 mm. Figure-3.1.3 displays

SEM images of the cross-sectional area of the composite after ion beam polishing. Figure-3.1.3a represents the general morphology of the composite. Zoomed image on Figure-3.1.3b shows A-particles pointed with white arrow which represent Bi_2Te_3 nanotubes cross-sectioned perpendicular to its length, while B-particles pointed with red arrows represent tubes cross-sectioned along its length. Frequent encounter of both types indicate that tubes are randomly oriented in the matrix, without apparent orientation, thus composite can be considered isotropic. Pieces of the sample with no apparent big pores were cut and its electrical conductivity was measured both by multimeter and ZEM 3. However, the composite surprisingly showed resin like resistance, which mean percolation was not obtained throughout the whole sample. It is evident from Figure-3.1.3c, where a considerable "resin only" area between filler particles is indicated by a green arrow. Additionally, green arrows on Figure-3.1.3d show considerably continuous aggregations of epoxy resin, which would highly contribute to the destruction of percolation.

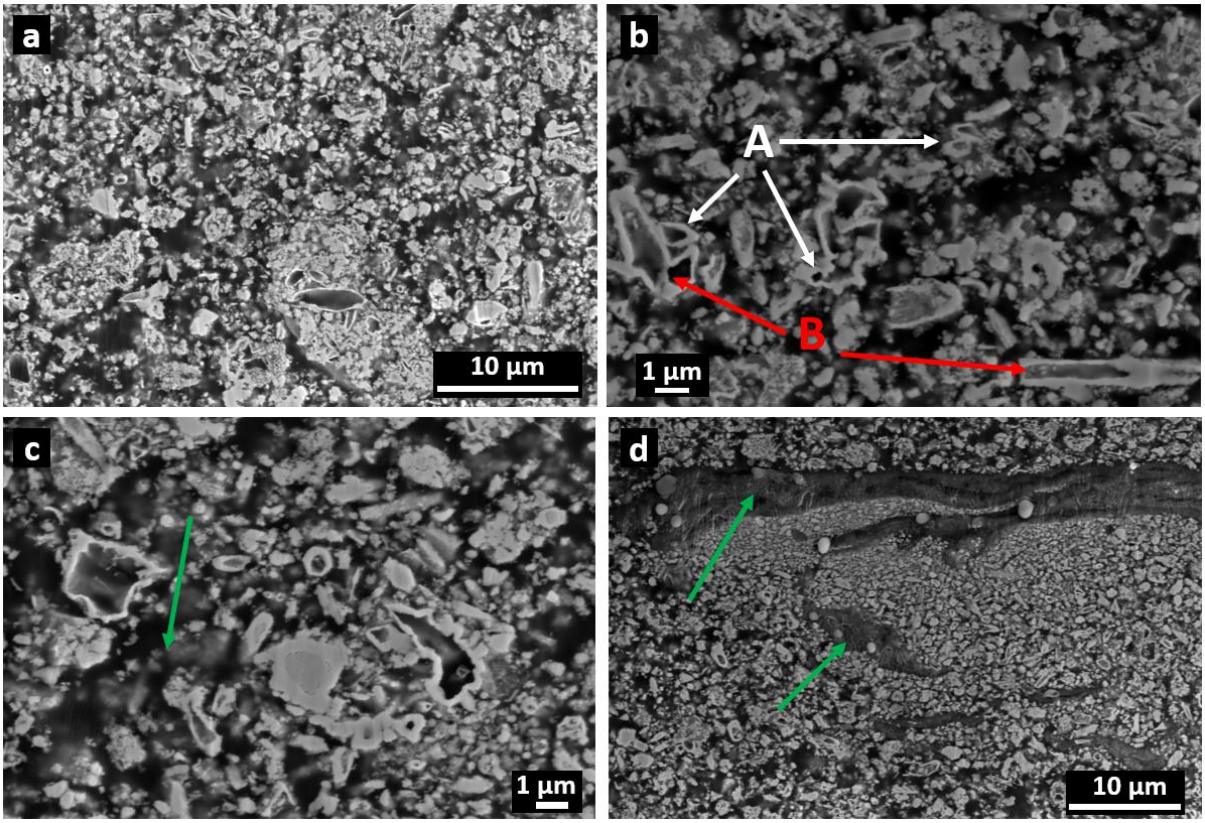

Figure-3.1.3 – SEM images of Bi_2Te_3/epoxy resin composite prepared by speed mixing: a – general morphology; b – Bi_2Te_3 tubes cut: A – across the tube length; B – along the tube length; c – green arrow indicating resin reach areas; d – arrows indicating continuous unloaded resin phases

As expected speed mixing provided relatively fine distribution of the filler particles in the matrix according to SEM images. However, big pure epoxy areas between filler particles and a few continuous agglomerations of the resin did not allow segregation of the Bi_2Te_3 network, which prevented the composite to be conductive.. Therefore, it can be concluded that speed mixing is not suited to prepare TE active composite from as synthesised Bi_2Te_3 sample nK1-50 content with epoxy resin. One could suggest addition of solvent to increase the wettability and improve pre-mixing and mixing of Bi_2Te_3 with resin. This tactic is usually applied to lower the viscosity and facilitate the mixing in epoxy resin mixtures. However, considering high viscosity of the Bi_2Te_3/epoxy resin, further complete removal of the solvent can be problematic. Trapped solvent deteriorate the properties of the composite. Therefore, as we did not succeed in obtaining conductive composites at maximum filler loading attainable for mixing methods, an alternative method has been experimented.

III.2 Composite preparation by infusion

The infusion method, earlier developed for CNT/epoxy thin films[180], was adopted for the first time for Bi_2Te_3 nanotube fillers. It relies on preparation of Bi_2Te_3 buckypapers and further infusion of it by resin and subsequent curing. So far only thin films of Bi_2Te_3/isolating matrix hybrids were reported[135,136,139], while our method allows to prepare bulk samples of any thickness. For the following experiments, Bi_2Te_3 with 50% nanotube content were used as a filler, while a resin mixture RIMR135/RIMH-137 was used a matrix. Additionally, ternary composites with addition of MWCNT (Nanocyl 7000) were prepared to explore possibility of reinforcing the Bi_2Te_3 buckypaper to improve its structural stability. CNT/epoxy composite was also prepared as comparative sample to understand CNTs contribution in the ternary composite.

III.2.1 Preparation of buckypapers (Bi_2Te_3, CNT, CNT/Bi_2Te_3)

Buckypapers were prepared by gradual filtration of dispersions of the corresponding nanoparticles in methanol. To prepare the dispersions corresponding amount type of nanoparticles (Table-3.2.1) and 50 ml of MeOH were placed in a 100 ml RB flask and mixed by sonicating tip (Bandelin-Sonopuls – probe KE76). The amplitude of the sonication was set to 30%, with pulse 15 s on, 5 s off, duration 30 min. The dispersion gradually filtered on a small Buchner funnel under vacuum. The funnel (Figure-3.2.1) was fitted with a Teflon mould with an inner diameter of 15 mm and an outer diameter corresponding to the inner diameter of the funnel. Inner circle surface of Buchner funnel was fitted with two layers of cellulose filter papers (pore size 0.22 μm and 2 μm) followed by two layers of PTFE membrane (0.1 μm). The mould was tightly attached to the funnel covered by membranes through plasticine to avoid the waste of the vacuum power around the mould, and secure high pressure only in the intended inner circle of the mould. Filtration carried out slowly drop-by-drop, but continuously till the end. BP forming in the mould was periodically pressed. Dispersion was re-sonicated every 60 minutes for 5 mins to maintain the homogeneity of the dispersion and BP. After completion of the filtration the BP was pressed by filtering over it additional 1-2 ml of pure MeOH. BP is then carefully removed from the mould, placed on a petri dish and residual solvent was evaporated by drying in an oven at 50°C for 18 h.

Table-3.2.1 Amounts of nanoparticles for preparation of dispersions

Corresponding composite name	Amount of Bi_2Te_3 (g)	Amount of CNT (mg)
Bi_2Te_3/epoxy resin	2.7	-
CNT/epoxy resin	-	300
10V%CNT- Bi_2Te_3/epoxy resin	2.7	30
20V%CNT- Bi_2Te_3/epoxy resin	2.5	68

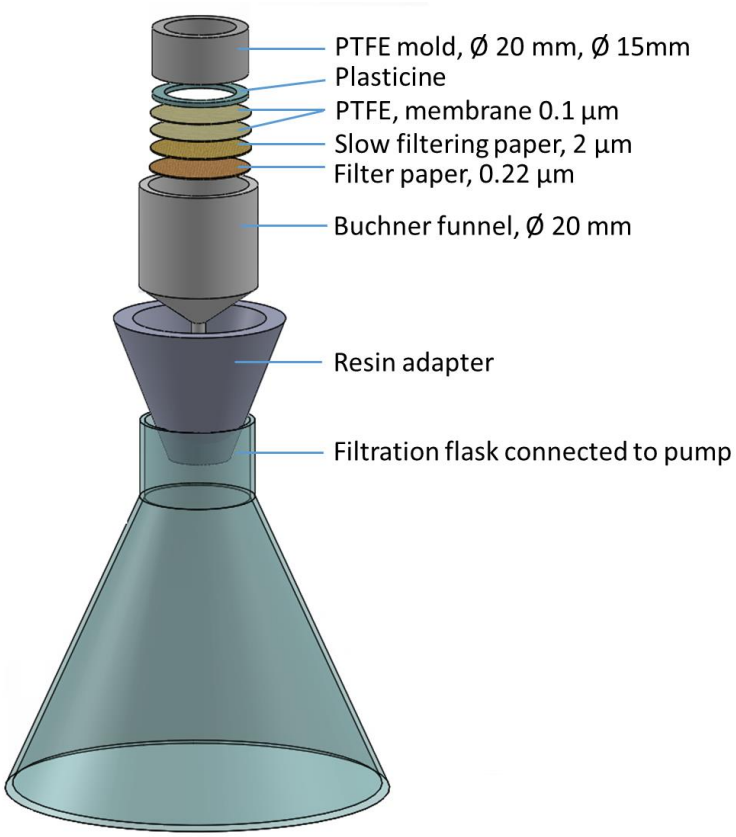

Figure-3.2.1 – Filtration set-up to prepare BPs

BPs were prepared by filtration of the nanoparticles suspension on a set up depicted on Figure-3.2.1. Several layers of the filter papers with different pore sizes were used because certain portion of the Bi_2Te_3 consist of small nanoparticles which escape from filter papers as the last has higher pore size than the NP size. However, even with using several layers, at the beginning of the filtration certain amount of the NP escapes the filter paper until certain layers of NP forms on top of the filter paper and act as additional membrane. At the early stages the dispersion was filtered by portions of 0.5 ml, but after formation of the certain thickness of filtered nanoparticles residue layers which slowed down the filtration, the suspension was added dropwise. Disruption of suspension supply leads to cracks on forming BP due to negative

pressure. Therefore, filtration must be carried out continuously and meticulously. Forming BP was periodically pressed, which prevented formation of cracks, facilitated denser packing and decreased the shrinkage in the case of CNT BP. Filtration speed decreases with an increase of the BP thickness. After required amount of the suspension is filtered, the BP pressed further by filtering through the BP additional amount of pure solvent. Then BP carefully removed from the filtration set-up to flat surface and dried at 50°C for 18 h.

Bi_2TE_3 BP (Figure-3.2.3a) is very fragile, thus requires careful handling, both before and after drying. This is explained by the fact that only 50% of used Bi_2Te_3 nanoparticles were elongated, while the rest is small isotropic particles. Additionally, the length of the tubes is considerably shorter than CNTs which is usually used to prepare BPs. No shrinkage was observed after drying. BP had d = 15 mm, l = 3 – 3.5 mm, which allowed to estimate the density to 2.6 g/cm^3 ± 15%, which is three time less than the density of bulk Bi_2Te_3 (7.7 g/cm^3). It indicates that the structure is porous, thus suitable for infusion.

CNT BP is more facile to prepare and mechanically quite stable both before and after drying, owing to long and non-rigid structure of the tubes which easily entangle, thus form stable 3D structures. CNT BP considerably shrinks after drying, therefore to obtain at least d = 15 mm BP and composite, CNT BP were prepared directly in the funnel without application of additional Teflon mould. Thus, CNT BP prepared in a funnel with inner diameter of 20 mm had d = 17 mm after drying. Interestingly, increase of the pressing frequency during the filtration decreases the shrinkage. Density of CNT BP is estimated to be 0.26 g/cm^3.

Preparation of CNT/Bi_2TE_3 BPs were similar to the preparation of pure Bi_2Te_3 BP because of the higher content of the last component. The ratio was selected in a volumetric percent as, due to low density of the CNT it is added in mg scale. Conversion of volume to mass to calculate the powders amount to prepare suspension was carried out using the estimated densities of Bi_2Te_3 BP and CNT BP as indicated above, rather than using bulk densities. 10 V% CNT-Bi_2Te_3 BP showed brittleness similar to the pure Bi_2Te_3 BP, while the sample with 20 V% CNT showed considerable mechanical stability. Despite the high amounts of CNT added, no noticeable shrinkage took place.

III.2.2 Composite preparation

Infusion was carried out in two steps – first proper infusion of the BP then removal of the excess resin. The infusion step is carried out under vacuum in a custom-made mould placed in a desiccator (Figure-3.2.2). Custom-made mould consisted of three parts – stainless-steel block with d = 50 mm and l = 60 mm; Teflon tubular mould with inner diameter corresponding to the diameter of the BPs (usually 15 mm), outer d = 25 mm and l = 20 mm; metallic top circular hole with d = 20 (not to block the hole in Teflon mould, but keep cover in through the thickness of the tube wall) attached to the block via screws placed surrounding the Teflon mould. The purpose of the top cover is to provide close contact between block and Teflon mould. A piece of Kapton foil is placed between block and Teflon mould then the top is tightly screwed. Assembled mould is preheated in an oven at 80°C for 2h, then BP is placed in the Teflon mould and the set placed in a desiccator with side valve and rubber sealed hole on the cover.

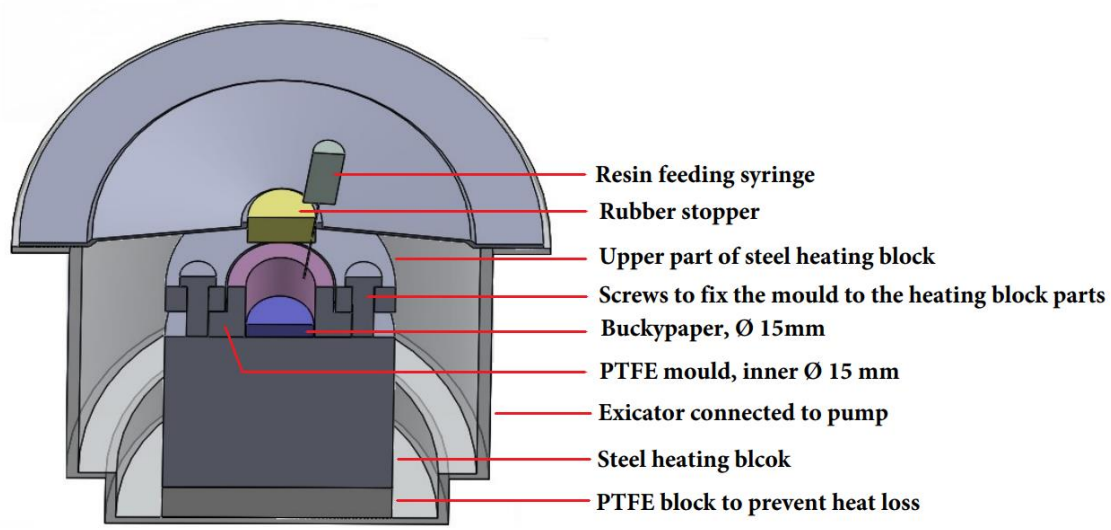

Figure-3.2.2 – Vacuum infusion set-up

Resin mixture was prepared by mixing RIM-135/RIMH-137 in a ratio 100/30 by speed mixer for 3 min at 3000 rpm and preheating at 50°C for 5 min. Preheated resin (approximately 2 ml) is filled in a syringe supplied with a long needle. The syringe is placed vertically on top of the desiccator cover by inserting the needle inside the dissector through the cover hole and closing the hole with rubber stop, while keeping the syringe outside. The needle is positioned on centre top of the BP at approximately 15 mm of its surface. All the joints were tightly sealed to avoid any loss of the pressure. Then vacuum was applied by pumping through the side valve. Pumping speed was adjusted to provide slow drop-by drop supply of the resin on the BP.

Approximately 0.75-1 ml of the resin is fed over 30 min. Infused composite allowed to degas for 30 min by removing the feed and increasing the pumping speed to maximum.

Slow dropwise supply of the resin and vacuum force along with the gravity are expected to facilitate fine infusion of the resin in enter-particle pores of the BPs. Exact amount of the fed resin is difficult to control; therefore, resin is fed till the surface of the BP is slightly covered with resin after saturation of the enter-particle pores, which required approximately 1 ml of the resin. The resin mixture was not degassed prior to supply; therefore, it is allowed to degas for 30 min after it was fed into the BP. It was more reasonable to degas the resin after it was infused, as epoxy resins are known to produce additional gasses after transfer. Curing of the resin right after the degassing step in the case of Bi_2Te_3/epoxy resin composite led to formation of electrically non-conducting composite, which means the excess resin added in uncontrolled matter interrupts the percolating network of the filler. Therefore, an excess resin removal step has been introduced. In contrast CNT/epoxy resin composite still maintained electrical conductivity even with extra epoxy amount. However, to keep the coherence between samples all the composites were prepared by two step infusion involving the removal step.

Removal of the excess resin is carried out in a way similar to the method known as vacuum assisted process, which in contrast is used to infuse the resin into substrate. The set up is depicted on Figure-3.2.3a. After the BP was infused with resin and degassed, the infusion mould is dismantled by unscrewing upper cover and removing it along with Teflon mould. The infused BP along with the Kapton foil underneath it are transferred on the metallic plate (150x150 mm) of the resin removal set-up depicted in Figure-3.2.3a which is constantly heated to 50°C. Sheets of peel-ply and fleece were placed on top of the composite. Peel-ply is to facilitate the removal of the set up from the composite, while fleece is placed to uptake the excess of the resin. Then *upper part of the set* (Figure-3.2.3b) is placed on top of the fleece in a close contact and attached to the metallic plate via thick all-sticky tape surrounding the composite. *The upper part* is a hand-made layered structure consisting of layers in a sequence Gore-Tex® – fleece ply 1 – straight sheet of metallic mesh – fleece ply 2 – small vacuum foil – big vacuum foil – connector valve. Gore-Tex® and small vacuum foil re-sealed together on sides via sticky tapes, sandwiching the intermediate layers, while the small and big vacuum foils where attached through the valve. After *upper part* is attached and sealed the bigger foil is also brought to close contact with the plate and attached to it via additional tacky tape surrounding the *upper set*. Once all closely sealed the vacuum is applied though from the top of the set via valve and removal of excess starts and lasts for 30 min.

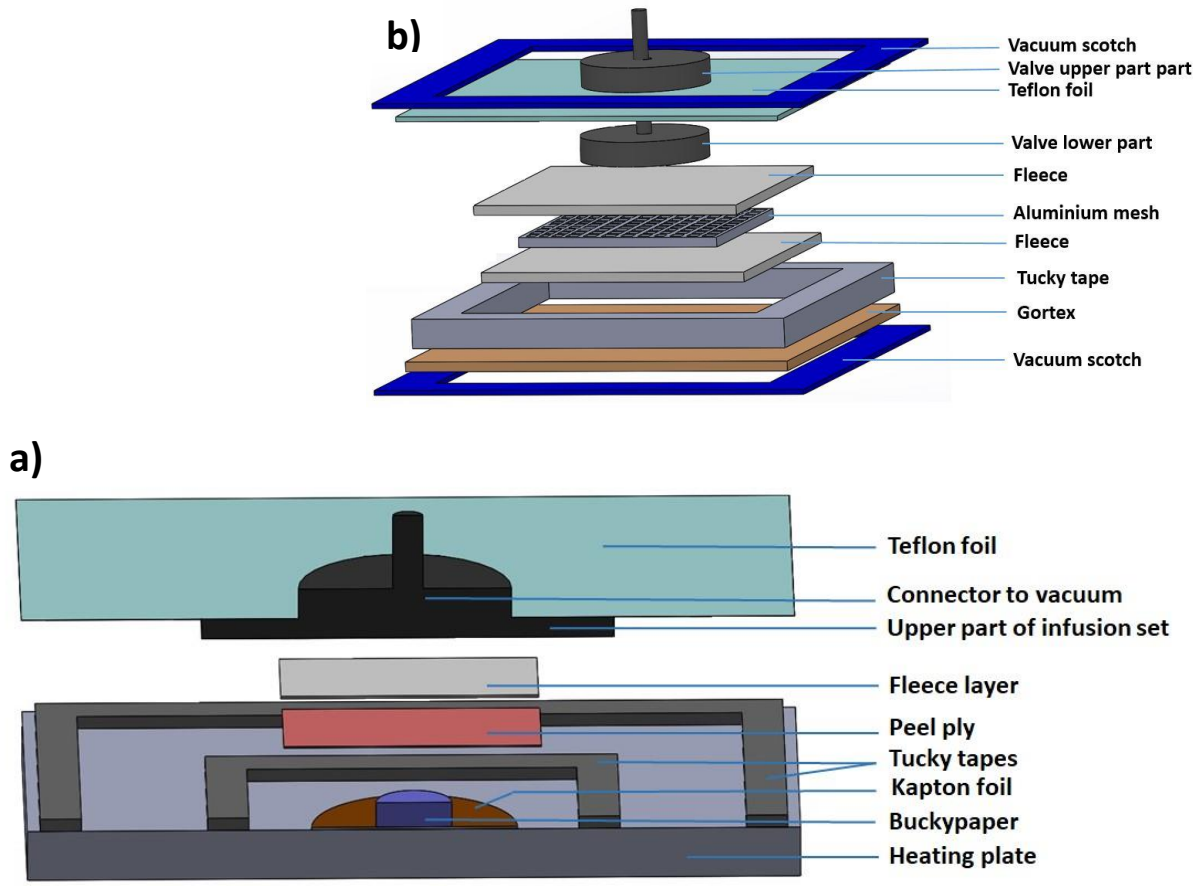

Figure-3.2.3 – Resin removal set up: a – general view; b – the detailed upper part structure

The excess resin is expected to be up-taken into fleece layer, otherwise called “bleeder”. The composite is then cured in the set up by increasing the temperature to 80°C and turning off the pump (but maintain close contact of the all parts of the set). Resin is cured for 2 h and the resulting solid composite is removed from the set. Then cured composite was removed from the set-up. Due to the adhesive properties of the resin the Kapton foil was adhered to the composite, while upper surface had meshed feature of the fleece ply (figure-3.2.4b). Therefore, the surfaces of the composite were polished off before further handling.

Figure-3.2.4: a - Bi_2Te_3 Buckypaper; b - Bi_2Te_3/epoxy resin after curing (before polishing); c - CNT/epoxy resin composite after polishing

Figure-3.2.5 depicts SEM images of the Bi_2Te_3/epoxy resin composites cross-section (perpendicular to the filtration direction). They show that particles are evenly spaced between each other. The space between particles are finely filled with epoxy resin, without visible pores. Observation of considerable amount of the holes, as a result of cross-sectioned nanotubes, allows to conclude that gradual filtration allows to the majority of the nanotubes align perpendicular to the filtration direction. Yet, the spacing between individual particles, filled with epoxy resin, is still considerable, ranging from several nanometres up to several hundreds of nanometres (Figure-3.2.5c yellow arrows).

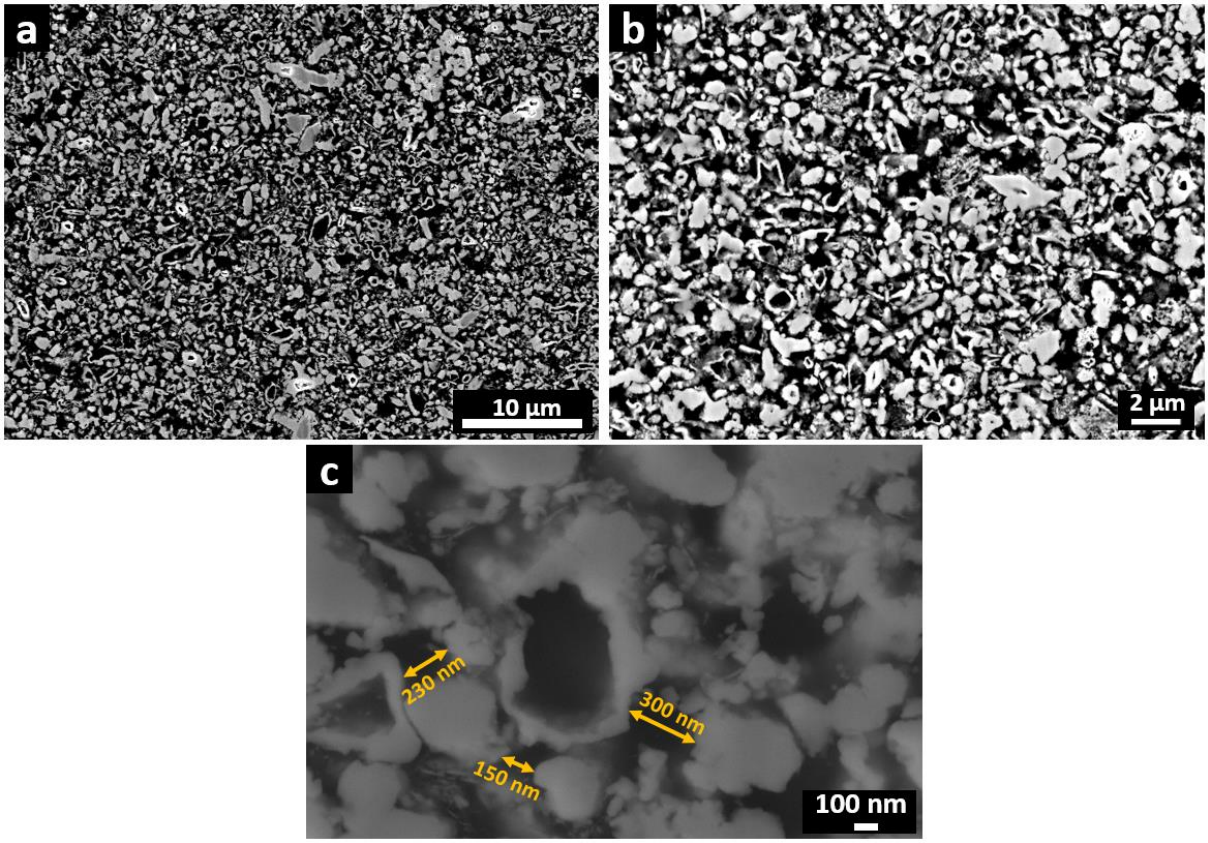

Figure-3.2.5: SEM images of Bi_2Te_3/epoxy resin composite prepared by infusion method

On Figure-3.2.6 SEM images of 20%CNT-Bi_2Te_3/epoxy resin composite cross section are displayed. In comparison with the sample without CNT, the composite seems much more porous. Bi_2Te_3 particles (brighter contrast on figure-3.2.6b and c) are interconnected with CNT-bundles (figure-3.2.6b), which in turn highly saturated with epoxy resin. Although in bundles, CNT is finely distributed in the composite and between Bi_2Te_3 particles and form continuous epoxy saturated CNT path. Observation of less holes from cross-sectioned Bi_2Te_3 nanotubes allows to conclude that the presence of CNT does not allow the Bi_2Te_3 nanoparticles align in one plane direction in contrast with pure Bi_2Te_3 BP. Neither CNTs themselves are well aligned.

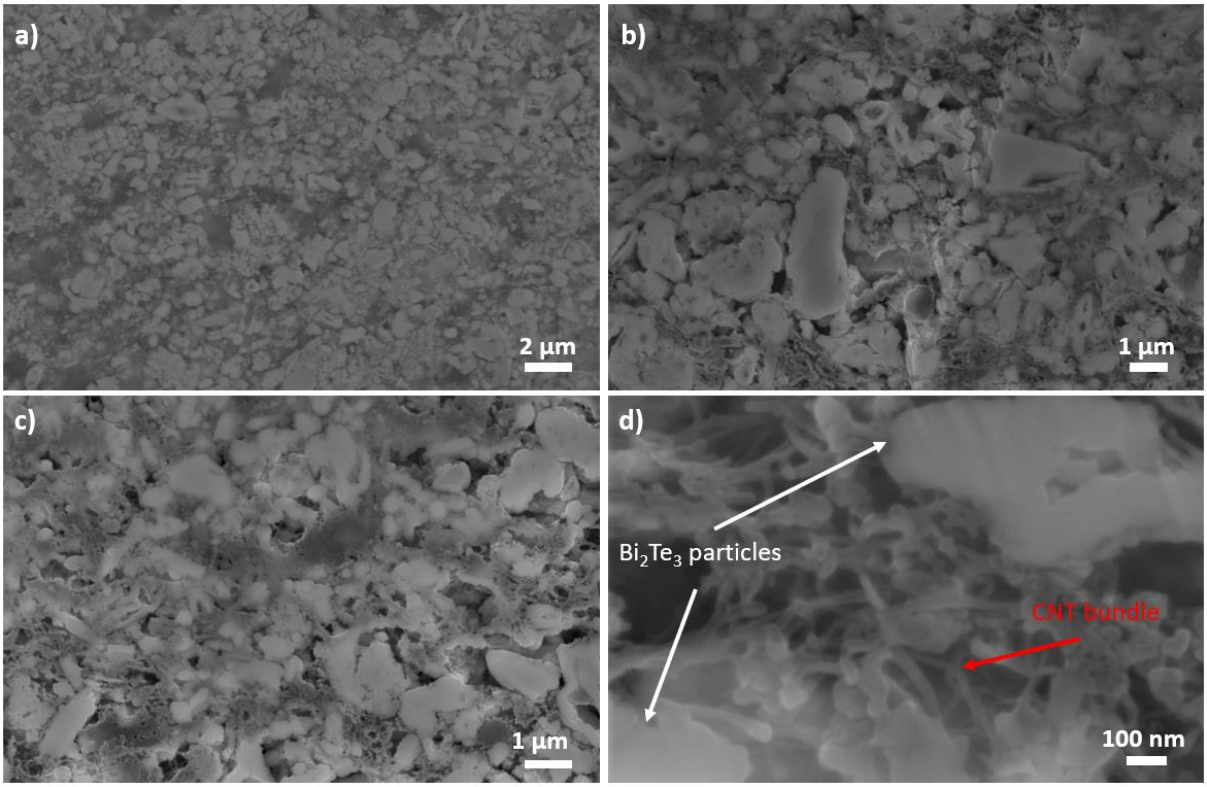

Figure-3.2.6: SEM images of 20%CNT-Bi_2Te_3/epoxy resin composite prepared by infusion method

III.3 TE characterization of composites

The composites prepared by infusion has cylindrical shape with dimensions d = 15 mm and h = 3 mm. Governed by the requirements of specimen size for further measurements of transport properties, the samples were cut as shown in the Figure-3.3.1: square with dimensions 6 x 6 x 1 mm for LFA and rectangular block with dimensions 10 x 3 x 3 for analysis on ZEM3. The electrical resistivity and Seebeck coefficient were measured in a direction perpendicular to the z axis (perpendicular to the filtration direction and along the tubes walls, in-plane) on ZEM3. While thermal diffusivity and specific heat capacity were measured along the z axis (out-of-plane). Such ZT calculated from values measured in perpendicular directions is denoted as apparent ZT.

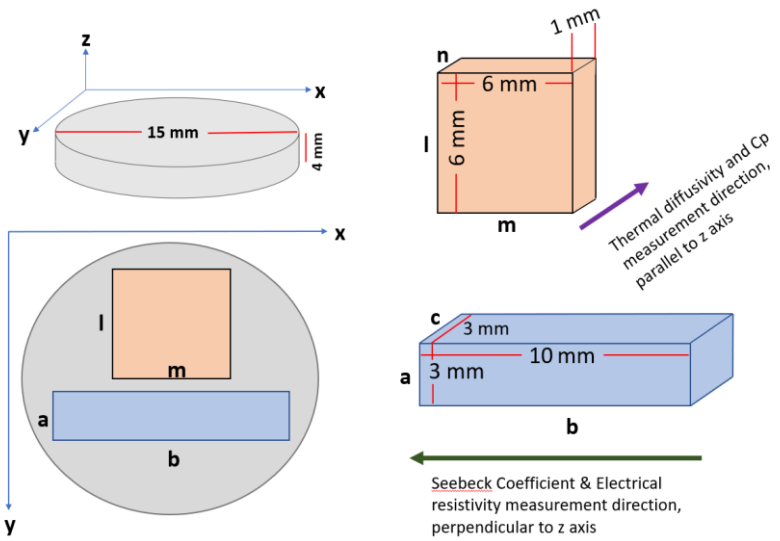

Figure-3.3.1 – Cutting schematics of the composites into specimens for transport properties measurement and transport property measurement directions

Infusion followed by removal of the excess resin does not permit to control the ratio of the added resin. Therefore, content of the filler in the composites prepared by infusion was calculated after the preparation using "the rule of mixtures", which states:[181]

$$\rho_c = \rho_f f_f + \rho_m(1 - f_f)$$

where ρ_c – density of the composite; ρ_f- density of the filler; f_f- volume fraction of the filler; ρ_m – density of the matrix.

The density of the composites (Table-3.3.1) and epoxy resin (1150 kg/m^3) were measured by Archimedes method. The following assumptions were made: density of the Bi_2Te_3

was taken as its bulk density value of 7700 kg/m^3, the bulk density of the CNT is assumed as 1700 kg/m^3 (the lower limit of the possible bulk density of MWCNT).

Table – 3.3.1 Densities and filler fractions of the composites

Name of the composite	Measured density, kg/m^3	Volume fraction of the filler, %	Mass fraction of the filler, %
Bi_2Te_3/epoxy	3787	40	81
10% CNT-Bi_2Te_3/epoxy	3457	42	82
20% CNT-Bi_2Te_3/epoxy	3018	31	74

Thermoelectric properties of Bi_2Te_3/epoxy composite are depicted on Figure-3.3.2 as a function of temperature between room temperature and 150°C to avoid any temperature induced structural modification as observed by Madan et al. Due to insulating nature of the epoxy resin, the resistivity of the composite is 51 mΩ·cm (Figure-3.3.2a), which is 25 times higher than resistivity of pure Bi_2Te_3. However, considering highly insulating nature of the matrix this value is logical. The resistivity increases with temperature, retaining degenerate nature of the conduction. Dependence of the Seebeck coefficient on temperature (Figure-3.3.2a) also remains similar to the evolution of the Seebeck coefficient in pure Bi_2Te_3, and passes through maximum around 130°C. Yet, the maximum Seebeck coefficient in pure Bi_2Te_3 is observed at 100°C. This lag can be explained by slower diffusion of the heat in the polymer. The composite demonstrates maximum Seebeck coefficient of α_{max} = -108 μV/K, which is almost twice lower than the Seebeck coefficient of sintered pure Bi_2Te_3 (α_{max} = -190 μV/K). Upon incorporation of Bi_2Te_3 in epoxy resin matrix, the carrier concentration for the bulk mass of the composite is expected to decreases as the matrix does not produce charge carriers. This, in turn, is expected to increase the Seebeck coefficient. However, in the current case, the Seebeck coefficient decreased. It could be a result of probable decrease of the main charge carrier mobility in the Bi_2Te_3 due to scattering at filler/matrix interface. This behaviour contradicts to the observation made by Madan et al.[135] where Seebeck coefficient is increased upon preparing Bi_2Te_3/epoxy resin composite via dispenser printing. Yet, the morphology of the filler in the report by Madan et al. is coarse particles with sizes more than 2 μm, which in comparison with our composite create less interface, thus less scattering. Comparing two contradicting observations in similar hybrid composites, it can be concluded that the amount of the interface might play a tremendous role in governing the TE behaviour of the composite.

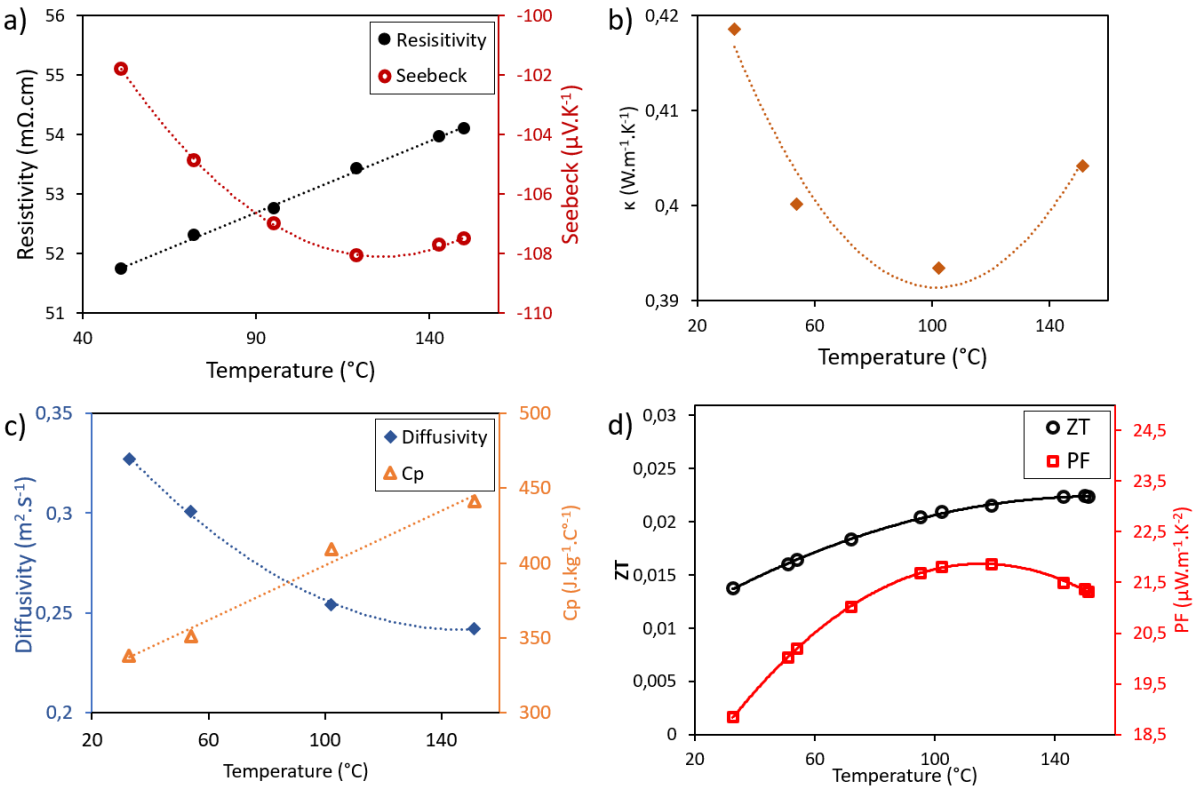

Figure-3.3.2. Dependence of TE properties of Bi_2Te_3/epoxy resin composite (prepared by infusion) on temperature measured in a heating mode: a) Resistivity and Seebeck coefficients; b) thermal conductivity (calculated); c) thermal diffusivity and specific heat; d) ZT and PF (calculated)

Thermal conductivity κ of the composite is around 0.4 W/m·K (Figure-3.3.2b) and logically lower than that of pure sintered Bi_2Te_3, which has been measured at 0.7 W/m·K for the R-30 sample. Yet, such reduction is not enough to fully compensate the drop in electrical conductivity and Seebeck coefficient. The thermal conductivity of the composite undergoes through minima around 100°C. Such evolution of κ can be explained by increasing specific heat capacity and decreasing thermal diffusivity by temperature (Figure-3.3.2c). The PF_{max} is 22 µW/m·K^2, which is 70 times less than the PF reached by pure Bi_2Te_3 sample. Such value is expected considering the dramatic decrease of the electrical conductivity and Seebeck coefficient upon compositing. ZT_{max} is 0.025, considering only slight improvement in thermal conductivity while both Seebeck coefficient and electrical conductivity significantly decreased compared to pure Bi_2Te_3.

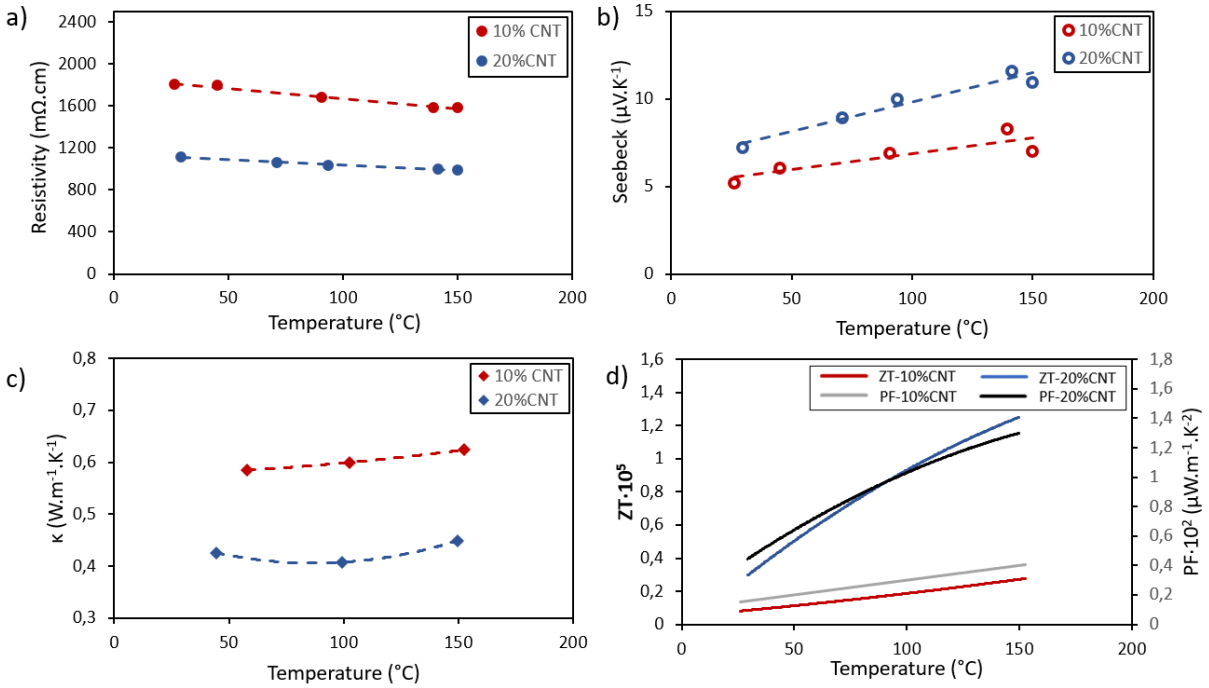

Figure-3.3.3. Dependence of TE properties of Bi_2Te_3/CNT/epoxy resin composites (as a function of temperature: a) Resistivity b) Seebeck coefficients; c) thermal conductivity (calculated); d) ZT and PF (calculated)

Analysis of CNT/Bi_2Te_3/epoxy resin composites is shown in Figure-3.3.3. Comparison of the values are complicated because the preparation method did not allow to control the filler/matrix ratio precisely and calculation of this ratio after the preparation made with certain assumptions, therefore not precise. Yet the trends of the properties as a function of temperature are comparable. In contrast with the composite with only Bi_2Te_3 filler, the resistivities of the later composites decrease with temperature, demonstrating the dominance of conduction governed by CNT. The resistivities of the composites, in spite the addition of more conductive CNT increases dramatically up to 1800 mΩ·cm for a 10%CNT composite and 1120 mΩ·cm for 20%CNT composite, in contrast with 51 mΩ·cm for the composite without CNT. In contrast with bulk rigid Bi_2Te_3 nanoparticles, CNT (higher surface area and softer structure) forms more porous structure during the preparation of BP, which might result in a higher ratio of the epoxy resin in the composite (according to the table 3.3.1), thus in higher resistivities. Additionally, porous structure of the composite itself also contributes to the increase of electrical resistivity. Evolution of the Seebeck coefficient shows positive values in accordance with the p-type conduction of CNT. Seebeck coefficient of the three component composites varies from 5 μV/K to 11 μV/K, which is comparable with the Seebeck coefficients of CNT/epoxy composites in the literature[180] and the one prepared in the course of this experiment (α_{max} = 8 μV/K).

Thermal conductivities of the ternary composites are mainly governed by the ratio of the matrix. Thus, the sample with 20% of CNT, which has higher ratio of the matrix according to calculation (Table -3.3.1) shows lower thermal conductivity. In the case of similar matrix to filler ratio, the opposite is expected as CNT has higher thermal conductivity than Bi_2Te_3, thus its higher ratio would lead to higher thermal conductivity. Due to high electrical resistivity and low Seebeck coefficients, PF and ZT values are dramatically low in comparison with Bi_2Te_3/epoxy resin composite with $PF_{max}=0.5\cdot10^{-2}$ μW/m·K and $ZT_{max}=0.3\cdot10^{-5}$ for composite with 10% CNT loading, and $PF_{max}=1.1\cdot10^{-2}$ μW/m·K and $ZT_{max}=10^{-5}$ for composite with 20% CNT loading. Therefore, despite providing a mechanical stability and simplifying the infusion step, incorporation of CNT dramatically decreases the TE properties of the Bi_2Te_3/epoxy resin composites. Therefore, more productive way to improve both, mechanical and TE properties of Bi_2Te_3/epoxy resin composites would be utilization of Bi_2Te_3 nanoparticles with higher content of nanotubes and higher aspects ratios developed later in the Chapter II.

III Conclusion

In this chapter Bi_2Te_3/epoxy resin hybrid composites were prepared by several methods. Mixing methods as manual mixing and speed mixing are concluded to be not-suitable to prepare composite with percolating network using as-synthesised Bi_2Te_3 nanoparticles. Manual mixing leads to agglomeration of the particles and sedimentation of the agglomerate, while speed mixing, even at maximum attainable filler loading for the method, could not provide homogeneous composites. In contrast, newly adopted infusion method yields nanocomposite with percolating filler network, which provide thermoelectrical properties to the material. Specificity of the three-step preparation process allows to align majority of the Bi_2Te_3 nanotubes in one plane direction. Inclusion of the isolating matrix leads to a strong decrease of the thermal conductivity compared to pure Bi_2Te_3. However, this decrease is not sufficient to fully compensate the decrease of electrical conductivity and Seebeck coefficient, thus, the composite has much lower ZT_{max} = 0.025 in contrast with pure Bi_2Te_3. Inclusion of the MWCNT into the composite had negative influence on the properties of the composite. Ternary composites showed higher porosity and much lower thermoelectrical performance.

General conclusion

The main focus of the current thesis was to develop methods to synthesize Bi_2Te_3 nanoparticles with tubular morphology for thermoelectric application. As a result, 1-DDT assisted reflux synthesis method, which yields Bi_2Te_3 nanoparticles with different content of nanotubes at slight changes of the reaction conditions, was established. When the precursors are allowed to react in an ionic state the nanotubes form via rolling-up mechanism, which involves formation of sheets and its subsequent rolling up into tubes. Under such conditions, reaction yields single phase rhombohedral Bi_2Te_3 with 30% nanotubes content. When the precursors are reacted after their oxidation into elemental states, the reaction follows nanoscale Kirkendall diffusion and yields Bi_2Te_3 with nanotubes content ranging from 50% up to 100%, depending on the re-crystallization step of the Te precursor. Thus, oxidation of Te from its reduced ionic state which leads to its re-crystallization into different morphology governs the morphology of the final Bi_2Te_3 particles, as precipitated Te plays the role of an in-situ template. Therefore, the effect of re-crystallization condition on the morphology of the precipitated Te was thoroughly investigated. Investigation shows that the Te morphology is highly affected by the surfactant and the rate of the oxidant application. Best quality Te rods are obtained at high rates of oxidant supply and in the presence of surfactant.

The uniqueness of the developed 1-DDT assisted reflux synthesis method is mild reaction conditions. All Bi_2Te_3 nanoparticles are obtained at 70°C under reflux and water is used as a major solvent. The reaction is easily scalable. Despite the difference in the mechanisms, this method always produces pure Bi_2Te_3 phase with rhombohedral arrangement of atoms in the crystal lattice according to XRD patterns. Thermoelectrical characterization of selected samples demonstrate competitive n-type Seebeck coefficients around 180 μV/K. Although certain improvement in reduction of thermal conductivity is achieved, yet further improvement is needed to compete with state-of-the-art materials. The main aspect restraining the thermoelectric performance of the tested samples are low electrical conductivities. Yet, considering the absence of extrinsic doping and relatively mild reaction conditions, the ZT of 0.49 is a competitive value. Optimization of sintering conditions and using best quality nanotubes should allow increasing this value.

Additionally, methods to elaborate the obtained nanoparticles into polymer hybrid composite were explored. Among studied methods, only newly adopted infusion method yields nanocomposite with percolating filler network, which provide thermoelectrical properties to the

material. Specificity of the three-step preparation process allows to align majority of the Bi_2Te_3 nanotubes in one plane direction. Inclusion of the isolating polymer matrix leads as expected to materials with lower thermal conductivity than pure Bi_2Te_3. However, this decrease is not sufficient to compensate the lower electrical conductivity and Seebeck coefficient, thus, the composite has much lower (apparent) $ZT_{max} = 0.025$. Yet, it is the first example of bulk hybrid composite of Bi_2Te_3 with an insulating polymer matrix and its thermoelectrical performance is comparable with its reported thin film analogous even if the best quality tubes have not been used.

Obtained results have value in several aspects. Firstly, developed 1-DDT assisted synthesis method shows possibility of obtaining Bi_2Te_3 nanoparticles at relatively mild reaction conditions in contrast with reported similar methods. It also shows how morphological content can be tuned by changing the reaction parameters. Obtaining Bi_2Te_3 nanoparticles with different content of nanotubes allows to highlight that in improving the thermoelectrical properties of material by nano-structuring, not only the size of particles matters, but also its morphology, as Bi_2Te_3 sample with higher content of nanotubes clearly shows better thermoelectric performance in comparison with low nanotube content samples. Thirdly, adopting the composite preparation by infusion method, which is usually used for CNT fillers, demonstrates the possibility that the process can be applied to more rigid fillers with lower aspect ratio.

Future work in the project should start from a deeper characterization of best quality Bi_2Te_3 nanotubes which have been obtained at the very end of this research project. Further direction of the work could be investigation crystal domain size and tubes aspect ratio dependence on the reaction condition. More precisely, investigate if the crystal domain size of Te template correlates with the size of resulting Bi_2Te_3 crystal size and if it does, explore methods to adjust the Te crystal size with the aim to govern the crystal size of the resulting Bi_2Te_3. Monitoring precisely the surfactant concentration and surfactant to precursors ratio could allow tailoring the tubes morphology. Optimizing the sintering conditions for these high aspect ratio particles would allow establishing relationships between the nanotubes aspect ratio and the thermoelectrical properties of sintered samples. Eventually using these top-quality Bi_2Te_3 to process buckypapers in which thermoset resins will be more easily infused might help increasing the overall thermoelectric properties of this new category of conductive polymer composites.

Reference List

(1) Nolas, G. S.; Sharp, J.; Goldsmid, H. J. *Thermoelectrics*, 1st ed.; Springer Berlin: Heidelberg.

(2) Goldsmid, H. J. *Introduction to Thermoelectricity*, 1st ed.; Springer Berlin, Heidelberg: Heidelberg.

(3) Chen, G.; Dresselhaus, M. S.; Dresselhaus, G.; Fleurial, J.-P.; Caillat, T. Recent Developments in Thermoelectric Materials. *International Materials Reviews* **2003**, *48* (1), 45–66. https://doi.org/10.1179/095066003225010182.

(4) Polozine, A.; Sirotinskaya, S.; Schaeffer, L. History of Development of Thermoelectric Materials for Electric Power Generation and Criteria of Their Quality. *Mat. Res.* **2014**, *17*, 1260–1267. https://doi.org/10.1590/1516-1439.272214.

(5) GOLDSMID, H. J. XXVII. Thermoelectric Applications of Semiconductors. *International Journal Of Electronics* **2007**. https://doi.org/10.1080/00207215508961410.

(6) Hicks, L. D.; Dresselhaus, M. S. Effect of Quantum-Well Structures on the Thermoelectric Figure of Merit. *Phys. Rev. B* **1993**, *47* (19), 12727–12731. https://doi.org/10.1103/PhysRevB.47.12727.

(7) Hicks, L. D.; Dresselhaus, M. S. Thermoelectric Figure of Merit of a One-Dimensional Conductor. *Phys. Rev. B* **1993**, *47* (24), 16631–16634. https://doi.org/10.1103/PhysRevB.47.16631.

(8) Pei, Y.; Wang, H.; Snyder, G. J. Band Engineering of Thermoelectric Materials. *Advanced Materials* **2012**, *24* (46), 6125–6135. https://doi.org/10.1002/adma.201202919.

(9) Twaha, S.; Zhu, J.; Yan, Y.; Li, B. A Comprehensive Review of Thermoelectric Technology: Materials, Applications, Modelling and Performance Improvement. *Renewable and Sustainable Energy Reviews* **2016**, *65*, 698–726. https://doi.org/10.1016/j.rser.2016.07.034.

(10) Jouhara, H.; Żabnieńska-Góra, A.; Khordehgah, N.; Doraghi, Q.; Ahmad, L.; Norman, L.; Axcell, B.; Wrobel, L.; Dai, S. Thermoelectric Generator (TEG) Technologies and Applications. *International Journal of Thermofluids* **2021**, *9*, 100063. https://doi.org/10.1016/j.ijft.2021.100063.

(11) Andrei, V.; Bethke, K.; Rademann, K. Thermoelectricity in the Context of Renewable Energy Sources: Joining Forces Instead of Competing. *Energy Environ. Sci.* **2016**, *9* (5), 1528–1532. https://doi.org/10.1039/C6EE00247A.

(12) Champier, D. Thermoelectric Generators: A Review of Applications. *Energy Conversion and Management* **2017**, *140*, 167–181. https://doi.org/10.1016/j.enconman.2017.02.070.

(13) Alam, H.; Ramakrishna, S. A Review on the Enhancement of Figure of Merit from Bulk to Nano-Thermoelectric Materials. *Nano Energy* **2013**, *2* (2), 190–212. https://doi.org/10.1016/j.nanoen.2012.10.005.

(14) Zevros, H. *Thermoelectric Generators: A $750 Million market by 2022*. IDTechEx. https://www.idtechex.com/fr/research-article/thermoelectric-generators-a-750-million-market-by-2022/4631 (accessed 2022-07-29).

(15) Tan, G.; Shi, F.; Hao, S.; Zhao, L.-D.; Chi, H.; Zhang, X.; Uher, C.; Wolverton, C.; Dravid, V. P.; Kanatzidis, M. G. Non-Equilibrium Processing Leads to Record High Thermoelectric Figure of Merit in PbTe–SrTe. *Nat Commun* **2016**, *7* (1), 12167. https://doi.org/10.1038/ncomms12167.

(16) Chang, C.; Wu, M.; He, D.; Pei, Y.; Wu, C.-F.; Wu, X.; Yu, H.; Zhu, F.; Wang, K.; Chen, Y.; Huang, L.; Li, J.-F.; He, J.; Zhao, L.-D. 3D Charge and 2D Phonon Transports Leading to High Out-of-Plane ZT in n-Type SnSe Crystals. *Science* **2018**, *360* (6390), 778–783. https://doi.org/10.1126/science.aaq1479.

(17) Shi, X.-L.; Zou, J.; Chen, Z.-G. Advanced Thermoelectric Design: From Materials and Structures to Devices. *Chem. Rev.* **2020**, *120* (15), 7399–7515. https://doi.org/10.1021/acs.chemrev.0c00026.

(18) Hegde, G. S.; Prabhu, A. N. A Review on Doped/Composite Bismuth Chalcogenide Compounds for Thermoelectric Device Applications: Various Synthesis Techniques and Challenges. *J. Electron. Mater.* **2022**, *51* (5), 2014–2042. https://doi.org/10.1007/s11664-022-09513-x.

(19) Kim, S. I.; Lee, K. H.; Mun, H. A.; Kim, H. S.; Hwang, S. W.; Roh, J. W.; Yang, D. J.; Shin, W. H.; Li, X. S.; Lee, Y. H.; Snyder, G. J.; Kim, S. W. Dense Dislocation Arrays Embedded in Grain Boundaries for High-Performance Bulk Thermoelectrics. *Science* **2015**, *348* (6230), 109–114. https://doi.org/10.1126/science.aaa4166.

(20) Liu, C.-J.; Lai, H.-C.; Liu, Y.-L.; Chen, L.-R. High Thermoelectric Figure-of-Merit in p-Type Nanostructured (Bi,Sb)2Te3 Fabricated Viahydrothermal Synthesis and Evacuated-and-Encapsulated Sintering. *J. Mater. Chem.* **2012**, *22* (11), 4825–4831. https://doi.org/10.1039/C2JM15185E.

(21) Fan, S.; Zhao, J.; Guo, J.; Yan, Q.; Ma, J.; Hng, H. H. P-Type Bi0.4Sb1.6Te3 Nanocomposites with Enhanced Figure of Merit. *Appl. Phys. Lett.* **2010**, *96* (18), 182104. https://doi.org/10.1063/1.3427427.

(22) Yan, X.; Poudel, B.; Ma, Y.; Liu, W. S.; Joshi, G.; Wang, H.; Lan, Y.; Wang, D.; Chen, G.; Ren, Z. F. Experimental Studies on Anisotropic Thermoelectric Properties and Structures of N-Type Bi2Te2.7Se0.3. *Nano Lett.* **2010**, *10* (9), 3373–3378. https://doi.org/10.1021/nl101156v.

(23) Tan, G.; Zhao, L.-D.; Kanatzidis, M. G. Rationally Designing High-Performance Bulk Thermoelectric Materials. *Chem. Rev.* **2016**, *116* (19), 12123–12149. https://doi.org/10.1021/acs.chemrev.6b00255.

(24) Sharma, P. K.; Senguttuvan, T. D.; Sharma, V. K.; Chaudhary, S. Revisiting the Thermoelectric Properties of Lead Telluride. *Materials Today Energy* **2021**, *21*, 100713. https://doi.org/10.1016/j.mtener.2021.100713.

(25) Fu, T.; Yue, X.; Wu, H.; Fu, C.; Zhu, T.; Liu, X.; Hu, L.; Ying, P.; He, J.; Zhao, X. Enhanced Thermoelectric Performance of PbTe Bulk Materials with Figure of Merit ZT >2 by Multi-Functional Alloying. *Journal of Materiomics* **2016**, *2* (2), 141–149. https://doi.org/10.1016/j.jmat.2016.05.005.

(26) He, W.; Wang, D.; Wu, H.; Xiao, Y.; Zhang, Y.; He, D.; Feng, Y.; Hao, Y.-J.; Dong, J.-F.; Chetty, R.; Hao, L.; Chen, D.; Qin, J.; Yang, Q.; Li, X.; Song, J.-M.; Zhu, Y.; Xu, W.; Niu, C.; Li, X.; Wang, G.; Liu, C.; Ohta, M.; Pennycook, S. J.; He, J.; Li, J.-F.; Zhao, L.-D. High Thermoelectric Performance in Low-Cost $SnS_{0.91}Se_{0.09}$ Crystals. *Science* **2019**, *365* (6460), 1418–1424. https://doi.org/10.1126/science.aax5123.

(27) Peng, K.; Zhang, B.; Wu, H.; Cao, X.; Li, A.; Yang, D.; Lu, X.; Wang, G.; Han, X.; Uher, C.; Zhou, X. Ultra-High Average Figure of Merit in Synergistic Band Engineered SnxNa1−xSe0.9S0.1 Single Crystals. *Materials Today* **2018**, *21* (5), 501–507. https://doi.org/10.1016/j.mattod.2017.11.005.

(28) Fu, C.; Bai, S.; Liu, Y.; Tang, Y.; Chen, L.; Zhao, X.; Zhu, T. Realizing High Figure of Merit in Heavy-Band p-Type Half-Heusler Thermoelectric Materials. *Nat Commun* **2015**, *6* (1), 8144. https://doi.org/10.1038/ncomms9144.

(29) J. Quinn, R.; G. Bos, J.-W. Advances in Half-Heusler Alloys for Thermoelectric Power Generation. *Materials Advances* **2021**, *2* (19), 6246–6266. https://doi.org/10.1039/D1MA00707F.

(30) Graf, T.; Felser, C.; Parkin, S. S. P. Simple Rules for the Understanding of Heusler Compounds. *Progress in Solid State Chemistry* **2011**, *39* (1), 1–50. https://doi.org/10.1016/j.progsolidstchem.2011.02.001.

(31) Shevelkov, A. V. *Thermoelectric Power Generation by Clathrates*; IntechOpen, 2016. https://doi.org/10.5772/65600.

(32) Saiga, Y.; Du, B.; Deng, S. K.; Kajisa, K.; Takabatake, T. Thermoelectric Properties of Type-VIII Clathrate Ba8Ga16Sn30 Doped with Cu. *Journal of Alloys and Compounds* **2012**, *537*, 303–307. https://doi.org/10.1016/j.jallcom.2012.05.049.

(33) Rull-Bravo, M.; Moure, A.; Fernández, J. F.; Martín-González, M. Skutterudites as Thermoelectric Materials: Revisited. *RSC Adv.* **2015**, *5* (52), 41653–41667. https://doi.org/10.1039/C5RA03942H.

(34) Rogl, G.; Grytsiv, A.; Yubuta, K.; Puchegger, S.; Bauer, E.; Raju, C.; Mallik, R. C.; Rogl, P. In-Doped Multifilled n-Type Skutterudites with ZT=1.8. *Acta Materialia* **2015**, *95*, 201–211. https://doi.org/10.1016/j.actamat.2015.05.024.

(35) Cutler, M.; Leavy, J. F.; Fitzpatrick, R. L. Electronic Transport in Semimetallic Cerium Sulfide. *Phys. Rev.* **1964**, *133* (4A), A1143–A1152. https://doi.org/10.1103/PhysRev.133.A1143.

(36) Rowe, D. M.; Min, G. α-in σ Plot as a Thermoelectric Material Performance Indicator. *J Mater Sci Lett* **1995**, *14* (9), 617–619. https://doi.org/10.1007/BF00586157.

(37) Snyder, G. J.; Toberer, E. S. Complex Thermoelectric Materials. *Nature Mater* **2008**, *7* (2), 105–114. https://doi.org/10.1038/nmat2090.

(38) Pei, Y.; LaLonde, A. D.; Heinz, N. A.; Shi, X.; Iwanaga, S.; Wang, H.; Chen, L.; Snyder, G. J. Stabilizing the Optimal Carrier Concentration for High Thermoelectric Efficiency. *Advanced Materials* **2011**, *23* (47), 5674–5678. https://doi.org/10.1002/adma.201103153.

(39) Dashevsky, Z.; Shusterman, S.; Dariel, M. P.; Drabkin, I. Thermoelectric Efficiency in Graded Indium-Doped PbTe Crystals. *Journal of Applied Physics* **2002**, *92* (3), 1425. https://doi.org/10.1063/1.1490152.

(40) Wang, H.; Pei, Y.; LaLonde, A. D.; Snyder, G. J. Weak Electron–Phonon Coupling Contributing to High Thermoelectric Performance in n-Type PbSe. *Proc Natl Acad Sci U S A* **2012**, *109* (25), 9705–9709. https://doi.org/10.1073/pnas.1111419109.

(41) Zhang, J.; Liu, R.; Cheng, N.; Zhang, Y.; Yang, J.; Uher, C.; Shi, X.; Chen, L.; Zhang, W. High-Performance Pseudocubic Thermoelectric Materials from Non-Cubic Chalcopyrite Compounds. *Adv. Mater.* **2014**, *26* (23), 3848–3853. https://doi.org/10.1002/adma.201400058.

(42) Rogers, L. M. Valence Band Structure of SnTe. *J. Phys. D: Appl. Phys.* **1968**, *1* (7), 845–852. https://doi.org/10.1088/0022-3727/1/7/304.

(43) Tan, G.; Shi, F.; Hao, S.; Chi, H.; Bailey, T. P.; Zhao, L.-D.; Uher, C.; Wolverton, C.; Dravid, V. P.; Kanatzidis, M. G. Valence Band Modification and High Thermoelectric Performance in SnTe Heavily Alloyed with MnTe. *J. Am. Chem. Soc.* **2015**, *137* (35), 11507–11516. https://doi.org/10.1021/jacs.5b07284.

(44) Ohta, S.; Nomura, T.; Ohta, H.; Koumoto, K. High-Temperature Carrier Transport and Thermoelectric Properties of Heavily La- or Nb-Doped SrTiO3 Single Crystals. *Journal of Applied Physics* **2005**, *97* (3), 034106. https://doi.org/10.1063/1.1847723.

(45) Heremans, J. P.; Wiendlocha, B.; Chamoire, A. M. Resonant Levels in Bulk Thermoelectric Semiconductors. *Energy Environ. Sci.* **2012**, *5* (2), 5510–5530. https://doi.org/10.1039/C1EE02612G.

(46) Beekman, M.; Morelli, D. T.; Nolas, G. S. Better Thermoelectrics through Glass-like Crystals. *Nature Mater* **2015**, *14* (12), 1182–1185. https://doi.org/10.1038/nmat4461.

(47) Meisner, G. P.; Morelli, D. T.; Hu, S.; Yang, J.; Uher, C. Structure and Lattice Thermal Conductivity of Fractionally Filled Skutterudites: Solid Solutions of Fully Filled and Unfilled End Members. *Phys. Rev. Lett.* **1998**, *80* (16), 3551–3554. https://doi.org/10.1103/PhysRevLett.80.3551.

(48) May, A. F.; Singh, D. J.; Snyder, G. J. Influence of Band Structure on the Large Thermoelectric Performance of Lanthanum Telluride. *Phys. Rev. B* **2009**, *79* (15), 153101. https://doi.org/10.1103/PhysRevB.79.153101.

(49) Wang, S.; Li, H.; Lu, R.; Zheng, G.; Tang, X. Metal Nanoparticle Decorated N-Type Bi$\less$sub$\greater$2$\less$/Sub$\greater$Te$\less$sub$\greater$3$\less$/Sub$\greater$-Based Materials with Enhanced Thermoelectric Performances. *Nanotechnology* **2013**, *24* (28), 285702. https://doi.org/10.1088/0957-4484/24/28/285702.

(50) Rowe, D. M.; Shukla, V. S.; Savvides, N. Phonon Scattering at Grain Boundaries in Heavily Doped Fine-Grained Silicon–Germanium Alloys. *Nature* **1981**, *290* (5809), 765–766. https://doi.org/10.1038/290765a0.

(51) Baig, N.; Kammakakam, I.; Falath, W. Nanomaterials: A Review of Synthesis Methods, Properties, Recent Progress, and Challenges. *Mater. Adv.* **2021**, *2* (6), 1821–1871. https://doi.org/10.1039/D0MA00807A.

(52) Chen, X.; Zhou, Z.; Lin, Y.-H.; Nan, C. Thermoelectric Thin Films: Promising Strategies and Related Mechanism on Boosting Energy Conversion Performance. *Journal of Materiomics* **2020**, *6* (3), 494–512. https://doi.org/10.1016/j.jmat.2020.02.008.

(53) Park, K. H.; Mohamed, M.; Aksamija, Z.; Ravaioli, U. Phonon Scattering Due to van Der Waals Forces in the Lattice Thermal Conductivity of Bi2Te3 Thin Films. *Journal of Applied Physics* **2015**, *117* (1), 015103. https://doi.org/10.1063/1.4905294.

(54) Hosokawa, Y.; Tomita, K.; Takashiri, M. Growth of Single-Crystalline Bi2Te3 Hexagonal Nanoplates with and without Single Nanopores during Temperature-Controlled Solvothermal Synthesis. *Sci Rep* **2019**, *9* (1), 10790. https://doi.org/10.1038/s41598-019-47356-5.

(55) Teweldebrhan, D.; Goyal, V.; Balandin, A. A. Exfoliation and Characterization of Bismuth Telluride Atomic Quintuples and Quasi-Two-Dimensional Crystals. *Nano Lett.* **2010**, *10* (4), 1209–1218. https://doi.org/10.1021/nl903590b.

(56) Pei, J.; Cai, B.; Zhuang, H.-L.; Li, J.-F. Bi2Te3-Based Applied Thermoelectric Materials: Research Advances and New Challenges. *National Science Review* **2020**, *7* (12), 1856–1858. https://doi.org/10.1093/nsr/nwaa259.

(57) Goncalves, L. M.; Couto, C.; Alpuim, P.; Rolo, A. G.; Völklein, F.; Correia, J. H. Optimization of Thermoelectric Properties on Bi2Te3 Thin Films Deposited by Thermal Co-Evaporation. *Thin Solid Films* **2010**, *518* (10), 2816–2821. https://doi.org/10.1016/j.tsf.2009.08.038.

(58) Zou, H.; Rowe, D. M.; Min, G. Growth of P- and n-Type Bismuth Telluride Thin Films by Co-Evaporation. *Journal of Crystal Growth* **2001**, *222* (1), 82–87. https://doi.org/10.1016/S0022-0248(00)00922-2.

(59) Takashiri, M.; Takiishi, M.; Tanaka, S.; Miyazaki, K.; Tsukamoto, H. Thermoelectric Properties of N-Type Nanocrystalline Bismuth-Telluride-Based Thin Films Deposited by Flash Evaporation. *Journal of Applied Physics* **2007**, *101* (7), 074301. https://doi.org/10.1063/1.2717867.

(60) Marinho, A. A.; Costa, N. P.; Pereira, L. F. C.; Brito, F. A.; Chesman, C. Thermoelectric Properties of BiSbTe Alloy Nanofilms Produced by DC Sputtering: Experiments and Modeling. *J Mater Sci* **2020**, *55* (6), 2429–2438. https://doi.org/10.1007/s10853-019-04188-y.

(61) Takashiri, M.; Takano, K.; Hamada, J. Use of H2-Ar Gas Mixtures in Radio-Frequency Magnetron Sputtering to Produce High-Performance Nanocrystalline Bismuth Telluride Thin Films. *Thin Solid Films* **2018**, *664*, 100–105. https://doi.org/10.1016/j.tsf.2018.08.036.

(62) Zhou, Y.; Li, L.; Tan, Q.; Li, J.-F. Thermoelectric Properties of Pb-Doped Bismuth Telluride Thin Films Deposited by Magnetron Sputtering. *Journal of Alloys and Compounds* **2014**, *590*, 362–367. https://doi.org/10.1016/j.jallcom.2013.12.136.

(63) Le, P. H.; Liao, C.-N.; Luo, C. W.; Leu, J. Thermoelectric Properties of Nanostructured Bismuth–Telluride Thin Films Grown Using Pulsed Laser Deposition. *Journal of Alloys and Compounds* **2014**, *615*, 546–552. https://doi.org/10.1016/j.jallcom.2014.07.018.

(64) Manzano, C. V.; Martin-Gonzalez, M. Electrodeposition of V-VI Nanowires and Their Thermoelectric Properties. *Frontiers in Chemistry* **2019**, *7*.

(65) Rostek, R.; Stein, N.; Boulanger, C. A Review of Electroplating for V-VI Thermoelectric Films: From Synthesis to Device Integration. *Journal of Materials Research* **2015**, *30* (17), 2518–2543. https://doi.org/10.1557/jmr.2015.203.

(66) Martín, J.; Manzano, C. V.; Caballero-Calero, O.; Martín-González, M. High-Aspect-Ratio and Highly Ordered 15-Nm Porous Alumina Templates. *ACS Appl. Mater. Interfaces* **2013**, *5* (1), 72–79. https://doi.org/10.1021/am3020718.

(67) Picht, O.; Müller, S.; Alber, I.; Rauber, M.; Lensch-Falk, J.; Medlin, D. L.; Neumann, R.; Toimil-Molares, M. E. Tuning the Geometrical and Crystallographic Characteristics of Bi2Te3 Nanowires by Electrodeposition in Ion-Track Membranes. *J. Phys. Chem. C* **2012**, *116* (9), 5367–5375. https://doi.org/10.1021/jp210491g.

(68) Li, W.-J.; Yu, W.-L.; Yen, C.-Y. Pulsed Electrodeposition of Bi2Te3 and Bi2Te3/Te Nanowire Arrays from a DMSO Solution. *Electrochimica Acta* **2011**, *58*, 510–515. https://doi.org/10.1016/j.electacta.2011.09.075.

(69) Sapp, S. A.; Lakshmi, B. B.; Martin, C. R. Template Synthesis of Bismuth Telluride Nanowires. *Advanced Materials* **1999**, *11* (5), 402–404. https://doi.org/10.1002/(SICI)1521-4095(199903)11:5<402::AID-ADMA402>3.0.CO;2-L.

(70) Newbrook, D. W.; Richards, S. P.; Greenacre, V. K.; Hector, A. L.; Levason, W.; Reid, G.; de Groot, C. H. (Kees); Huang, R. Improved Thermoelectric Performance of Bi2Se3 Alloyed Bi2Te3 Thin Films via Low Pressure Chemical Vapour Deposition. *Journal of Alloys and Compounds* **2020**, *848*, 156523. https://doi.org/10.1016/j.jallcom.2020.156523.

(71) You, H.; Hyub Baek, S.; Kim, K.-C.; Kwon, O.-J.; Kim, J.-S.; Park, C. Growth and Thermoelectric Properties of Bi2Te3 Films Deposited by Modified MOCVD. *Journal of Crystal Growth* **2012**, *346* (1), 17–21. https://doi.org/10.1016/j.jcrysgro.2012.02.033.

(72) Benjamin, S. L.; Groot, C. H. (Kees) de; Gurnani, C.; Hector, A. L.; Huang, R.; Koukharenko, E.; Levason, W.; Reid, G. Controlling the Nanostructure of Bismuth Telluride by Selective Chemical Vapour Deposition from a Single Source Precursor. *J. Mater. Chem. A* **2014**, *2* (14), 4865–4869. https://doi.org/10.1039/C4TA00341A.

(73) Schönherr, P.; Kojda, D.; Srot, V.; Fischer, S. F.; van Aken, P. A.; Hesjedal, T. Perfect Quintuple Layer Bi2Te3 Nanowires: Growth and Thermoelectric Properties. *APL Materials* **2017**, *5* (8), 086110. https://doi.org/10.1063/1.4986524.

(74) Andzane, J.; Kunakova, G.; Charpentier, S.; Hrkac, V.; Kienle, L.; Baitimirova, M.; Bauch, T.; Lombardi, F.; Erts, D. Catalyst-Free Vapour–Solid Technique for Deposition of Bi2Te3 and Bi2Se3 Nanowires/Nanobelts with Topological Insulator Properties. *Nanoscale* **2015**, *7* (38), 15935–15944. https://doi.org/10.1039/C5NR04574F.

(75) Jung, H.; Suh, H.; Hangarter, C. M.; Lim, J. H.; Lee, Y.-I.; Choa, Y.-H.; Hong, K.; Myung, N. V. Programmable Synthesis of Shape-, Structure-, and Composition-Modulated One-Dimensional Heterostructures by Galvanic Displacement Reaction. *Appl. Phys. Lett.* **2012**, *100* (22), 223105. https://doi.org/10.1063/1.4722919.

(76) Liu, J.; Uprety, B.; Gyawali, S.; Woolley, A. T.; Myung, N. V.; Harb, J. N. Fabrication of DNA-Templated Te and Bi2Te3 Nanowires by Galvanic Displacement. *Langmuir* **2013**, *29* (35), 11176–11184. https://doi.org/10.1021/la402678j.

(77) Xiao, F.; Yoo, B.; Lee, K. H.; Myung, N. V. Synthesis of Bi2Te3 Nanotubes by Galvanic Displacement. *J. Am. Chem. Soc.* **2007**, *129* (33), 10068–10069. https://doi.org/10.1021/ja073032w.

(78) Scheele, M.; Oeschler, N.; Meier, K.; Kornowski, A.; Klinke, C.; Weller, H. Synthesis and Thermoelectric Characterization of Bi $_2$ Te $_3$ Nanoparticles. *Adv. Funct. Mater.* **2009**, *19* (21), 3476–3483. https://doi.org/10.1002/adfm.200901261.

(79) Wei, J.; Yang, L.; Ma, Z.; Song, P.; Zhang, M.; Ma, J.; Yang, F.; Wang, X. Review of Current High-ZT Thermoelectric Materials. *J Mater Sci* **2020**, *55* (27), 12642–12704. https://doi.org/10.1007/s10853-020-04949-0.

(80) Akshay, V. R.; Arun, B.; Suneesh, M. V.; Vasundhara, M. Surfactant-Induced Structural Phase Transitions and Enhanced Room Temperature Thermoelectric Performance in n-Type Bi2Te3 Nanostructures Synthesized via Chemical Route. *ACS Appl. Nano Mater.* **2018**, *1* (7), 3236–3250. https://doi.org/10.1021/acsanm.8b00464.

(81) Zhang, G.; Yu, Q.; Yao, Z.; Li, X. Large Scale Highly Crystalline Bi2Te3nanotubes through Solution Phase Nanoscale Kirkendall Effect Fabrication. *Chem. Commun.* **2009**, No. 17, 2317–2319. https://doi.org/10.1039/B822595H.

(82) Kim, S. H.; Park, B. K. Solvothermal Synthesis of Bi2Te3 Nanotubes by the Interdiffusion of Bi and Te Metals. *Materials Letters* **2010**, *64* (8), 938–941. https://doi.org/10.1016/j.matlet.2010.01.065.

(83) Zhu, H.; Zhang, H.; Liang, J.; Rao, G.; Li, J.; Liu, G.; Du, Z.; Fan, H.; Luo, J. Controlled Synthesis of Tellurium Nanostructures from Nanotubes to Nanorods and Nanowires and Their Template Applications. *J. Phys. Chem. C* **2011**, *115* (14), 6375–6380. https://doi.org/10.1021/jp200316y.

(84) Nunes, D.; Pimentel, A.; Santos, L.; Barquinha, P.; Pereira, L.; Fortunato, E.; Martins, R. 2 - Synthesis, Design, and Morphology of Metal Oxide Nanostructures. In *Metal Oxide*

Nanostructures; Nunes, D., Pimentel, A., Santos, L., Barquinha, P., Pereira, L., Fortunato, E., Martins, R., Eds.; Metal Oxides; Elsevier, 2019; pp 21–57. https://doi.org/10.1016/B978-0-12-811512-1.00002-3.

(85) Aditha, S. K.; Kurdekar, A. D.; Chunduri, L. A. A.; Patnaik, S.; Kamisetti, V. Aqueous Based Reflux Method for Green Synthesis of Nanostructures: Application in CZTS Synthesis. *MethodsX* **2016**, *3*, 35–42. https://doi.org/10.1016/j.mex.2015.12.003.

(86) Dong, H.; Chen, Y.-C.; Feldmann, C. Polyol Synthesis of Nanoparticles: Status and Options Regarding Metals, Oxides, Chalcogenides, and Non-Metal Elements. *Green Chem.* **2015**, *17* (8), 4107–4132. https://doi.org/10.1039/C5GC00943J.

(87) Bensebaa, F. Chapter 2 - Wet Production Methods. In *Interface Science and Technology*; Bensebaa, F., Ed.; Nanoparticle Technologies; Elsevier, 2013; Vol. 19, pp 85–146. https://doi.org/10.1016/B978-0-12-369550-5.00002-1.

(88) Yu, C.; Zhang, X.; Leng, M.; Shaga, A.; Liu, D.; Chen, F.; Wang, C. Preparation and Thermoelectric Properties of Inhomogeneous Bismuth Telluride Alloyed Nanorods. *Journal of Alloys and Compounds* **2013**, *570*, 86–93. https://doi.org/10.1016/j.jallcom.2013.03.167.

(89) Zhao, Q.; Wang, Y. G. A Facile Two-Step Hydrothermal Route for the Synthesis of Low-Dimensional Structured Bi2Te3 Nanocrystals with Various Morphologies. *Journal of Alloys and Compounds* **2010**, *497* (1), 57–61. https://doi.org/10.1016/j.jallcom.2010.03.077.

(90) Mi, J.-L.; Lock, N.; Sun, T.; Christensen, M.; Søndergaard, M.; Hald, P.; Hng, H. H.; Ma, J.; Iversen, B. B. Biomolecule-Assisted Hydrothermal Synthesis and Self-Assembly of Bi2Te3 Nanostring-Cluster Hierarchical Structure. *ACS Nano* **2010**, *4* (5), 2523–2530. https://doi.org/10.1021/nn100267q.

(91) Xu, Y.; Ren, Z.; Ren, W.; Cao, G.; Deng, K.; Zhong, Y. Hydrothermal Synthesis of Single-Crystalline Bi2Te3 Nanoplates. *Materials Letters* **2008**, *62* (27), 4273–4276. https://doi.org/10.1016/j.matlet.2008.06.055.

(92) Fu, J.; Song, S.; Zhang, X.; Cao, F.; Zhou, L.; Li, X.; Zhang, H. Bi2Te3 Nanoplates and Nanoflowers: Synthesized by Hydrothermal Process and Their Enhanced Thermoelectric Properties. *CrystEngComm* **2012**, *14* (6), 2159–2165. https://doi.org/10.1039/C2CE06348D.

(93) Zhu, H.-T.; Luo, J.; Liang, J.-K. Synthesis of Highly Crystalline Bi2Te3 Nanotubes and Their Enhanced Thermoelectric Properties. *J. Mater. Chem. A* **2014**, *2* (32), 12821–12826. https://doi.org/10.1039/C4TA02532F.

(94) Wang, Z.; Wang, F.; Chen, H.; Zhu, L.; Yu, H.; Jian, X. Synthesis and Characterization of Bi2Te3 Nanotubes by a Hydrothermal Method. *Journal of Alloys and Compounds* **2010**, *492* (1), L50–L53. https://doi.org/10.1016/j.jallcom.2009.11.155.

(95) Zhao, X. B.; Ji, X. H.; Zhang, Y. H.; Lu, B. H. Effect of Solvent on the Microstructures of Nanostructured Bi2Te3 Prepared by Solvothermal Synthesis. *Journal of Alloys and Compounds* **2004**, *368* (1), 349–352. https://doi.org/10.1016/j.jallcom.2003.08.070.

(96) Wada, K.; Tomita, K.; Takashiri, M. Fabrication of Bismuth Telluride Nanoplates via Solvothermal Synthesis Using Different Alkalis and Nanoplate Thin Films by Printing Method. *Journal of Crystal Growth* **2017**, *468*, 194–198. https://doi.org/10.1016/j.jcrysgro.2016.12.048.

(97) Xu, Y.; Ren, Z.; Cao, G.; Ren, W.; Deng, K.; Zhong, Y. Fabrication and Characterization of Bi2Te3 Nanoplates via a Simple Solvothermal Process. *Physica B: Condensed Matter* **2009**, *404* (21), 4029–4033. https://doi.org/10.1016/j.physb.2009.07.153.

(98) Jin, R.; Liu, J.; Li, G. Facile Solvothermal Synthesis, Growth Mechanism and Thermoelectric Property of Flower-like Bi2Te3. *Crystal Research and Technology* **2014**, *49* (7), 460–466. https://doi.org/10.1002/crat.201400012.

(99) Wang, K.; Liang, H.-W.; Yao, W.-T.; Yu, S.-H. Templating Synthesis of Uniform Bi2Te3 Nanowires with High Aspect Ratio in Triethylene Glycol (TEG) and Their Thermoelectric Performance. *J. Mater. Chem.* **2011**, *21* (38), 15057–15062. https://doi.org/10.1039/C1JM12384J.

(100) He, M.; Ge, J.; Lin, Z.; Feng, X.; Wang, X.; Lu, H.; Yang, Y.; Qiu, F. Thermopower Enhancement in Conducting Polymer Nanocomposites via Carrier Energy Scattering at the Organic–Inorganic

Semiconductor Interface. *Energy Environ. Sci.* **2012**, *5* (8), 8351–8358. https://doi.org/10.1039/C2EE21803H.

(101) Dou, Y.; Wu, F.; Fang, L.; Liu, G.; Mao, C.; Wan, K.; Zhou, M. Enhanced Performance of Dye-Sensitized Solar Cell Using Bi2Te3 Nanotube/ZnO Nanoparticle Composite Photoanode by the Synergistic Effect of Photovoltaic and Thermoelectric Conversion. *Journal of Power Sources* **2016**, *307*, 181–189. https://doi.org/10.1016/j.jpowsour.2015.12.113.

(102) Nishiwaki, S.; Itoh, T. Synthesis of Bi $_2$ Te $_3$ Nanosheets Using Polyol Process. *IOP Conf. Ser.: Mater. Sci. Eng.* **2011**, *18* (14), 142009. https://doi.org/10.1088/1757-899X/18/14/142009.

(103) Sun, T.; Zhao, X. B.; Zhu, T. J.; Tu, J. P. Aqueous Chemical Reduction Synthesis of Bi2Te3 Nanowires with Surfactant Assistance. *Materials Letters* **2006**, *60* (20), 2534–2537. https://doi.org/10.1016/j.matlet.2006.01.033.

(104) Kim, D.; Du, R.; Yu, S.-Y.; Yin, Y.; Dong, S.; Li, Q.; Mohney, S. E.; Li, X.; Tadigadapa, S. Enhanced Thermoelectric Efficiency in Nanocrystalline Bismuth Telluride Nanotubes. *Nanotechnology* **2020**, *31* (36), 365703. https://doi.org/10.1088/1361-6528/ab97d2.

(105) Toshima, N. Recent Progress of Organic and Hybrid Thermoelectric Materials. *Synthetic Metals* **2017**, *225*, 3–21. https://doi.org/10.1016/j.synthmet.2016.12.017.

(106) Russ, B.; Glaudell, A.; Urban, J. J.; Chabinyc, M. L.; Segalman, R. A. Organic Thermoelectric Materials for Energy Harvesting and Temperature Control. *Nat Rev Mater* **2016**, *1* (10), 1–14. https://doi.org/10.1038/natrevmats.2016.50.

(107) Cowen, L. M.; Atoyo, J.; Carnie, M. J.; Baran, D.; Schroeder, B. C. Review—Organic Materials for Thermoelectric Energy Generation. *ECS J. Solid State Sci. Technol.* **2017**, *6* (3), N3080. https://doi.org/10.1149/2.0121703jss.

(108) Wang, H.; Yu, C. Organic Thermoelectrics: Materials Preparation, Performance Optimization, and Device Integration. *Joule* **2019**, *3* (1), 53–80. https://doi.org/10.1016/j.joule.2018.10.012.

(109) Peng, S.; Wang, D.; Lu, J.; He, M.; Xu, C.; Li, Y.; Zhu, S. A Review on Organic Polymer-Based Thermoelectric Materials. *J Polym Environ* **2017**, *25* (4), 1208–1218. https://doi.org/10.1007/s10924-016-0895-z.

(110) Yan, H.; Ohta, T.; Toshima, N. Stretched Polyaniline Films Doped by (±)-10-Camphorsulfonic Acid: Anisotropy and Improvement of Thermoelectric Properties. *Macromol. Mater. Eng.* **2001**, *286* (3), 139–142. https://doi.org/10.1002/1439-2054(20010301)286:3<139::AID-MAME139>3.0.CO;2-F.

(111) Hiroshige, Y.; Ookawa, M.; Toshima, N. Thermoelectric Figure-of-Merit of Iodine-Doped Copolymer of Phenylenevinylene with Dialkoxyphenylenevinylene. *Synthetic Metals* **2007**, *157* (10), 467–474. https://doi.org/10.1016/j.synthmet.2007.05.003.

(112) Lindorf, M.; Mazzio, K. A.; Pflaum, J.; Nielsch, K.; Brütting, W.; Albrecht, M. Organic-Based Thermoelectrics. *J. Mater. Chem. A* **2020**, *8* (16), 7495–7507. https://doi.org/10.1039/C9TA11717B.

(113) Zuzok, R.; Kaiser, A. B.; Pukacki, W.; Roth, S. Thermoelectric Power and Conductivity of Iodine-doped ‘“New”’ Polyacetylene. *The Journal of Chemical Physics* **1991**, *95* (2), 1270–1275. https://doi.org/10.1063/1.461107.

(114) Groenendaal, L.; Jonas, F.; Freitag, D.; Pielartzik, H.; Reynolds, J. R. Poly(3,4-Ethylenedioxythiophene) and Its Derivatives: Past, Present, and Future. *Advanced Materials* **2000**, *12* (7), 481–494. https://doi.org/10.1002/(SICI)1521-4095(200004)12:7<481::AID-ADMA481>3.0.CO;2-C.

(115) Fan, Z.; Ouyang, J. Thermoelectric Properties of PEDOT:PSS. *Advanced Electronic Materials* **2019**, *5* (11), 1800769. https://doi.org/10.1002/aelm.201800769.

(116) Worfolk, B. J.; Andrews, S. C.; Park, S.; Reinspach, J.; Liu, N.; Toney, M. F.; Mannsfeld, S. C. B.; Bao, Z. Ultrahigh Electrical Conductivity in Solution-Sheared Polymeric Transparent Films. *Proceedings of the National Academy of Sciences* **2015**, *112* (46), 14138–14143. https://doi.org/10.1073/pnas.1509958112.

(117) Kim, G.-H.; Shao, L.; Zhang, K.; Pipe, K. P. Engineered Doping of Organic Semiconductors for Enhanced Thermoelectric Efficiency. *Nature Mater* **2013**, *12* (8), 719–723. https://doi.org/10.1038/nmat3635.

(118) Sun, Y.; Di, C.; Xu, W.; Zhu, D. Advances in N-Type Organic Thermoelectric Materials and Devices. *Adv. Electron. Mater.* **2019**, *5* (11), 1800825. https://doi.org/10.1002/aelm.201800825.

(119) Sun, Y.; Sheng, P.; Di, C.; Jiao, F.; Xu, W.; Qiu, D.; Zhu, D. Organic Thermoelectric Materials and Devices Based on P- and n-Type Poly(Metal 1,1,2,2-Ethenetetrathiolate)s. *Adv. Mater.* **2012**, *24* (7), 932–937. https://doi.org/10.1002/adma.201104305.

(120) Jin, H.; Li, J.; Iocozzia, J.; Zeng, X.; Wei, P.-C.; Yang, C.; Li, N.; Liu, Z.; He, J. H.; Zhu, T.; Wang, J.; Lin, Z.; Wang, S. Hybrid Organic–Inorganic Thermoelectric Materials and Devices. *Angewandte Chemie International Edition* **2019**, *58* (43), 15206–15226. https://doi.org/10.1002/anie.201901106.

(121) An, H.; Pusko, M.; Chun, D.; Park, S.; Moon, J. In-Situ Synthesis of Flexible Hybrid Composite Films for Improved Thermoelectric Performance. *Chemical Engineering Journal* **2019**, *357*, 547–558. https://doi.org/10.1016/j.cej.2018.09.200.

(122) Wang, H.; Yi, S.; Yu, C. Engineering Electrical Transport at the Interface of Conjugated Carbon Structures to Improve Thermoelectric Properties of Their Composites. *Polymer* **2016**, *97*, 487–495. https://doi.org/10.1016/j.polymer.2016.05.062.

(123) Blackburn, J. L.; Ferguson, A. J.; Cho, C.; Grunlan, J. C. Carbon-Nanotube-Based Thermoelectric Materials and Devices. *Advanced Materials* **2018**, *30* (11), 1704386. https://doi.org/10.1002/adma.201704386.

(124) Toshima, N.; Jiravanichanun, N.; Marutani, H. Organic Thermoelectric Materials Composed of Conducting Polymers and Metal Nanoparticles. *J. Electron. Mater.* **2012**, *41* (6), 1735–1742. https://doi.org/10.1007/s11664-012-2041-6.

(125) Wang, H.; Hsu, J.-H.; Yi, S.-I.; Kim, S. L.; Choi, K.; Yang, G.; Yu, C. Thermally Driven Large N-Type Voltage Responses from Hybrids of Carbon Nanotubes and Poly(3,4-Ethylenedioxythiophene) with Tetrakis(Dimethylamino)Ethylene. *Advanced Materials* **2015**, *27* (43), 6855–6861. https://doi.org/10.1002/adma.201502950.

(126) Wang, Q.; Yao, Q.; Chang, J.; Chen, L. Enhanced Thermoelectric Properties of CNT/PANI Composite Nanofibers by Highly Orienting the Arrangement of Polymer Chains. *J. Mater. Chem.* **2012**, *22* (34), 17612–17618. https://doi.org/10.1039/C2JM32750C.

(127) Du, Y.; Shen, S. Z.; Cai, K.; Casey, P. S. Research Progress on Polymer–Inorganic Thermoelectric Nanocomposite Materials. *Progress in Polymer Science* **2012**, *37* (6), 820–841. https://doi.org/10.1016/j.progpolymsci.2011.11.003.

(128) Yao, Q.; Chen, L.; Zhang, W.; Liufu, S.; Chen, X. Enhanced Thermoelectric Performance of Single-Walled Carbon Nanotubes/Polyaniline Hybrid Nanocomposites. *ACS Nano* **2010**, *4* (4), 2445–2451. https://doi.org/10.1021/nn1002562.

(129) Yao, Q.; Wang, Q.; Wang, L.; Chen, L. Abnormally Enhanced Thermoelectric Transport Properties of SWNT/PANI Hybrid Films by the Strengthened PANI Molecular Ordering. *Energy Environ. Sci.* **2014**, *7* (11), 3801–3807. https://doi.org/10.1039/C4EE01905A.

(130) Yu, C.; Kim, Y. S.; Kim, D.; Grunlan, J. C. Thermoelectric Behavior of Segregated-Network Polymer Nanocomposites. *Nano Lett* **2008**, *8* (12), 4428–4432. https://doi.org/10.1021/nl802345s.

(131) Choi, Y.; Kim, Y.; Park, S. G.; Kim, Y. G.; Sung, B. J.; Jang, S. Y.; Kim, W. Effect of the Carbon Nanotube Type on the Thermoelectric Properties of CNT/Nafion Nanocomposites. *Organic Electronics: physics, materials, applications* **2011**, *12* (12), 2120–2125. https://doi.org/10.1016/j.orgel.2011.08.025.

(132) Wang, L.; Liu, Y.; Zhang, Z.; Wang, B.; Qiu, J.; Hui, D.; Wang, S. Polymer Composites-Based Thermoelectric Materials and Devices. *Composites Part B: Engineering* **2017**, *122*, 145–155. https://doi.org/10.1016/j.compositesb.2017.04.019.

(133) Du, Y.; Cai, K. F.; Chen, S.; Cizek, P.; Lin, T. Facile Preparation and Thermoelectric Properties of Bi2Te3 Based Alloy Nanosheet/PEDOT:PSS Composite Films. *ACS Appl. Mater. Interfaces* **2014**, *6* (8), 5735–5743. https://doi.org/10.1021/am5002772.

(134) Xue, Q. The Influence of Particle Shape and Size on Electric Conductivity of Metal–Polymer Composites. *European Polymer Journal* **2004**, *40* (2), 323–327. https://doi.org/10.1016/j.eurpolymj.2003.10.011.

(135) Madan, D.; Chen, A.; Wright, P. K.; Evans, J. W. Dispenser Printed Composite Thermoelectric Thick Films for Thermoelectric Generator Applications. *Journal of Applied Physics* **2011**, *109* (3), 034904. https://doi.org/10.1063/1.3544501.

(136) Madan, D.; Wang, Z.; Chen, A.; Juang, R.; Keist, J.; Wright, P. K.; Evans, J. W. Enhanced Performance of Dispenser Printed MA N-Type Bi2Te3 Composite Thermoelectric Generators. *ACS Appl. Mater. Interfaces* **2012**, *4* (11), 6117–6124. https://doi.org/10.1021/am301759a.

(137) Chen, A.; Madan, D.; Wright, P. K.; Evans, J. W. Dispenser-Printed Planar Thick-Film Thermoelectric Energy Generators. *J. Micromech. Microeng.* **2011**, *21* (10), 104006. https://doi.org/10.1088/0960-1317/21/10/104006.

(138) Madan, D.; Wang, Z.; Chen, A.; Winslow, R.; Wright, P. K.; Evans, J. W. Dispenser Printed Circular Thermoelectric Devices Using Bi and Bi0.5Sb1.5Te3. *Appl. Phys. Lett.* **2014**, *104* (1), 013902. https://doi.org/10.1063/1.4861057.

(139) Cao, Z.; Koukharenko, E.; Tudor, M. J.; Torah, R. N.; Beeby, S. P. Screen Printed Flexible Bi$\less$sub$\greater$2$\less$/Sub$\greater$Te$\less$sub$\greater$3$\less$/Sub$\greater$-Sb$\less$sub$\greater$2$\less$/Sub$\greater$Te$\less$sub$\greater$3$\less$/Sub$\greater$based Thermoelectric Generator. *J. Phys.: Conf. Ser.* **2013**, *476*, 012031. https://doi.org/10.1088/1742-6596/476/1/012031.

(140) Hou, W.; Nie, X.; Zhao, W.; Zhou, H.; Mu, X.; Zhu, W.; Zhang, Q. Fabrication and Excellent Performances of Bi0.5Sb1.5Te3/Epoxy Flexible Thermoelectric Cooling Devices. *Nano Energy* **2018**, *50*, 766–776. https://doi.org/10.1016/j.nanoen.2018.06.020.

(141) Rijal, B.; Baimyrza, A.; Parein, T.; Lonné, Q.; Blond, D.; Retoux, R.; Gascoin, F.; Pluart, L. L.; Lemouchi, C. 1-Dodecanthiol-Assisted Aqueous Synthesis and Characterization of Bi2Te3 Nanotubes. *Nano-Structures & Nano-Objects* **2021**, *25*, 100629. https://doi.org/10.1016/j.nanoso.2020.100629.

(142) Giri, L.; Mallick, G.; Jackson, A. C.; Griep, M. H.; Karna, S. P. Synthesis and Characterization of High-Purity, Single Phase Hexagonal Bi2Te3 Nanostructures. *RSC Adv.* **2015**, *5* (32), 24930–24935. https://doi.org/10.1039/C5RA02303C.

(143) Chen, J.; Wu, L.-M.; Chen, L. Syntheses and Characterizations of Bismuth Nanofilms and Nanorhombuses by the Structure-Controlling Solventless Method. *Inorg. Chem.* **2007**, *46* (2), 586–591. https://doi.org/10.1021/ic0615067.

(144) Du, R.; Hsu, H.-C.; Balram, A. C.; Yin, Y.; Dong, S.; Dai, W.; Zhao, W.; Kim, D.; Yu, S.-Y.; Wang, J.; Li, X.; Mohney, S. E.; Tadigadapa, S.; Samarth, N.; Chan, M. H. W.; Jain, Jainendra. K.; Liu, C.-X.; Li, Q. Robustness of Topological Surface States against Strong Disorder Observed in $\mathrm{B}{\mathrm{i}}_{2}\mathrm{T}{\mathrm{e}}_{3}$ Nanotubes. *Phys. Rev. B* **2016**, *93* (19), 195402. https://doi.org/10.1103/PhysRevB.93.195402.

(145) Wang, Z.; Wang, F.; Chen, H.; Zhu, L.; Yu, H.; Jian, X. Synthesis and Characterization of Bi2Te3 Nanotubes by a Hydrothermal Method. *Journal of Alloys and Compounds* **2010**, *492* (1), L50–L53. https://doi.org/10.1016/j.jallcom.2009.11.155.

(146) Zhao, X. B.; Ji, X. H.; Zhang, Y. H.; Zhu, T. J.; Tu, J. P.; Zhang, X. B. Bismuth Telluride Nanotubes and the Effects on the Thermoelectric Properties of Nanotube-Containing Nanocomposites. *Appl. Phys. Lett.* **2005**, *86* (6), 062111. https://doi.org/10.1063/1.1863440.

(147) Kullmann, W.; Geurts, J.; Richter, W.; Lehner, N.; Rauh, H.; Steigenberger, U.; Eichhorn, G.; Geick, R. Effect of Hydrostatic and Uniaxial Pressure on Structural Properties and Raman Active Lattice Vibrations in Bi2Te3. *physica status solidi (b)* **1984**, *125* (1), 131–138. https://doi.org/10.1002/pssb.2221250114.

(148) Glavee, G. N.; Klabunde, K. J.; Sorensen, C. M.; Hadjipanayis, G. C. Borohydride Reduction of Nickel and Copper Ions in Aqueous and Nonaqueous Media. Controllable Chemistry Leading to

Nanoscale Metal and Metal Boride Particles. *Langmuir* **1994**, *10* (12), 4726–4730. https://doi.org/10.1021/la00024a055.

(149) Glavee, G. N.; Klabunde, K. J.; Sorensen, C. M.; Hadjapanayis, G. C. Borohydride Reductions of Metal Ions. A New Understanding of the Chemistry Leading to Nanoscale Particles of Metals, Borides, and Metal Borates. *Langmuir* **1992**, *8* (3), 771–773. https://doi.org/10.1021/la00039a008.

(150) Chatenet, M.; Micoud, F.; Roche, I.; Chainet, E. Kinetics of Sodium Borohydride Direct Oxidation and Oxygen Reduction in Sodium Hydroxide Electrolyte: Part I. BH4− Electro-Oxidation on Au and Ag Catalysts. *Electrochimica Acta* **2006**, *51* (25), 5459–5467. https://doi.org/10.1016/j.electacta.2006.02.015.

(151) Chen, J.; Tan, S.; Liang, X.; Liu, W.; Ji, G. Rod-like Te as Excellent Microwave Absorber: A New Exploration. *Journal of Alloys and Compounds* **2019**, *777*, 1197–1203. https://doi.org/10.1016/j.jallcom.2018.11.113.

(152) Raj, C. R.; Samanta, A.; Noh, S. H.; Mondal, S.; Okajima, T.; Ohsaka, T. Emerging New Generation Electrocatalysts for the Oxygen Reduction Reaction. *J. Mater. Chem. A* **2016**, *4* (29), 11156–11178. https://doi.org/10.1039/C6TA03300H.

(153) Cherin, P.; Unger, P. Two-Dimensional Refinement of the Crystal Structure of Tellurium. *Acta Cryst* **1967**, *23* (4), 670–671. https://doi.org/10.1107/S0365110X6700341X.

(154) Kim, S. H.; Kim, J. J.; Suh, S. W.; Park, B. K.; Lee, J. B. The Effect of the Microstructures of Te Nanowires on the Crystal Growth of One-Dimensional Bi2Te3 Nanotubes. *Journal of Industrial and Engineering Chemistry* **2010**, *16* (5), 741–747. https://doi.org/10.1016/j.jiec.2010.07.009.

(155) Xi, G.; Peng, Y.; Yu, W.; Qian, Y. Synthesis, Characterization, and Growth Mechanism of Tellurium Nanotubes. *Crystal Growth & Design* **2005**, *5* (1), 325–328. https://doi.org/10.1021/cg049867p.

(156) Ge, Z.-H.; Nolas, G. S. Purification and Crystal Growth of Single-Crystalline Tellurium Tubes and Rods. *Materials Letters* **2017**, *194*, 20–22. https://doi.org/10.1016/j.matlet.2017.01.137.

(157) Gautam, U. K.; Rao, C. N. R. Controlled Synthesis of Crystalline Tellurium Nanorods, Nanowires, Nanobelts and Related Structures by a Self-Seeding Solution Process. *J. Mater. Chem.* **2004**, *14* (16), 2530–2535. https://doi.org/10.1039/B405006A.

(158) Liu, Z.; Hu, Z.; Liang, J.; Li, S.; Yang, Y.; Peng, S.; Qian, Y. Size-Controlled Synthesis and Growth Mechanism of Monodisperse Tellurium Nanorods by a Surfactant-Assisted Method. *Langmuir* **2004**, *20* (1), 214–218. https://doi.org/10.1021/la035160d.

(159) Sun, X.; Yang, J.; Liu, Q.; Cheng, X. Influence of Sodium Dodecyl Benzene Sulfonate (SDBS) on the Morphology and Negative Thermal Expansion Property of ZrW2O8 Powders Synthesized by Hydrothermal Method. *Journal of Alloys and Compounds* **2009**, *481* (1), 668–672. https://doi.org/10.1016/j.jallcom.2009.03.061.

(160) Wang, C.; Liao, K. Kirkendall Synthesis and Characterization of Nanotubular (Bi2)m(Bi2Te3)n Series. *Materials Research Bulletin* **2022**, *152*, 111827. https://doi.org/10.1016/j.materresbull.2022.111827.

(161) Wang, W.; Goebl, J.; He, L.; Aloni, S.; Hu, Y.; Zhen, L.; Yin, Y. Epitaxial Growth of Shape-Controlled Bi2Te3−Te Heterogeneous Nanostructures. *J. Am. Chem. Soc.* **2010**, *132* (48), 17316–17324. https://doi.org/10.1021/ja108186w.

(162) Kim, H.-Y.; Han, M.-K.; Kim, S.-J. Morphological Control of Bi2Te3 Nanotubes and Their Thermoelectric Properties. *Journal of Nanoscience and Nanotechnology* **2015**, *15* (8), 6044–6047. https://doi.org/10.1166/jnn.2015.10443.

(163) Nakajima, S. The Crystal Structure of Bi2Te3−xSex. *Journal of Physics and Chemistry of Solids* **1963**, *24* (3), 479–485. https://doi.org/10.1016/0022-3697(63)90207-5.

(164) Goldsmid, H. J. Recent Studies of Bismuth Telluride and Its Alloys. *Journal of Applied Physics* **1961**, *32* (10), 2198–2202. https://doi.org/10.1063/1.1777042.

(165) Kaibe, H.; Tanaka, Y.; Sakata, M.; Nishida, I. Anisotropic Galvanomagnetic and Thermoelectric Properties of N-Type Bi2Te3 Single Crystal with the Composition of a Useful Thermoelectric Cooling Material. *Journal of Physics and Chemistry of Solids* **1989**, *50* (9), 945–950. https://doi.org/10.1016/0022-3697(89)90045-0.

(166) Witting, I. T.; Chasapis, T. C.; Ricci, F.; Peters, M.; Heinz, N. A.; Hautier, G.; Snyder, G. J. The Thermoelectric Properties of Bismuth Telluride. *Advanced Electronic Materials* **2019**, *5* (6), 1800904. https://doi.org/10.1002/aelm.201800904.

(167) Wu, F.; Wang, W.; Hu, X.; Tang, M. Thermoelectric Properties of I-Doped n-Type Bi2Te3-Based Material Prepared by Hydrothermal and Subsequent Hot Pressing. *Progress in Natural Science: Materials International* **2017**, *27* (2), 203–207. https://doi.org/10.1016/j.pnsc.2017.02.009.

(168) Yu, F.; Zhang, J.; Yu, D.; He, J.; Liu, Z.; Xu, B.; Tian, Y. Enhanced Thermoelectric Figure of Merit in Nanocrystalline Bi2Te3 Bulk. *Journal of Applied Physics* **2009**, *105* (9), 094303. https://doi.org/10.1063/1.3120865.

(169) Plecháček, T.; Navrátil, J.; Horák, J.; Lošťák, P. Defect Structure of Pb-Doped Bi2Te3 Single Crystals. *Philosophical Magazine* **2004**, *84* (21), 2217–2228. https://doi.org/10.1080/14786430410001678226.

(170) Wu, F.; Song, H.; Gao, F.; Shi, W.; Jia, J.; Hu, X. Effects of Different Morphologies of Bi2Te3 Nanopowders on Thermoelectric Properties. *J. Electron. Mater.* **2013**, *42* (6), 1140–1145. https://doi.org/10.1007/s11664-013-2541-z.

(171) Lee, C.; Kim, J. N.; Tak, J.-Y.; Cho, H. K.; Shim, J. H.; Lim, Y. S.; Whangbo, M.-H. Comparison of the Electronic and Thermoelectric Properties of Three Layered Phases Bi2Te3, PbBi2Te4 and PbBi4Te7: LEGO Thermoelectrics. *AIP Advances* **2018**, *8* (11), 115213. https://doi.org/10.1063/1.5047823.

(172) Scanlon, D. O.; King, P. D. C.; Singh, R. P.; de la Torre, A.; Walker, S. M.; Balakrishnan, G.; Baumberger, F.; Catlow, C. R. A. Controlling Bulk Conductivity in Topological Insulators: Key Role of Anti-Site Defects. *Advanced Materials* **2012**, *24* (16), 2154–2158. https://doi.org/10.1002/adma.201200187.

(173) Zhao, C.; Li, Z.; Fan, T.; Xiao, C.; Xie, Y. Defects Engineering with Multiple Dimensions in Thermoelectric Materials. *Research* **2020**, *2020*. https://doi.org/10.34133/2020/9652749.

(174) Li, F.; Zhai, R.; Wu, Y.; Xu, Z.; Zhao, X.; Zhu, T. Enhanced Thermoelectric Performance of N-Type Bismuth-Telluride-Based Alloys via In Alloying and Hot Deformation for Mid-Temperature Power Generation. *Journal of Materiomics* **2018**, *4* (3), 208–214. https://doi.org/10.1016/j.jmat.2018.05.008.

(175) Wang, S.; Xie, W.; Li, H.; Tang, X. Enhanced Performances of Melt Spun Bi2(Te,Se)3 for n-Type Thermoelectric Legs. *Intermetallics* **2011**, *19* (7), 1024–1031. https://doi.org/10.1016/j.intermet.2011.03.006.

(176) Zhu, B.; Liu, X.; Wang, Q.; Qiu, Y.; Shu, Z.; Guo, Z.; Tong, Y.; Cui, J.; Gu, M.; He, J. Realizing Record High Performance in N-Type Bi2Te3-Based Thermoelectric Materials. *Energy Environ. Sci.* **2020**, *13* (7), 2106–2114. https://doi.org/10.1039/D0EE01349H.

(177) Nozariasbmarz, A.; Krasinski, J. S.; Vashaee, D. N-Type Bismuth Telluride Nanocomposite Materials Optimization for Thermoelectric Generators in Wearable Applications. *Materials (Basel)* **2019**, *12* (9), 1529. https://doi.org/10.3390/ma12091529.

(178) Pascal, J.-P.; Saurereau, H.; Verdu, J.; Williams, R. *Thermosetting Polymers*; Markel Deccer Inc.

(179) Naresh, K.; Adrian, S. Standardisation of Mixing Method for Experimental Resin-Based Composite | Journal of the Pakistan Dental Association.

(180) Kröning, K.; Krause, B.; Pötschke, P.; Fiedler, B. Nanocomposites with P- and n-Type Conductivity Controlled by Type and Content of Nanotubes in Thermosets for Thermoelectric Applications. *Nanomaterials (Basel)* **2020**, *10* (6), 1144. https://doi.org/10.3390/nano10061144.

(181) Tam, D. K. Y.; Ruan, S.; Gao, P.; Yu, T. 10 - High-Performance Ballistic Protection Using Polymer Nanocomposites. In *Advances in Military Textiles and Personal Equipment*; Sparks, E., Ed.; Woodhead Publishing Series in Textiles; Woodhead Publishing, 2012; pp 213–237. https://doi.org/10.1533/9780857095572.2.213.

Reference list

Appendixes

Appendix-1. Analysis by Electron Microscopy

1.1 Scanning electron microscopy

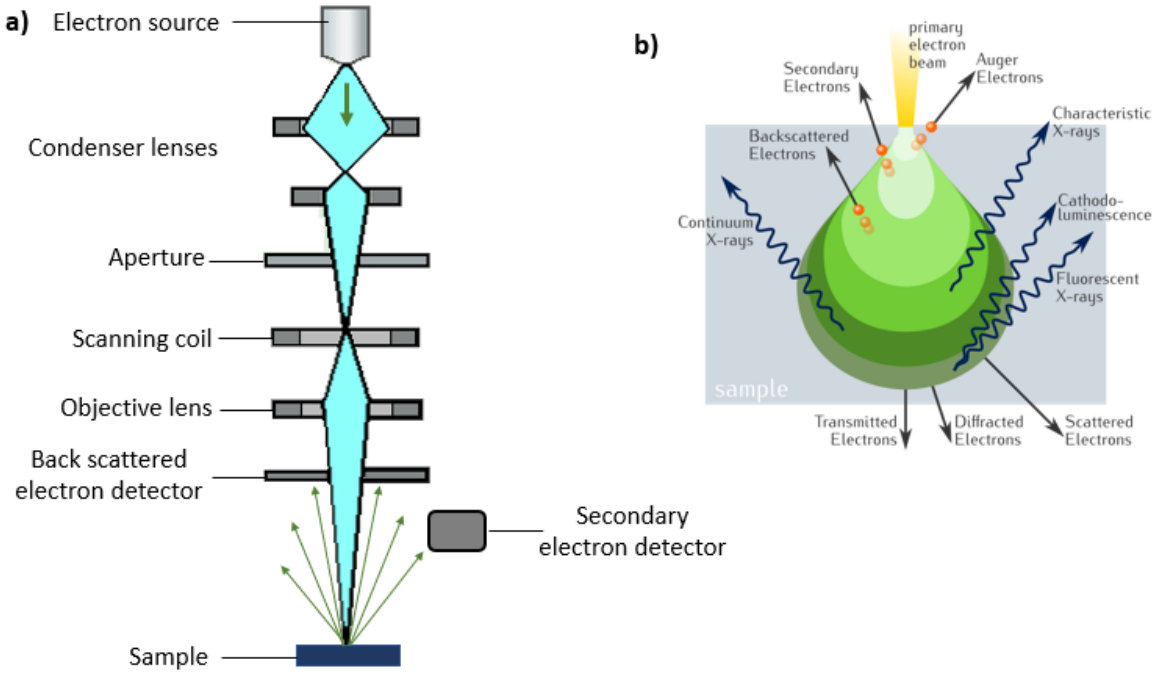

Figure – A.1.1: a – Scheme of SEM; b – types of signals generated by focused electron beam in the sample

Scanning electron microscopy (SEM) is a type of microscope where the surface image of the sample is produced by scanning it with focused electron beams. The electron beam excites the sample atoms and prompts it to emit various electrons which pocess information about the composition and surface topology of the sample. Emitted electrons are detected and, in combination with the applied electron beam intensity and position, used to produce the surface image of the sample. General scheme of SEM is depicted on Figure-A.1.1a. When the sample is targeted by electron beam it produces electrons with various energy, thus different detectors are used to detects them. In the basic SEM, secondary electrons are detected to produce the surface topology images. They have lowest energy of 50eV and as a result their main free path is limited to few nanometres. Thus, they carry information only about few nanometre depths of the sample. All the electrons with various energy and their relative depth in the sample is depicted on Figure-A.1.1b. Other commonly detected electrons in SEMs are back-scattered electron and characteristic X-ray. Back-scattered electrons are produced as a result of elastic scattering and because they have higher energy, can originate from deeper

locations in the sample than secondary electron. Back-scattered electrons mainly used to analyse the distribution of the constituents of the sample as their signal intensity correlates with the atomic number of the elements, therefore different species have distinctive contrast on the images. Characteristic X-ray electrons are used to do elemental analysis of the sample surface known as electron dispersive X-ray spectroscopy (EDS).

In the course of the current thesis research, to characterise the powder samples, ZEISS Supra 55 microscopy with secondary electron and characteristic X-ray electron detectors was used, without specific sample preparation. The bulk samples, as composites and sintered samples was characterized by JOEL microscope, with prior ion beam polishing of the sample surface by JOEL SM-09010 cross-section polisher.

1.2 Transmission electron microscopy

Transmission electron microscopy is a type of microscopy where the images are acquired by detecting the electrons passed through the sample. Therefore, high-energy electron beams are used in contrast with other electron microscopy and the sample is required to have small thickness. The electrons, passed through the sample contains specific information as a result of their interaction with specimen atoms and detected to produce images. Owing to the low wavelength of the electrons, TEM images have high resolution and can be used to images very small samples. In the current thesis JOEL 2010 FEG TEM equipped with double tilt sample holder for High resolution analysis, was used to characterize Bi_2Te_3 samples.

Appendix-2. X-ray diffraction

X-ray diffraction is material analysis technique to determine its crystallographic structure. To analyse the material the sample is irradiated by incident X-rays and angles and intensities of the scattered X-rays are measured and used to calculate crystal structure of the material using Braggs law:

$$n\lambda = 2dsin\theta$$

where, d – is a distance between diffraction planes; λ – beam wavelength; θ – incident angle; n – integer number.

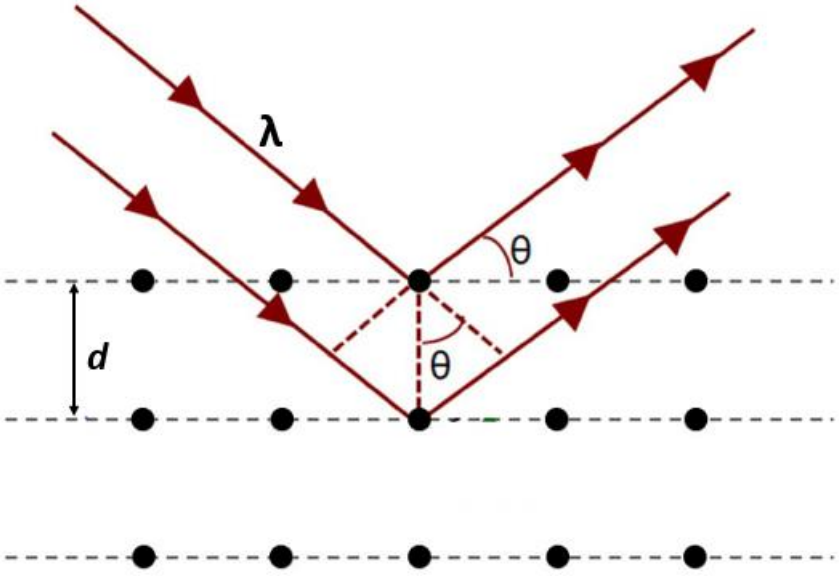

Figure – A.2. X-ray diffraction scheme in a crystal structure

To analyse the samples in the current research X'Pert Pro diffractometer of Panalytical with Pixel detector is used by Cu Kα radiation (λKα1 = 1.5406 Å/λKα2 = 1.544 Å). Data was collected a step size 0,0131°. The diffractograms were refined using a Maud software.

Appendix-3. Sintering

Sintering of the samples by Spark Plasma Sintering

Bi_2Te_3 nanoparticles were sintered by Spark Plasma Sintering (SPS) technique for further thermoelectrical characterizations. SPS is a sintering technique applied for densification of powders and synthesis. Schematics of the sample loading part of the conventional SPS is depicted on Figure-A.3a.[1] In a general procedure the sample powder is placed in the graphite die and between two punches. Then, this sample loading part is placed in the mechanical loading part of the machine, which acts as both, to apply a mechanical pressure and as an electrical circuit. Sintering is activated by pulsed direct current passing from machine to punches, die and through the sample (in the case of conductive samples). Current creates Joule heating; therefore, no external heat is applied. Materials in the electrical circuit (die, punches and other parts of the machine in the circuit) have good electrical conductivity, therefore upon applying low voltages high current and efficient Joule heating is produced. Joule heating allows efficiently heat the sample, thus permits fast sintering. Heating rate as 1000°C/min and cooling rate as 150°C/min is possible to achieve with SPS. Mechanical pressure is applied while the sample is being heated. The process is regulated by temperature control via pyrometer and thermocouple or by displacement of the punches. Pulsed current passing through the sample does not only heat it, but also activates the particles surface, thus increases the diffusion rate.[2] It leads to efficient sintering and densification as high as 95% of the theoretical values.

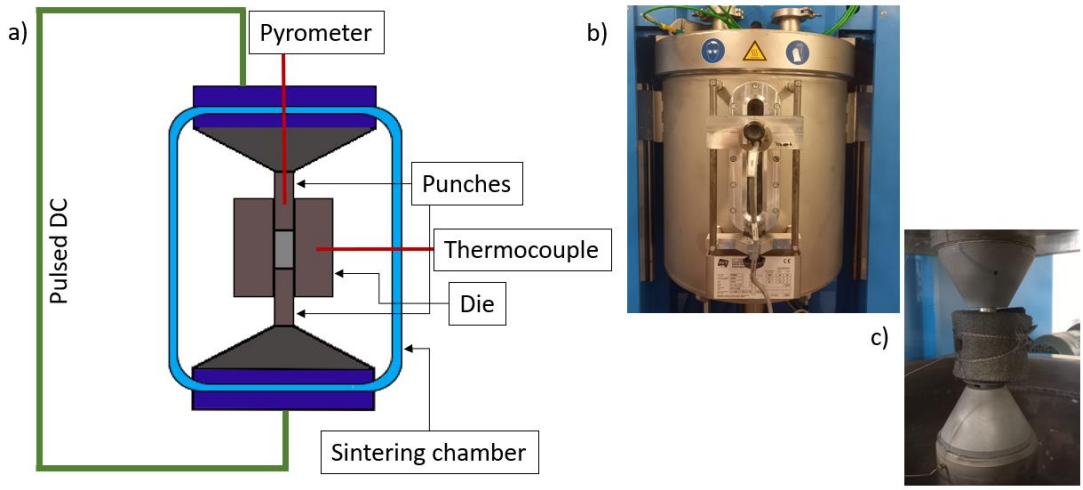

Figure – A.3: a – general schematics of sintering chamber of SPS machine; b – sintering chamber of SPS HP D25 FCT used for experiments; c – sample loading unit of the used SPS machine

Appendixes

Bi_2Te_3 samples were sintered by SPS HP D25 FCT. Powder were densified in a graphene die with an inner d = 10 mm. Sintering procedure was set up as following: heating to 450°C in 30 min, constant temperature of 450°C for 30 min, then cooling to room temperature in 30 min. Applied pressure was 5kN during the whole cycle. Sintering carried out under Ar atmosphere. Densities of obtained powder were measured by Archimedes method and varied between 94% and 96% of theoretical value of bulk the Bi_2Te_3 (7700 kg/m^3).

(1) Guillon, O.; Gonzalez-Julian, J.; Dargatz, B.; Kessel, T.; Schierning, G.; Räthel, J.; Herrmann, M. Field-Assisted Sintering Technology/Spark Plasma Sintering: Mechanisms, Materials, and Technology Developments. *Adv. Eng. Mater.* **2014**, *16* (7), 830–849. https://doi.org/10.1002/adem.201300409.

(2) Mamedov, V. Spark Plasma Sintering as Advanced PM Sintering Method. *Powder Metall.* **2002**, *45* (4), 322–328. https://doi.org/10.1179/003258902225007041.

Appendix-4. Measurement of transport properties

Measurement of electrical resistivity and Seebeck coefficient

Measurement of Seebeck coefficient and electrical resistivity were carried out on ZEM 3 of Advance Riko, Japan – a system which measures two values simultaneously. The measurements are carried out as following. Sample is placed between the upper and lower heating furnaces in a close contact as shown in the general scheme of the ZEM3 sample holder chamber on Figure-A.4a. The upper furnace heats the sample to the required temperature, while lower furnace provides temperature gradient. To measure the Seebeck coefficient, temperature difference between T1 and T2 is measured via thermocouple attached to the side wall of the sample. Simultaneously, electromotive force dE between the wires of the thermocouple is measured and Seebeck coefficient is calculated, considering the dimensions of the sample and distance between the two thermocouple wires. Electrical resistance is measured by four-probe method. Electrical current is applied to the sample through its ends and voltage drop dV is recorded between wires of the thermocouple. The resistivity values are calculated considering the thermoelectromotive force. Measurements are carried out under He. During the measurements in this thesis, ΔT was set to 10, 20 and 30, and final values are obtained by the mean value of the measurements under different ΔT.

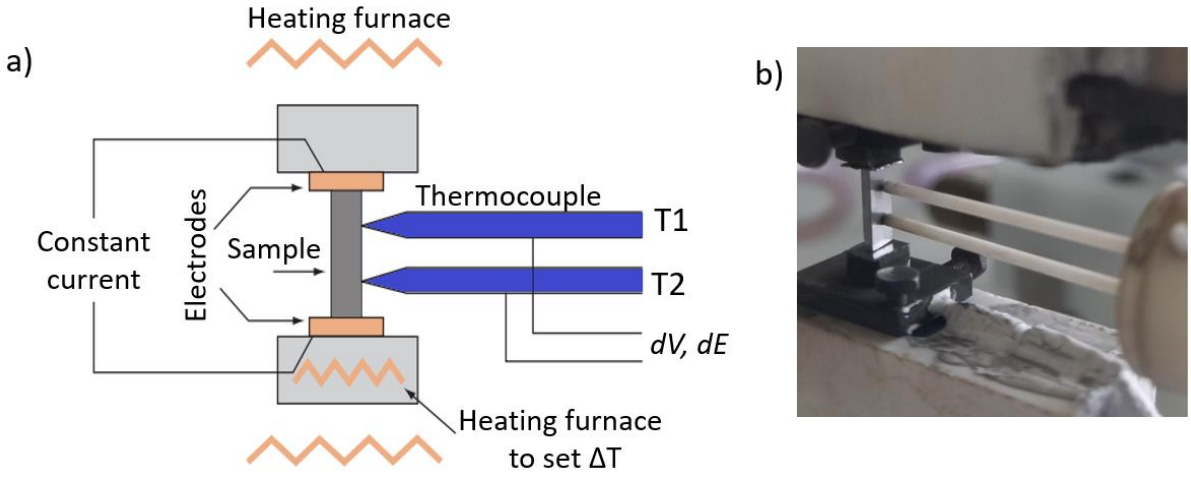

Figure – A.4: a - Schematics of the sample chamber of ZEM3; b – photo of the used ZEM3 sample chamber

Appendix-5. Thermal analysis

Thermal conductivity of the samples was calculated using the following formula:

$$\kappa(T) = D(T) \cdot C_\rho(T) \cdot \rho(T)$$

where, D – thermal diffusivity, Cp – specific heat capacity, ρ – density.

5.1 Laser Flash analysis (LFA)

Thermal diffusivity of the samples was measured by light flash method on equipment LFA-457 MicroFlash of Netzsch. In a general procedure of measurement, thin flat sample is placed in the sample holder and lower surface of the sample is heated by pulsed short energy (laser). Meanwhile, the temperature of the upper surface of the sample is detected by infrared detector. Thermal diffusivity is then calculated using the ΔT between upper lower surfaces of sample, half time of the signal and considering the sample thickness, as shown in Figure-A.5.1. In the measurements for the samples in this thesis samples with dimension 6 x 6 x 1 was used and analyses were carried out under Ar. To avoid the loose of heat by reflection, samples were first covered by thin carbon layer.

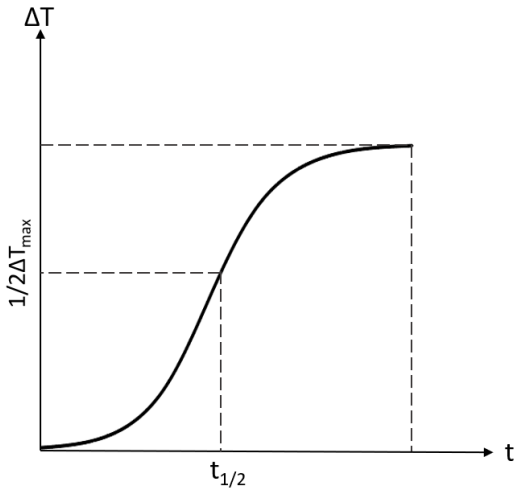

Figure – A.5.1. Generic curve to calculate the diffusivity of the sample

5.2 Differential scanning calorimetry (DSC)

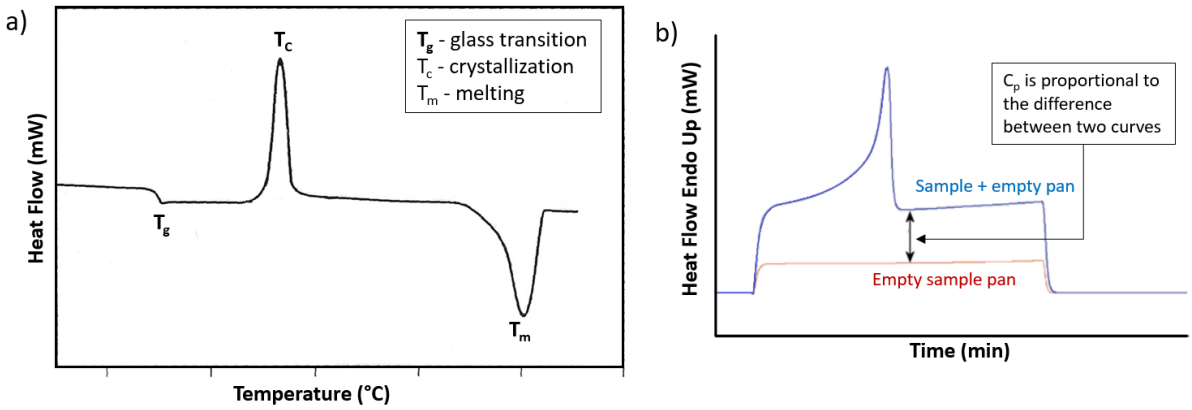

Figure – A.5.2: a – DSC curve of semi-crystalline polymer; b – Generic DSC curves of a sample and an empty pan to calculate the C_p

DSC is a thermal analysis technique where the difference between amounts of heat fluxes to increase the temperature of the sample and the reference materials is a measured. DSC can be used to determine the temperature of the phase transition, enthalpy of the reaction, C_p and other temperature related feature of the material or reaction. In the course of this thesis research, Dimond DSC and DSC-7 of Perkin Elmer were used. Dimond DSC is heat-flux type where heat-flux difference between the analysing sample and the reference is measured with integrated temperature sensors. While DSC-7 is a power compensating type where the electrical power difference to maintain the sample and the reference at the same temperature is measured. All the analyses were carried out in an aluminium pans and empty pan is used as a reference under nitrogen.

C_p of Bi_2Te_3 samples were calculated according to the Dulong-Petit law and assumed that it does not vary by temperature. C_p of the composites were measured by DSC-7 applying two curve method – the sample and background (empty pan). The difference on the DSC curves of the sample and empty pan is proportional to the C_p of the sample (Figure-A.5.2.b). Then the precision of the equipment was confirmed by measuring the Cp of a known material – sapphire. The calculations were carried out on the Pyris software for Dimond DSC.

5.3 Thermogravimetric analysis

Thermogravimetric analysis (TGA) is a thermal analysis method where the weight of the sample is evaluated as a function of temperature under controlled atmosphere. TGA allows to detects temperatures at which changes as phase transition, sorption and thermal decomposition takes place. A general equipment for TGA consists of high precision balance, furnace, chamber to control the atmosphere (within the furnace) and crucible. Sample is placed in the crucible, which is then placed on the balance. Depending on the type of machine, the furnace is closed and after application of the selected atmosphere (gas), the furnace is heated at selected rate. The weight of the sample is then recorded as a function of temperature, then the change of the weight is calculated as a function of temperature or time. In the experiments for the current thesis research, TGA were carried out on Pyris 1 analyser of Perkin Elmer. Analyses were carried out in Al_2O_3 crucible, under nitrogen atmosphere and heating rate of 20°C/min.

Appendix-6. Rheology

The rheology of the epoxy resin mixture was investigated by rheometer AR 1000 of TA Instrument. Rheometer is a device to measure the flow behaviour and deformation of a viscous liquid as a response to an applied force. They can measure Dynamic, storage and loss modulus, along with viscosity of the liquid and other properties. Used rheometer is a shear stress type, meaning that rotational shear stress is applied to the liquid and resulting strain rate is measured. In the current research all rheological measurements were carried out on plate-plate type holder as shown on Figure-A.6. Plate diameters are 25 mm. In a general procedure, the liquid is placed between lower fixed plate and upper rotating plate, then shear stress is applied by torque.

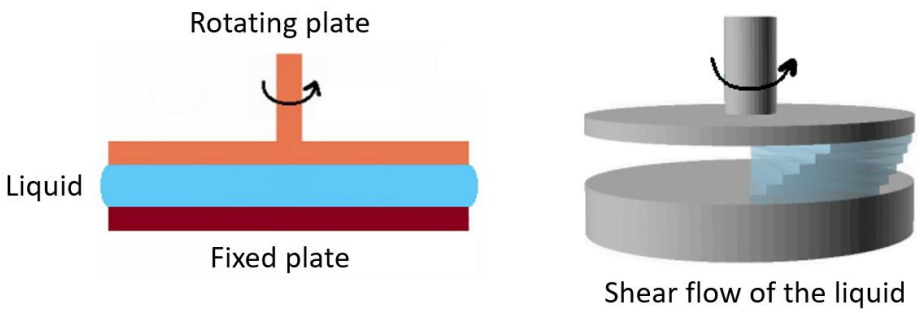

Figure – A.6: Plates for sample analysis of rheometer

Appendix-7. Chemical formulas and reactions

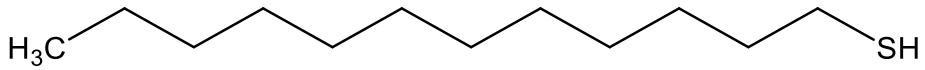

1-dodecanthiol

Used resin and hardeners:

Araldite GY 260 – is an epoxy resin made of Bisphenol A diglycidyl ether (DGEBA), with epoxy equivalent weight – 182-192 g/eq and epoxy functionality of 2 (Huntsman Advanced Materials).

Jeffamine-D230 – is a resin hardener made of polyether diamine with molecular weight of 230 mol/g and amine functionality of 4 (Huntsman Advanced Materials).

Curing of DGEBA by polyether diamine

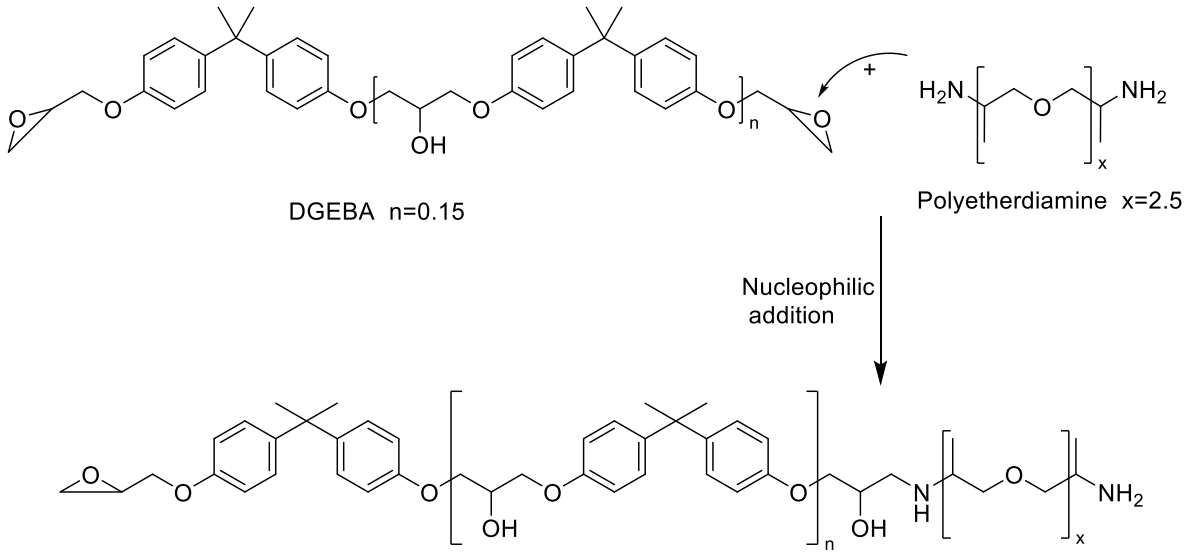

RIMR 135 – is an epoxy resin produced by Hexion. It is a mixture of resins DGEBA 570-90%) and 1,6-bis-(2, 3 -epoxypropoxy) hexane (15-20%).

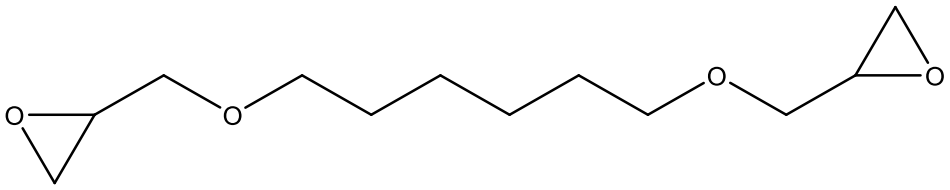

1,6-bis-(2, 3 -epoxypropoxy) hexane

RIMH 137 – is a resin hardener produced by Hexion. It is mixture of polyether diamine (50-75%) and isophorone diamine (35-50%).

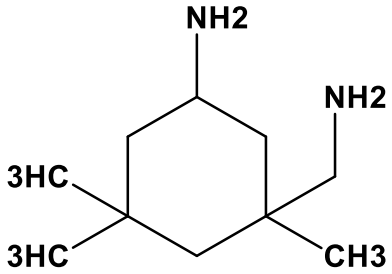

Isophorone diamine (IPDA)

Appendix-8. Miscellaneous

8.1 Thermograms

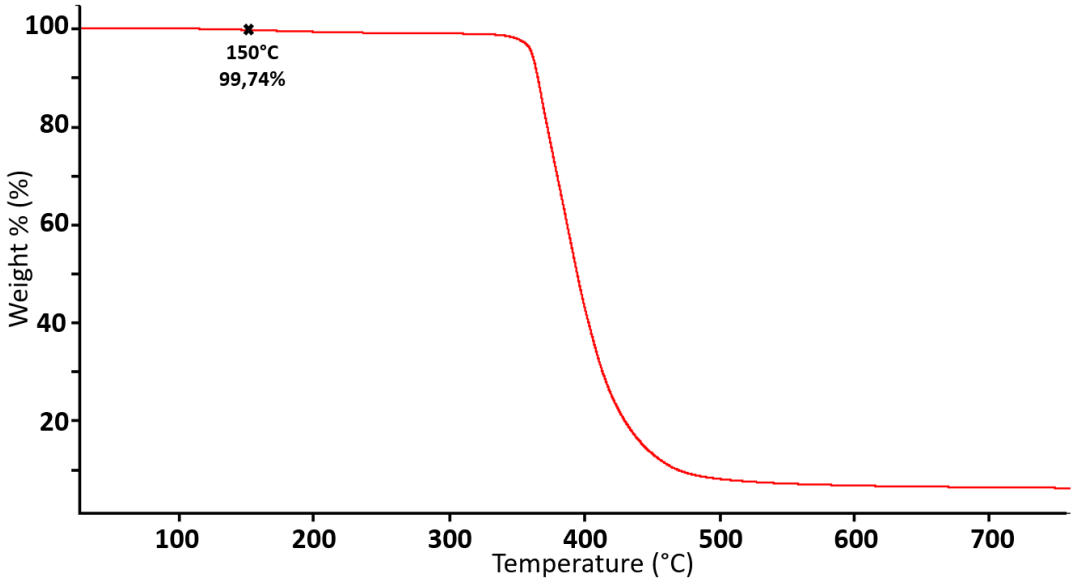

Figure – A.8.2: Thermogram of epoxy resin RIMR-135/RIMH-137

8.2 DSC traces

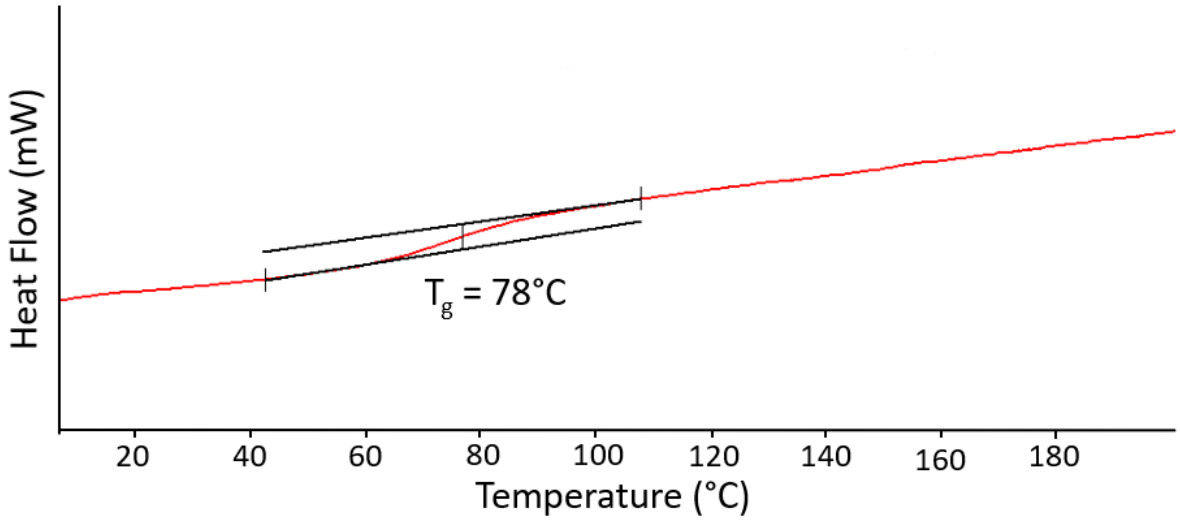

Figure – A.8.3: DSC trace of Bi_2Te_3/epoxy resin composite (RIMR-135/RIMH-137) (with indication of the Tg of the epoxy resin)

Abstract

Current thesis aims at developing methods to synthesise Bi_2Te_3 nanoparticles with nanotubular morphology in order to process composite materials. In the course of the thesis research 1-dodecanthiol assisted aqueous reflux synthesis methods of Bi_2Te_3 nanoparticles were developed. We evidenced that nanotubes formation can follow two mechanisms, rolling-up or nanoscale Kirkendall diffusion, which resulted in variation of nanotubes content from 30% up to 100% depending on the experimental parameters. Optimizing the synthesis protocols also leads to improvements of the thermoelectrical properties of the samples processed by spark plasma sintering. The developed methods are easily scalable and proceed under mild reaction conditions. Subsequently, methods to prepare polymer hybrid composites with percolating Bi_2Te_3 nanoparticles network, were explored as an alternative to energy consuming sintering process. Infusing a thermoset resin in a preformed Bi_2Te_3 buckypaper was demonstrated to be the more efficient way to obtain a non-porous conductive polymer composite with specific orientation of the filler.

Keywords: Bismuth telluride, bismuth telluride nanotubes, thermoelectric material, Bismuth telluride/epoxy resin hybrid composite

Résumé

Ce travail de thèse est consacré au développement de méthodes de synthèse de nanoparticules de Bi_2Te_3 à facteur de forme élevé afin de concevoir des matériaux composites thermoélectriques à matrice polymère. A cet effet, des protocoles de synthèse à reflux en milieu aqueux faisant intervenir le 1-dodecanethiol ont été mis au point. Il a été mis en évidence que la formation de nanotubes peut survenir par enroulement de structures bidimensionnelles ou par un effet d'interdiffusion à partir de nanotubes de tellure préformés selon le mécanisme de Kirkendall à l'échelle nanométrique. En fonction des conditions de synthèse la proportion de nanotubes au sein des nanoparticules obtenues a varié de 30 à 100%. Cette augmentation de la proportion de nanotubes s'est accompagnée d'une amélioration des propriétés thermoélectriques d'échantillons élaborés par frittage flash à partir de ces particules. Ces protocoles de synthèse en conditions douces sont facilement utilisables à plus grande échelle. Dans un second temps, des méthodes de mise en œuvre de matériaux composites thermoélectriques basés sur la formation d'un réseau de nanoparticules ont été explorées en tant qu'alternatives aux procédés énergivores de frittage. Une méthode originale, basée sur l'infusion de résine dans un réseau préformé sous forme de mat de nanoparticules, a permis d'obtenir des composites polymères conducteurs massifs dotés de propriétés thermoélectriques satisfaisantes.

Mots clés: Tellurure de bismuth, nanotubes de tellurure de bismuth, matériau thermoélectrique, composite hybride tellurure de bismuth/résine époxy